

Autonomous Science Target Detection and Touchability Assessment for Planetary Exploration

Chen Gui

Department of Computer Science
Aberystwyth University

August
2015

This thesis is submitted in partial fulfilment of the
requirements for the degree of
Doctor of Philosophy of Aberystwyth University.

Declaration

This thesis has not previously been accepted in substance for any degree and is not being concurrently submitted in candidature for any degree.

Signed (candidate)

Date

Statement 1

This thesis is the result of my own investigations, except where otherwise stated.

Other sources are acknowledged by footnotes giving explicit references. A bibliography is appended.

Signed (candidate)

Date

Statement 2

I hereby give consent for my thesis, if accepted, to be made available for photocopying and for inter-library loan, and for the title and summary to be made available to outside organisations.

Signed (candidate)

Date

ABSTRACT

One of the goals of planetary exploration is to cache rock samples for subsequent return to the Earth in future Mars Sample Return missions. Rocks on the Martian surface are one of the most interesting science targets for geologists and planetary scientists. Hence, it is essential to develop a method for the accurate segmentation of Martian rocks in Mars images. This thesis introduces a new approach to segmenting Mars images captured by the NASA Mars Exploration Rover (MER). An improved OTSU and Canny operator are utilized for detecting rock regions and their space relations, respectively. The closed contours of detected rocks are gained by the use of template dilatation edge linking for a given set of images. These images have been obtained from MER Navcam and Pancam.

Experimental results of six representative images (with different illumination levels, spectral bands and scenes) including a total of 128 rocks are shown. In these experiments qualitative and quantitative comparisons are accomplished. The results demonstrate that the proposed approach is consistent with human perception and is the best in terms of the average values over the performance indices such as Precision, Recall and misclassification error in comparison to the existing approaches. Additionally, a method is proposed for computing the size of a detected rock through the stereo triangulation technique. Experimental results also show that this proposed method offers better accuracy than the standard disparity algorithm.

Currently, science target selection, and whether or not it is possible for a robot arm to touch the target, is accomplished by human operators and scientists on the Earth. The use of onboard autonomy would greatly reduce the human intervention, and it would be advantageous if the rover could evaluate autonomously whether the robot arm could place an instrument against an identified science target. In this thesis a fuzzy logic-based system is presented to address the problem of autonomous science target touchability evaluation. The touchability of a potential science target is assessed in terms of its size (the bounding area of the rock), SV (the science value of the target), distance (the reachable distance of the arm between its base and the science target), and orientation (the angular regions of the arm's shoulder azimuth). In particular, the plane in front of the arm is divided into a number of partitions, which are ranked with the different touchability levels by the use of a fuzzy rule-based system. Simulations on the rank of science object touchability are carried out, via hardware implementation. Based on the real data gathered from the cameras and the Schunk arm experimental results successfully verify the validity of the proposed touchability approach and associated software and hardware implementations.

ACKNOWLEDGEMENTS

Particularly, I would like to thank my previous supervisor Professor Dave Barnes for his guidance and support throughout my research. I would like to thank him for the things he taught me and the hours he devoted to helping me overcome obstacles in my research. Without his help and insight this research would not have been possible. I am extremely grieved as he passed away. He will live in my heart for ever.

I would also like to thank my supervisor, Dr Changjing Shang, who is kind, generous, supportive and understanding, giving me enormous scientific guidance on my research and writing. She is a great mentor and her enthusiasm has always been one of my greatest encouragements. Without her guidance and support this thesis would not exist - thank you very much!

I would also like to acknowledge my second supervisor Dr Frederic Labrosse for his efforts in discussing my work. My special thanks also go to Professor Qiang Shen, without him it is impossible to start my PhD study in Aberystwyth University. I am very grateful to my home university, ChongQing University of Science and Technology that provide me with the support of funding. I am glad to work and discuss my research with Dr Laurence Tyler and Lilan Pan for their help to my research.

Finally, I would like to thank my family for their patience, understanding and support during my studies.

Contents

1	Introduction	12
1.1	Background of the Research	12
1.1.1	ExoMars Programme	13
1.1.1.1	ExoMars Rover	15
1.1.1.2	ExoMars Instruments	16
1.2	Need for Autonomous Systems	18
1.2.1	Benefits of Full Autonomy	19
1.2.2	Benefits of Limited Autonomy	21
1.3	Research Aim and Objectives	22
1.4	Thesis Outline	23
2	Autonomous Science Systems	28
2.1	Robotic Antarctic Meteorite Search (RAMS)	28
2.1.1	Image Segmentation	29
2.1.2	Rock Classification	30
2.1.3	Bayes Network	31
2.1.4	Final Notes on RAMS	31
2.2	CREST Autonomous Robotic Scientist (ARS)	32
2.2.1	Science Assessment and Response Agent (SARA)	33
2.2.1.1	Science Assessment Framework (SAF)	35
2.2.1.2	Science Agent	36
2.2.2	Final Notes on CREST	36
2.3	Single Command Approach and Instrument Placement (SCAIP)	38
2.3.1	Final Notes on SCAIP	42
2.4	On-board Autonomous Rover Science Investigation System (OASIS)	43
2.4.1	Feature Detection	43
2.4.2	Image Segmentation	45
2.4.2.1	Feature Extracion	46
2.4.2.2	Planning and execution	48
2.4.3	Final Notes on OASIS	49
2.5	Summary	49

3	Target Detection and SIFT-Based Matching Desired Keypoints	51
3.1	Background	51
3.2	Target Identification	53
3.2.1	Overview of the Proposed System	53
3.2.2	Rock Detection	53
3.2.2.1	Tri-level Thresholding OTSU	54
3.2.2.2	Merge of Regions	57
3.2.2.3	Template Dilatation Edge Linking (TDEL)	60
3.3	Matching Keypoints	62
3.3.1	SIFT-RANSAC Algorithm	62
3.3.2	Fundamental Matrix	67
3.3.3	Epipolar Geometry	68
3.3.4	Rough Matching Points	68
3.3.5	Matching through Correlation	70
3.3.6	Triangulation	71
3.4	Experimental Study	74
3.4.1	Segmentation Based Upon Mars Images	74
3.4.1.1	Qualitative Comparison	74
3.4.1.2	Quantitative Comparison	75
3.4.2	Rocks Size Measurement and Results	80
3.4.2.1	PATLab	80
3.4.2.2	Experimental Results	80
3.5	Summary	82
4	Designing Algorithms for Touchability Index Evaluation	89
4.1	Background	89
4.2	Fuzzy Control System	90
4.2.1	Fuzzy Sets	91
4.2.2	Linguistic Variables	94
4.2.3	Fuzzy Rules	96
4.2.4	Defuzzification	97
4.2.5	Structure of Fuzzy Controllers	98
4.3	Fuzzy Logic Control of Touchability System	99
4.3.1	Overview of the Touchability System	99
4.3.2	Proposed Approach	100
4.3.2.1	Fuzzification	100
4.3.2.1.1	Size (i_s)	100
4.3.2.1.2	Distance (i_d)	102
4.3.2.1.3	Orientation (i_o)	104
4.3.2.1.4	Science Value (SV) (i_{SV})	104
4.3.2.2	Inference Mechanism	106
4.3.2.3	Defuzzification	110
4.4	Simulation Results and Analysis	110
4.5	Summary	112

5	Experimentation of the Touchability System	114
5.1	Experimental Platform	114
5.1.1	Cameras	115
5.1.1.1	Camera Calibration	116
5.1.2	Optical Bench	118
5.1.3	Schunk Arm	118
5.1.3.1	Object Location	121
5.1.3.2	Translations	122
5.1.3.3	Rotations	123
5.1.3.4	Forward Kinematics	123
5.1.3.5	Inverse Kinematics	125
5.2	Experimental Results	130
5.2.1	Experiment 1	130
5.2.2	Experiment 2	131
5.2.3	Experiment 3	134
5.2.4	Experiment 4	134
5.2.5	Experiment 5	136
5.2.6	Experiment 6	136
5.2.7	Experiment 7	138
5.3	Discussion of Results	138
5.4	Summary	139
6	Conclusions	140
6.1	Summary of the Work	140
6.2	Original Contribution	142
6.3	Future Research	144
	Appendix A List of Acronyms	146
	References	148

List of Figures

1.1	The Beagle 2 lander. The ARM would position the PAW whose calibration undertaken by Aberystwyth University to conduct panoramic, macroscopic and microscopic imaging, in-situ compositional analysis, and sample acquisition for the Gas Analysis Package (GAP) experiment (Barnes <i>et al.</i> , 2003; Barnes <i>et al.</i> , 2006). Image courtesy of ESA	14
1.2	Artist's impression of the ExoMars rover. Image courtesy of ESA	16
1.3	Artists rendition: A. Viking Lander, B. Mars Pathfinder and Sojourner Rover, C. MER Rover, D. Curiosity Rover. Composite images courtesy of NASA/JPL	20
1.4	Rover to Earth communication during the representative instrument placement. Composite images courtesy of NASA/JPL	25
1.5	Rover to Earth communication during instrument placement, a fully autonomous system E4. Composite images courtesy of NASA/JPL	26
1.6	Rover to Earth communication during instrument placement, a semi-autonomous system with ground based target decisions E3. Composite images courtesy of NASA/JPL	27
2.1	Image of Carnegie Mellons Nomad Rover (Image courtesy of Carnegie Mellon). Nomad is a 4 wheel drive rover measuring 2.4 m × 2.4 m × 2.4 m, and has a total mass of just over 700 kg	29
2.2	Opportunistic science aims of CREST (Image courtesy of SciSys, (Woods <i>et al.</i> , 2009). This image outlines a basic ExoMars exploration cycle, showing the potential for opportunistic science activities. The main objective is to traverse from a previously explored site (A) and progress toward the next site at B, where detailed sample assessment will be carried out. The intention is to visit seven sites over the nominal 180-sol period. Opportunistic science is clearly possible during the traverse phase and could be used to improve the robustness of data acquisition and prioritisation during the measurement cycle.	34
2.3	CREST Project Architecture (Image courtesy of SciSys (Woods <i>et al.</i> , 2009))	35
2.4	SARA architecture (Image courtesy of SciSys (Woods <i>et al.</i> , 2009))	40

2.5	Instrument placement results from 11 trial runs of the prior algorithm with the distance being 32.5cm between the most-left yellow cross and the most-right yellow cross, with crosses at the positions where the instrument arm made contact overlaid on the short range image used for arm trajectory planning. Instrument arm contact positions for the SCAIP effort all lie within the 1cm radius red circle centred on the designated target. Image courtesy of NASA/JPL . . .	41
2.6	Example rock target demonstrating lamination features.	42
2.7	Full architecture of the OASIS system. Image courtesy of NASA/JPL	44
2.8	Dust Devil as observed by MER Spirit rover (Image courtesy of NASA/JPL)	47
3.1	An overview of the proposed system.	54
3.2	An image example and histogram from MER Navcam data showing the optimal thresholds g_1^* and g_2^* ($[0, g_1^*]:\text{shadow}$; $[g_1^*, g_2^*]:\text{rock}$; $[g_2^*, 255]:\text{ground}$)	55
3.3	(a) Resultant image of proposed method from Tri-level Thresholding OTSU. (b) Resultant image from connecting endpoints.	58
3.4	Four types of Y-junction.	59
3.5	Intersection (a) and merging (b) of Regions and Edges.	61
3.6	Top: The rocks included in the irregular bounding box. [Red line denotes the irregular bounding box]. Bottom: Patch of the image for subsequently explaining the TDEL algorithm. In the patch red pixels form a rough rock boundary, the other colour pixels from the real rock boundary that can be connected.	63
3.7	(a) 3×3 template. ‘C’ pixel is the center of the template on an irregular bounding box. Here no pixel has a different colour except for the red and black, so there is no connection performed. (b) 5×5 template. The template is a dilatation of the above 3×3 template. Here ‘18’, ‘19’ and ‘24’ pixels are in different colours in addition to red and black, and the colour of ‘18’ and ‘19’ is different from the colour of ‘24’. Therefore, the distances between ‘18’ and ‘24’, ‘19’ and ‘24’ are calculated separately. The nearest distance is from ‘19’ to ‘24’ in the two results, so these two pixels are connected using a straight line.	64
3.8	SIFT based matching result.	66
3.9	RANSAC result relative to Figure 3.8.	67
3.10	Epipolar geometry. Two cameras are used to observe a point X, with their respective centers of projection being O_L and O_R . The projection of X onto each of the image planes is denoted X_L and X_R . Points e_L and e_R are the epipoles.	69
3.11	Angle of rotation determination.	70
3.12	Correlation.	72
3.13	Qualitative comparison among the results using different methods.	83

3.14	Matching algorithm results for rock 1 ((a): left image results. (b): right image results).	84
3.15	Matching algorithm results for rock 2 ((a): left image results. (b): right image results).	84
3.16	Matching algorithm results for rock 3 ((a): left image results. (b): right image results).	85
3.17	Matching algorithm results for rock CONGLOMERATE ((a): left image results. (b): right image results).	85
3.18	Matching algorithm results for rock BRECCIA ((a): left image results. (b): right image results).	86
3.19	Matching algorithm results for rock SANDSTONE aolian ((a): left image results. (b): right image results).	86
3.20	Matching algorithm results for rock SANDSTONE torridonian ((a): left image results. (b): right image results).	87
3.21	Matching algorithm results for rock MUDSTONE ((a): left image results. (b): right image results).	87
3.22	Matching algorithm results for rock OXFORD CLAY ((a): left image results. (b): right image results).	88
3.23	Matching algorithm results for rock CRINOIDAL LIMESTONE ((a): left image results. (b): right image results).	88
4.1	A graphical representation of a fuzzy set.	92
4.2	Typical shapes of membership functions: 1: triangular, 2: trapezoidal, 3: Gaussian, 4: bell-shaped, 5: singleton.	93
4.3	Basic structure of a fuzzy logic controller.	99
4.4	Fuzzy Logic Touchability Controller.	101
4.5	Stereo matching points selection.	102
4.6	Membership functions for the Size (i_s).	103
4.7	Distance between arm and object.	103
4.8	Membership functions for the Distance (i_d).	104
4.9	Orientation between arm and object.	105
4.10	Decomposition of orientation regions.	105
4.11	Membership functions for the Orientation (i_o).	106
4.12	Membership functions for SV (i_{SV}).	106
4.13	Rule base for touchability (VL-VeryLow, L-Low, ML-MediumLow, M-Medium, MH-MediumHigh, H-High, VH-VeryHigh).	109
4.14	Membership functions for Touchability Index (o_t).	110
4.15	Simulated experiment environment.	112
5.1	Experimental platform	115
5.2	(a) The distortion model of the left camera. (b) The distortion model of the right camera.	119
5.3	Schunk Arm: all the joints are at home base.	120
5.4	Directions of the rotation of the seven joints.	121
5.5	D-H frames of the Schunk arm.	125

5.6	Inverse kinematics for a four DOF manipulator.	127
5.7	Plan View (seen from the z axis) of the four DOF manipulator. . .	128
5.8	ZR plane for the procedure of computing θ_2 and θ_3	129
5.9	Rocks used for experiment.	131
5.10	Top left image: this image was captured by the left camera. Top right image: this image was captured by the right camera. Bottom image: this image was the result of touchability computation. . . .	132
5.11	Top left image: this image was captured by the left camera. Top right image: this image was captured by the right camera. Bottom image: this image was the result of touchability computation. . . .	133
5.12	Left image: this image was captured by the left camera. Right image: this image was captured by the right camera.	134
5.13	Top left image: this image was captured by the left camera. Top right image: this image was captured by the right camera. Bottom image: this image was the result of touchability computation. . . .	135
5.14	Left image: this image was captured by the left camera. Right image: this image was captured by the right camera.	136
5.15	Top left image: this image was captured by the left camera. Top right image: this image was captured by the right camera. Bottom image: this image was the result of touchability.	137
5.16	Left image: this image was captured by the left camera. Right image: this image was captured by the right camera.	138
6.1	Colour image-based Martian rock detection and classification. Im- age Courtesy of ELSEVIER	145

List of Tables

1.1	ECSS autonomy levels vs space robot application.	20
2.1	Structure feature list (Table courtesy of (Pullan, 2006)).	37
2.2	Texture feature list (Table courtesy of (Pullan, 2006)).	38
2.3	Composition feature list (Table courtesy of (Pullan, 2006)).	39
3.1	Selected images for experimentation (Spirit Rover)	74
3.2	Qualitative comparison about 1.png and 2.png images amongst OTSU, Pugh's, Fink's and the present method.	76
3.3	Qualitative comparison about 3.png and 4.png images amongst OTSU, Pugh's, Fink's and the present method.	77
3.4	Qualitative comparison about 5.png and 6.png images amongst OTSU, Pugh's, Fink's and the present method.	78
3.5	Comparison of Precision for the four methods	79
3.6	Comparison of Recall for the four methods	79
3.7	Comparison of ME for the four methods	80
3.8	Distance of ToptoBottom (mm)	81
3.9	Distance of LefttoRight (mm)	82
4.1	Membership function levels for Size.	102
4.2	Membership function levels for Distance.	104
4.3	Membership function levels for SV.	106
4.4	Simulation experiment data.	111
4.5	Correspondence between SV and colour.	111
4.6	Simulation experiment result.	113
5.1	WACs specifications.	116
5.2	D-H parameters of the Schunk arm.	126
5.3	Results from experiment 1.	132
5.4	Results from experiment 2.	133
5.5	Results from experiment 3.	134
5.6	Results from experiment 4.	135
5.7	Results from experiment 5.	136
5.8	Results from experiment 6.	137
5.9	Results from experiment 7.	138

Chapter 1

Introduction

1.1 Background of the Research

Since there is a hostile environment such as dust and solar radiation on the Red Planet, currently it is inadvisable to send humans to perform the investigation of Mars that may endanger their life. Therefore, it is preferable to survey Mars with robotic technology. During the recent decades important technological developments have been made in the area of robotic exploration. Robotic applications range from search and rescue and oceanography to planetary science (Castano *et al.*, 2007a; Baxter *et al.*, 2007; Antonelli *et al.*, 2008). Modern unmanned planetary rovers are sent to acquire and make real-time decisions on how to explore their environment, and autonomously interpret the scientific data.

At the moment space robotic landers include Viking, Beagle 2 and Phoenix; and of course the planetary rovers such as Mars Pathfinder, Spirit and Opportunity, Curiosity. The Viking program was composed of two main parts: an orbiter designed to photograph the surface of Mars from orbit, and a lander designed to study the planet from the surface (Godwin, 2000). The lander conducted biological experiments designed to search for evidence of life in the Martian soil. Europe's first planetary mission incorporated an orbiter (Mars Express) and a lander (Beagle 2)(Pullan *et al.*, 2004). The lander (Figure 1.1) was equipped with a highly-integrated scientific payload designed to conduct in situ geological and astrobiology-related experiments at a landing site located within Isidis Planitia (Bridges *et al.*, 2003). Mission scientists used instruments aboard the Phoenix lander to search for environments suitable for microbial life on Mars, and to investigate the history of water there (Shotwell, 2005; Goldstein & Shotwell, 2009). The

Mars Pathfinder is a NASA spacecraft and consisted of a lander and a lightweight wheeled robotic Mars rover named Sojourner. The mission involved a series of scientific instruments to analyse the Martian atmosphere, climate, geology and the composition of its rocks and soil (Golombek, 1997; Squyres *et al.*, 2003). The Mars Exploration Rover mission (MER) began in 2003 with the sending of the two rovers (Spirit and Opportunity) to explore the Martian surface and geology. The mission's scientific objective was to search for and characterize a wide range of rocks and soils that hold clues to past water activity on Mars (Arvidson *et al.*, 2006; Squyres *et al.*, 2006). The Mars Science Laboratory mission (MSL) successfully landed on Mars on August 6, 2012, and consisted of a rover named Curiosity and a scientific payload designed to identify and assess the habitability, geological, and environmental histories of Gale crater (Anderson *et al.*, 2012; Grotzinger *et al.*, 2012). In short, all these missions will be heavily influenced by the Martian geology and environment, astrobiology and habitability in terms of payload, landing site and sampling strategies.

Rocks are one of the prime features exposed on the planet's surface and with regards to Mars rover missions, they play an important role in scientific investigation. Rocks carry considerable rich geologic clues for the study of planetary geology. According to the distribution and type of rocks, a geologist can conclude which regions may have similar rocks formed and deposited at the same time. Different rocks may have different physical parameters and appear in different location, which may be essential for the understanding of the Martian chemical elements and geologic environment. The present state of the rocks can tell us what has happened since their formation such as the influence of climate, erosion and transportation (Gor *et al.*, 2001). Rocks are one of the chief obstacles to endanger a rover traverse if they are not detected ahead of time accurately. Furthermore, rocks are also employed for vision-based localization and navigation as tie points. Consequently, the autonomous detection of rocks is a valuable capability for planetary geology survey and sample acquisition, and for hazard avoidance and rover localization and navigation in Mars mission operations.

1.1.1 ExoMars Programme

The Mars Sample Return (MSR) mission plans to collect samples of Martian rock, soil and gas for returning to Earth, and for carrying out scientific analysis (iMARS Working Group, 2008; Space Studies Board, 2011). In particular, ExoMars is

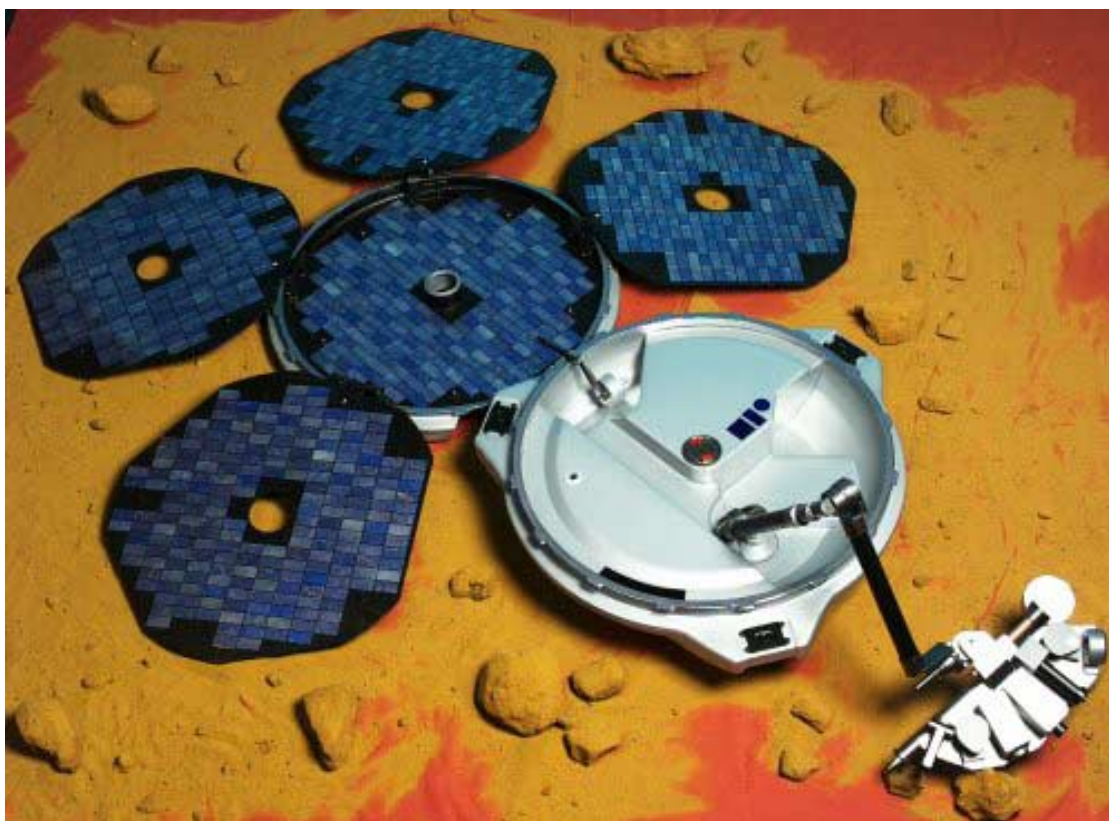


Figure 1.1: The Beagle 2 lander. The ARM would position the PAW whose calibration undertaken by Aberystwyth University to conduct panoramic, macroscopic and microscopic imaging, in-situ compositional analysis, and sample acquisition for the Gas Analysis Package (GAP) experiment (Barnes *et al.*, 2003; Barnes *et al.*, 2006). Image courtesy of ESA

scheduled for the forthcoming ESA/Roscosmos 2016 and 2018 missions, which can be regarded as precursor missions to MSR. The first mission will carry a Trace Gas Orbiter and an Entry, Descent and Landing Demonstrator Module (EDM), and will be launched and reach Mars in 2016. The second mission will carry a large capsule with a surface science platform and a rover to Mars in 2018 (<http://exploration.esa.int/mars/46048-programme-overview>).

The ExoMars campaign will demonstrate an amount of fundamental flight and in-situ enabling technologies, whose development objectives include:

- To enable Entry, Descent and Landing (EDL) of large payloads on Mars.
- To adopt solar electric power on the surface of Mars.
- To develop surface exploration mobility capability with a rover.

- To access to the subsurface for sample acquisition, preparation, distribution and analysis with a drill.

Meanwhile, a number of crucial scientific objectives are to be achieved, including:

- To search for possible signs of life on Mars, past and present.
- To investigate the water and geochemical distribution and environmental variations.
- To survey the surface environment and identify hazards for future manned missions to Mars.
- To study the Martian subsurface to better understand the habitability and evolution of Mars.

1.1.1.1 ExoMars Rover

The ExoMars Rover (Figure 1.2) developed by ESA hosts the primary mission abilities: surface mobility, subsurface drill and autonomous sample acquisition, processing, and deployment to instruments. It provides an analytical instrument suite called the Pasteur payload devoted to exobiology and geochemistry investigation. Solar panels are utilized to generate the electrical power required, and novel batteries and heater units are designed for the rover survival at the cold Martian nights. The ExoMars is of extreme automation. Scientists/operators on Earth just specify target locations from stereo images taken by the cameras mounted on the rover mast, then the rover will traverse to the designated location without human intervention. In order to achieve the navigation, navigational stereo cameras are employed for digital maps and then path planning is implemented.

The rover can safely traverse around 100 meters per sol with the help of navigation. The six wheels of the rover control its movement. Each wheel pair is suspended on an independently pivoted bogie. All wheels can be steered and driven individually and can be independently used to adjust the rover height and angle relative to the surface. Sun sensors are provided for the absolute attitude of the rover on the Martian surface and for the direction to Earth. The rover is equipped with a drill called the subsurface sampling device which can autonomously drill to the maximum 2 meters depth for gathering small samples. In the heart of the rover the analytical laboratory will analyse these samples when delivered. A fine powder will be obtained by crushing the collected samples. Detailed chemical, physical, and spectral analyses will be performed using the powder by means of the instruments.

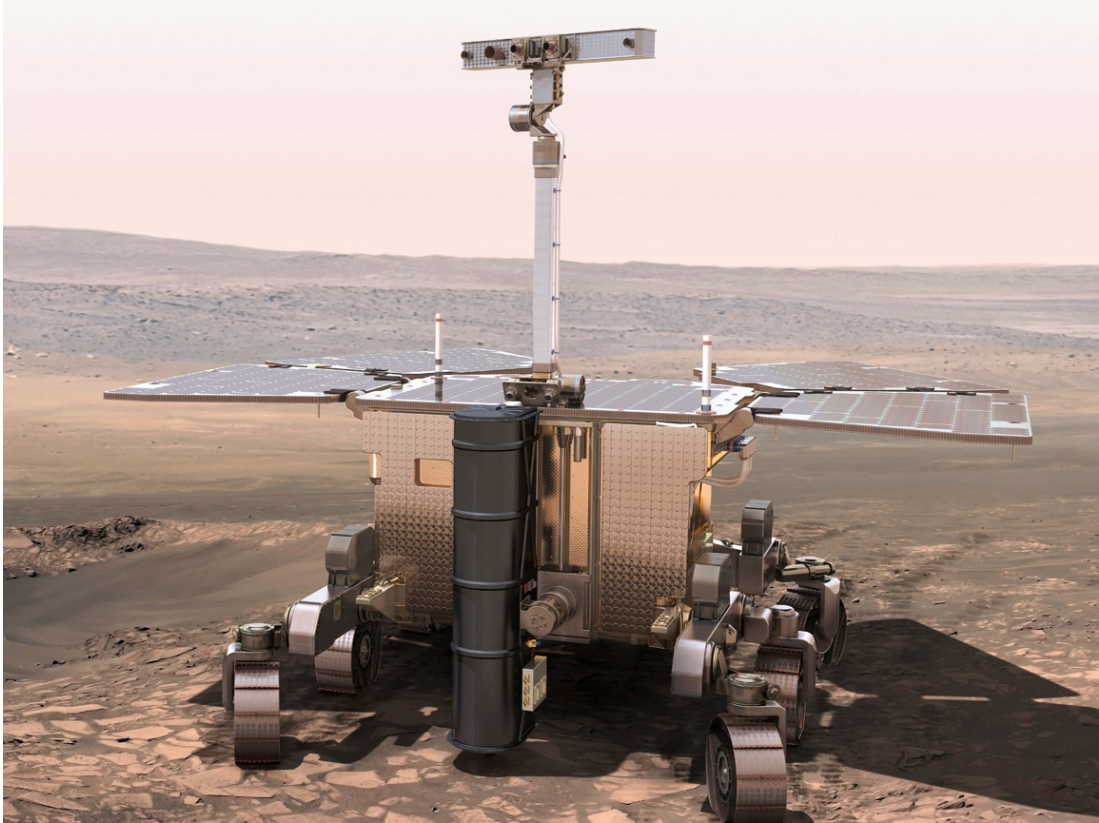


Figure 1.2: Artist's impression of the ExoMars rover. Image courtesy of ESA

1.1.1.2 ExoMars Instruments

The ExoMars rover is equipped with a comprehensive and coherent suite of analytical instruments dedicated to exobiology and geology investigation. The instrument suite is known as the Pasteur payload (PPL). PPL includes a set of complementary instruments, and has the following objectives: searching for signs of past and present life on Mars and researching the water/geochemical environment as a function of depth in the shallow subsurface (Debus *et al.*, 2010). The key instruments that will be comprised as part of the 2016 and 2018 ESA/Roscosmos ExoMars rover are:

- PanCam - The Panoramic Camera

PanCam is to conduct digital terrain mapping of Mars. It is composed of two wide angle cameras (WACs), one high resolution camera (HRC) and the Pancam interface unit (PIU). For panoramic imaging (34° field of view, fixed focus) WACs are equipped with a 12-position filter wheel each covering a different wavelength, thus enabling multispectral observations. HRC is used

for high-resolution colour imaging with 5° field of view, and is an autofocus mechanism. PIU as the brain of the instrument undertakes the communication with the rover (Pugh *et al.*, 2010; Barnes *et al.*, 2011; Pugh *et al.*, 2011; Cousins *et al.*, 2012).

- MOMA - Mars Organic Molecule Analyser
This instrument will target biomarkers to answer questions related to the potential origin, evolution and distribution of life on Mars.
- MicrOmega
This is a visible plus infrared imaging spectrometer for mineralogy studies on Martian samples.
- MARS-XRD - MARS X-Ray Diffractometer
A combined X-ray diffractometer and fluorescence spectrometer, which will be used to analyse the mineralogy and the chemical composition of the Martian rocks and soil.
- RLS - Raman Laser Spectrometer
The Raman instrument will be used to provide context information for the identification and characterisation of potential organic compounds which can then be related to present or past signatures of life on Mars.
- WISDOM - Water Ice and Subsurface Deposit Observation OnMars
This instrument under the rover is a ground-penetrating radar to explore the stratigraphy. WISDOM will be utilized in combination with Adron, which is able to provide information about subsurface water content, to decide where to acquire subsurface samples for analysis.
- MA_MISS - Mars Multispectral Imager for Subsurface Studies
MA_MISS located inside the drill will contribute to the study of the Martian mineralogy and rock formation.
- CLUPI - Close-UP Imager
CLUPI is a camera system and is capable of taking the high resolution colour close-up images of rocks, outcrops, drill fines and drill core samples.

- LMC - Life Marker Chip

LMC will be utilized to detect specific molecules that may be concerned with Martian life at past or present.

- Adron

Adron is developed to seek subsurface water and hydrated minerals, and will be used with WISDOM to study the subsurface beneath the rover and to search for suitable areas for drilling and sample collection.

1.2 Need for Autonomous Systems

Currently, since all extra-terrestrial planets which have been explored and observed commonly have large changes in temperature, unstable weather systems and very thin atmospheres, they are inhospitable for human beings. It is well known that only Earth has liquid water compared with the other observed planets and has the appropriate amount of oxygen to sustain life. However, as regards to planetary exploration these are by no means the only problems that human beings face. The main problem is how to travel to the planet. The length of time that it would take to travel from Earth to Mars for a spacecraft relies heavily on the relative orbits between both planets. Any journey would be a minimum of a six month. During the journey the crews have to be fed, warmed, shielded from radiation. Waste products must be dealt with and oxygen is stored for use during the whole mission. Fuel for launches and landings have to be available. It is significant that the current technologies would make it nearly impossible for astronauts to return on the same spacecraft which landed on Mars. A huge number of technologies and resources would be needed to equip for the entire mission. It is mainly for these reasons that robotic platforms have become the key tools when it comes to planetary exploration.

Originally, in-situ landers were sent to Mars such as the Viking Landers (see Figure 1.3A). Since it was found that a very limited amount of science could be implemented only from the landers, mobile platforms were built, the first being a lander like Mars Pathfinder and the Sojourner Rover (see Figure 1.3B). Success in using the mobile platforms with regard to scientific return

has resulted in an increase in the use of the mobile platforms as the MER rovers (see Figure 1.3C) and the Curiosity rover (see Figure 1.3D).

Certainly, the amount of science return that can be delivered by a current robotic platform is fully less than can be achieved by an on site human expert. Any measures that are able to maximize the amount of science return must be contemplated seriously. Given this situation, then the way forward is maximum autonomy for exploration devices. In this way it is that autonomy can avail for planetary exploration. With increasing autonomy a lot of decisions which are currently made by scientists and operators on Earth can be made from the exploration platforms. This would reduce the amount of communication between ground control and the robotic platform and also would allow optimisation of the workload of a platform. This would in turn reduce the need for pauses and times of inactivity. These pauses typically occur at decision points when a command sequence has been accomplished and the images have to be processed before the next move of the platform can be decided (see Figure 1.4). An autonomous system can make this decision and move to the next sample location. The communication bandwidth can be specifically devoted to the return of valuable scientific data that include poor images and other lower priority images of limited value. The European Cooperation for Space Standardisation (ECSS) gave a definition of robotic autonomy in a planetary exploration context (see Table 1.1). An autonomous system can be assessed by these levels as a unified scale.

1.2.1 Benefits of Full Autonomy

In order to achieve level E4 (see Table 1.1) of autonomy, a robotic system will have to perform goal-orientated re-planning within an unstructured environment without human guidance. Therefore, it can be said that an autonomous robotic system at level E4 has to be able to:

- Gather information about the environment.
- Work for an extended period without the need for human interaction.
- Move either all or part of itself through a changing environment without human assistance.
- Avoid damaging people, property, or itself.

Table 1.1: ECSS autonomy levels vs space robot application.

Level	Description	Functions
E1	Mission execution under ground control. Limited on-board capability for safety issues	Real-time control from ground for nominal operations. Execution of time-tagged commands for safety issues.
E2	Execution of pre-planned, ground defined, mission operations on-board.	Capability to store time-based commands in an on-board scheduler.
E3	Execution of adaptive mission operations on-board.	Event-based autonomous operations. Execution of on-board operations control procedures.
E4	Execution of goal-orientated mission operations on-board.	Goal-orientated mission re-planning.

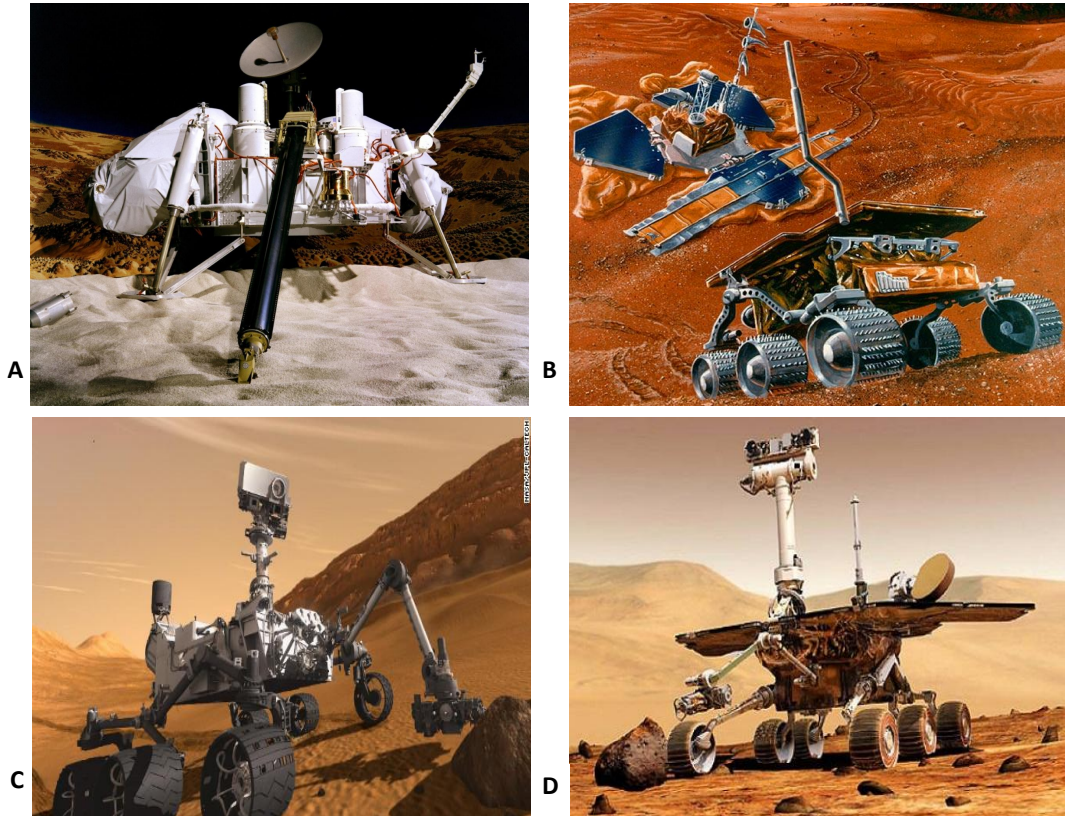


Figure 1.3: Artists rendition: A. Viking Lander, B. Mars Pathfinder and Sojourner Rover, C. MER Rover, D. Curiosity Rover. Composite images courtesy of NASA/JPL

Understanding this helps illustrate why this level of autonomy is so hard to achieve. Figure 1.5 illustrates the results of moving all Earth-bound decision points to the exploration platform. The exploration platform can use both communication windows to download images and telemetry to Earth. No input from Earth is necessary, although Earth-bound contact would be needed to update the platforms goal list.

This approach would also reduce the need for pauses in execution. The platform can work as long as it has power available. An added benefit would be to minimise ground-based operator workload, as Earth-bound scientists would have less involvement during the sample selection stages. Low quality images and work-flow images need not be down-linked at all, resulting in a reduced administration and archiving workload. Amortized primary mission NASA Mars Exploration Rover (MER) operations have been reported to cost approximately \$4 million to \$4.5 million per day and require 240 operators working 24/7 (Pedersen *et al.*, 2005). If a reduction in the number of operators and scientists needed to assess down-linked data could be achieved, a significant reduction in mission cost would be possible thus reducing the overall cost of the science achieved during the mission.

1.2.2 Benefits of Limited Autonomy

Limited autonomy is more achievable, and in some ways more acceptable as scientists are still uneasy about delegating control of the mission to the exploration platform. It has been essential for some time that certain aspects of the exploration platform be autonomous; for example the deployment of the on-board communication aerial (Jansson *et al.*, 2007). As technology advances and human acceptance towards robotic autonomy grows, more and more mission operations could move towards autonomy. Currently no science or targeting decisions have undergone this transition. This is primarily because of the difficulties involved in categorizing potential targets in the remote terrain. Significant advancements have been made in the instrument placement (Pedersen *et al.*, 2005) and Rover navigation domains (Laurent & Michel, 2006). Figure 1.6 illustrates a scenario where both autonomous navigation and instrument placement are in use. The initial target is selected on Earth in the traditional way. By moving the navigation on-board,

the rover need not wait for Earth based computers to calculate a safe path to the target, or to produce a final DEM (Digital Elevation Model) of the sample. This would all be accomplished on board. Instrument placement could take place as soon as the vehicle is in position. The only Earth-bound operation would be to select suitable targets for sampling, thus reducing the need to provide the platform with any contextual information about its surroundings or mission objectives. Thus the complexity of the problem is substantially reduced.

1.3 Research Aim and Objectives

Rocks as science target are one of the main features exposed on the Martian surface, which play an important role in scientific research and engineering operation for Mars rover missions (such as the study of planetary geology, and the evaluation of the information content in Mars images to identify major obstacles for Martian rover traversing)for Mars rover missions. This research aims to analyse Mars images by means of image processing and computer vision techniques, and to develop a method for autonomous science target detection.

The current strategy employed by MER and MSL is that a science target is deemed to be able to be acquired just when it is within the robotic arm workspace, which is a mechanical decision strategy. Hence, this research aims to develop an autonomous flexible approach to adjusting automatically the robotic arm workspace in terms of the science value score (SV) for a potential scientific goal. In addition, due to the fact that Mars images may well be captured with uncertainty and imprecision owing to the natural environment in which a Martian rover functions, any tool to be developed in handling such images will have to address the inherent uncertain and imprecise information, data and knowledge.

Thus, the main aims of my research are as follows: To design and develop a Mars surface science target touchability evaluation architecture through the use of a fuzzy logic control structure, and to guide the actions of the rover for planetary exploration.

The objectives of this research can be summarised as follows:

1. Design and develop a rocks identification algorithm, and conduct experiments to validate the effectiveness of the algorithm using field images and Mars images.
2. Develop a desired keypoint matching algorithm for calculating the size of an identified rock and the distance between the arm base and the target.
3. Design and develop a touchability evaluation algorithm, and validate the effectiveness of this algorithm through simulation.
4. Build upon the experiment platform and perform experiments using the real rock data to validate the effectiveness of the above method.

1.4 Thesis Outline

The rest of this thesis has been divided into the following five chapters, which are organised as follows:

- **Chapter 2** In this chapter, four current autonomous science solutions are reviewed and discussed, including: On-board Autonomous Rover Science Investigation System (OASIS) project (Castano *et al.*, 2007b), the Single Command Approach and Instrument Placement (SCAIP) project (Schenker *et al.*, 2003), the Collaborative Research in Exploration and Technology (CREST) project (Shaw *et al.*, 2007), and the Robotic Antarctic Meteorite Search (RAMS) project (Pedersen, 2000). These four projects represent the current state of the art as regards autonomous science systems for planetary/terrestrial exploration.
- **Chapter 3** The chapter not only presents an unsupervised segmentation approach about the Mars images based upon an improved OTSU and Canny operator (Otsu, 1979) (Canny, 1986), but also introduces a technique for measuring the size of the rock based on the SIFT-RANSAC (Scale Invariant Feature Transform - Random Sample Consensus) algorithm (Lowe, 2004) (Fischler & Bolles, 1981) and the cross correlation method (Tsai & Lin, 2003).
- **Chapter 4** The chapter describes a fuzzy logic-based touchability system in detail for the following instrument deployment. In this system

the five linguistic variables (Size, Distance, Science Value, Orientation and Touchability Index) have been extracted, and their membership functions have also been built.

- **Chapter 5** In this chapter, in order to test and verify the validity of the proposed touchability system the laboratory experiments are described on the basis of the hardware assembly which includes two wide-angle cameras (WACs), Schunk arm, real rocks, camera mast and optical bench.
- **Chapter 6** A discussion of the achievements of this research is presented, future direction of the study is proposed and potential areas of improvement are identified.

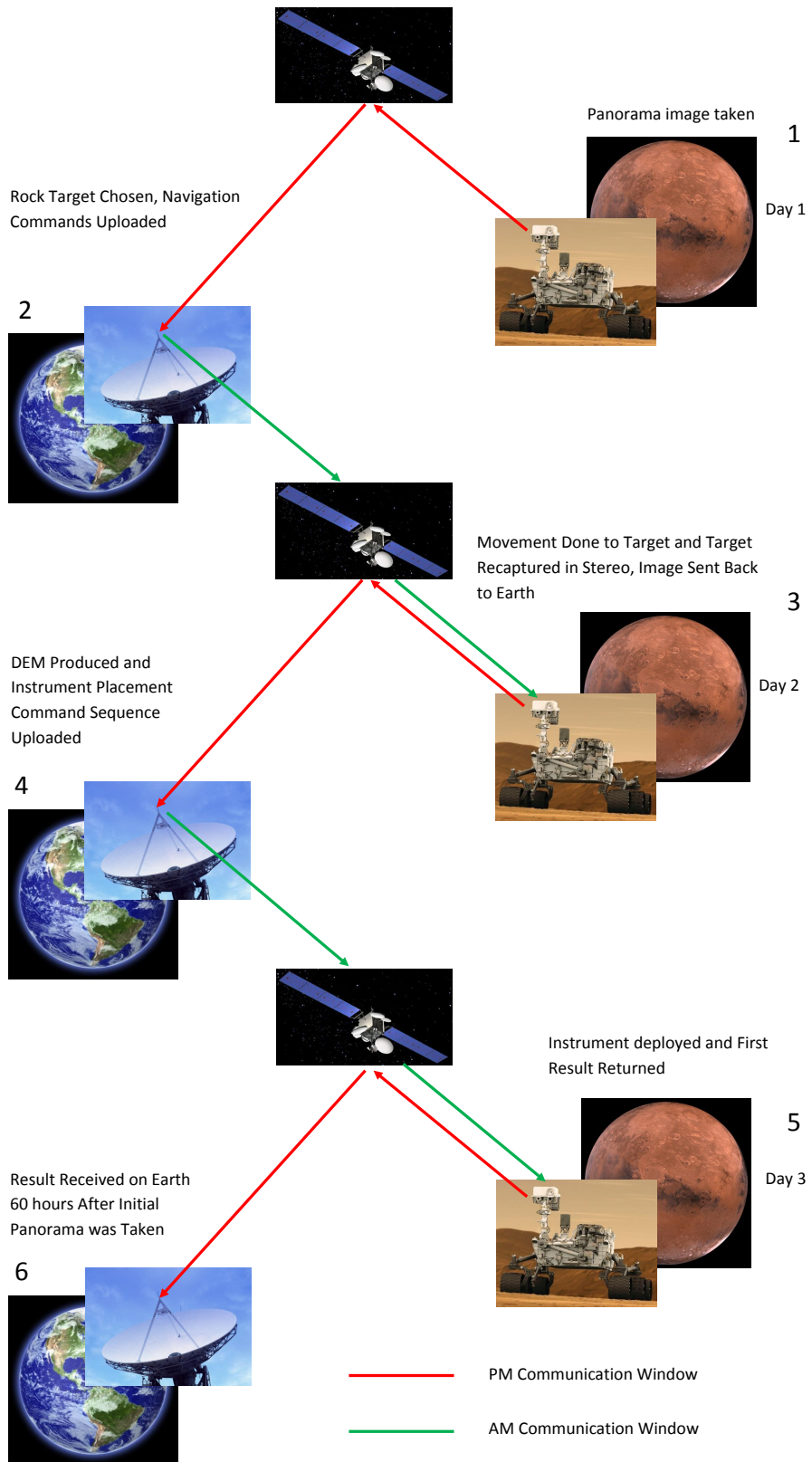


Figure 1.4: Rover to Earth communication during the representative instrument placement. Composite images courtesy of NASA/JPL

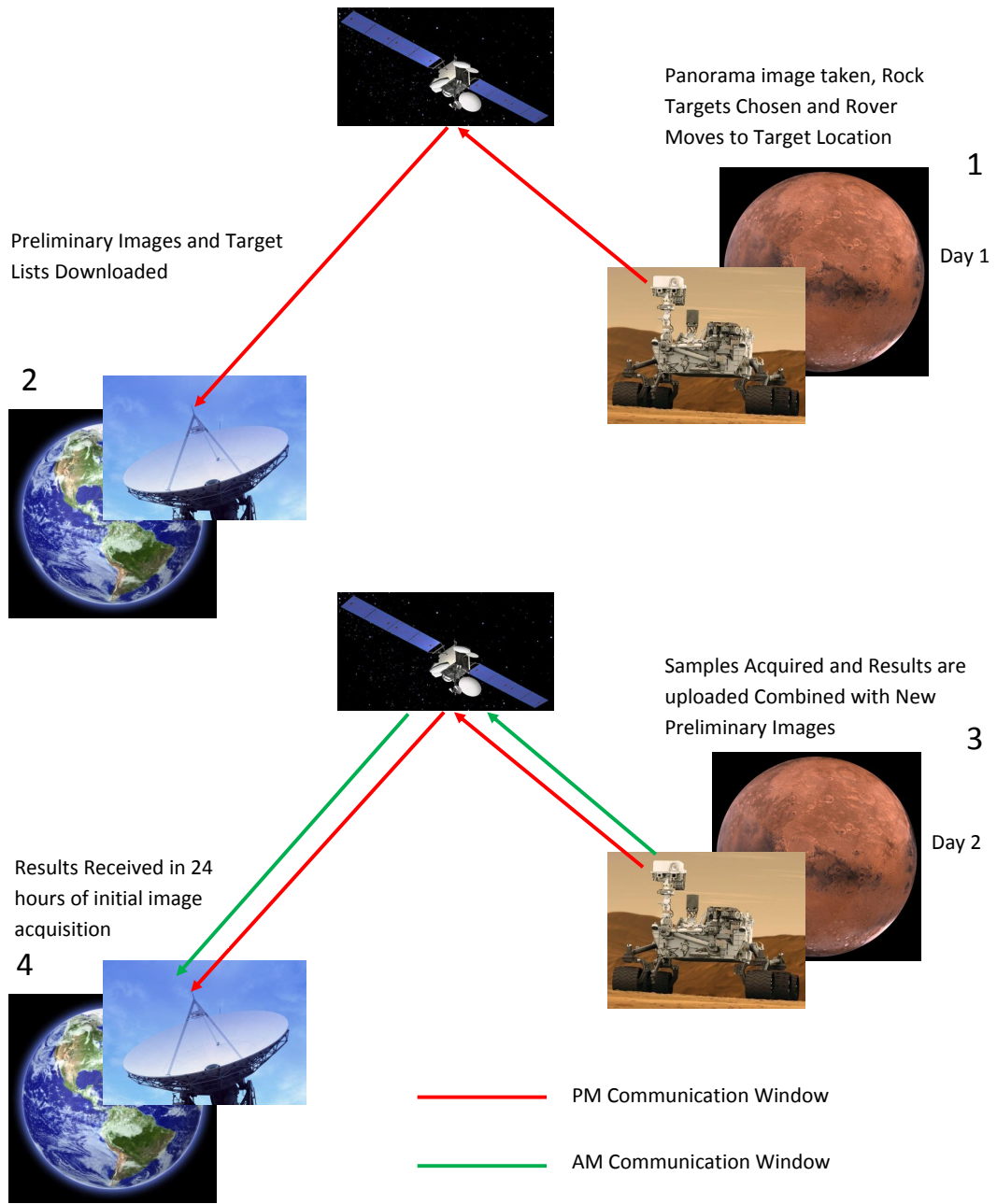


Figure 1.5: Rover to Earth communication during instrument placement, a fully autonomous system E4. Composite images courtesy of NASA/JPL

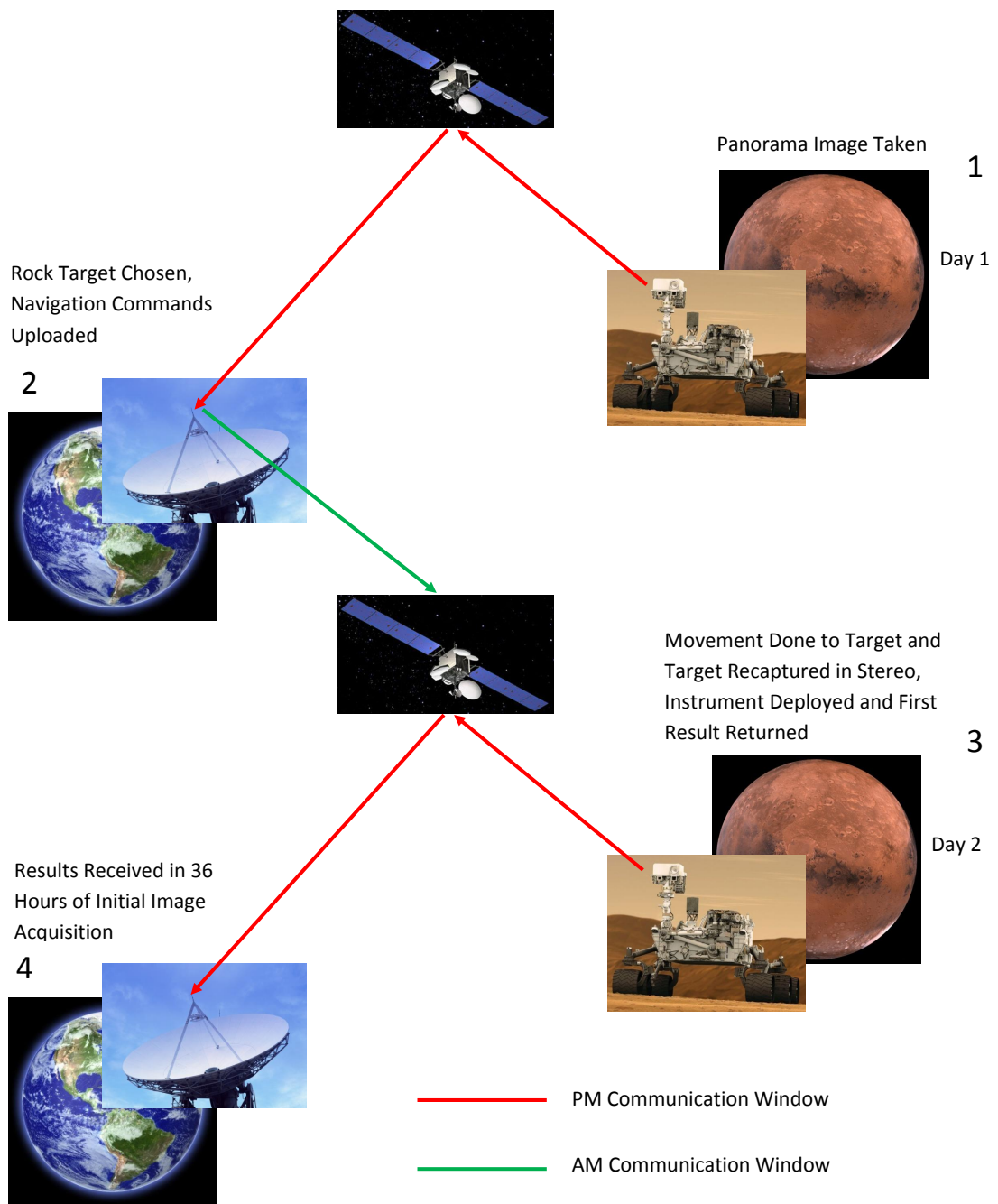


Figure 1.6: Rover to Earth communication during instrument placement, a semi-autonomous system with ground based target decisions E3. Composite images courtesy of NASA/JPL

Chapter 2

Autonomous Science Systems

Autonomy in space has become a desirable capability. There is extensive research being undertaken in the field to endow robots with the autonomy necessary to explore a remote, relatively poorly characterized extra terrestrial environment. This chapter is focused upon the research that has been undertaken in the area of autonomous science which sets the background for the present work. There are a number of key projects that are described in the following sections. These projects are of direct relevance to the present research. However, due to the specialism the literature is rather limited in developing the relevant techniques for the problem that is addressed herein.

2.1 Robotic Antarctic Meteorite Search (RAMS)

The Robotic Antarctic Meteorite Search (RAMS) is a Carnegie Mellon based project concentrating upon developing robotic technologies to facilitate an autonomous rover in the search for meteorites in Antarctica. Antarctica has been chosen as a base location for this project because of its richness of well preserved and easily accessible samples. This is caused by the predominant environmental conditions experienced in the region. The moving glaciers bring deposited rocks to the surface and the cold dry conditions delay their degradation (Pedersen, 2000). The study has been built around a robotic platform known as Nomad (see Figure 2.1) which has been outfitted and prepared to deal with the harsh environment of the Antarctic (Apostolopoulos

et al., 2000). It has also been equipped with a high resolution camera and a visible to near infrared reflectance spectrometer (Pedersen *et al.*, 1998). The purpose of these upgrades are to enable Nomad to operate autonomously for extended periods and carry out an unaided search for meteorite samples. A Bayes network approach has been adopted to facilitate rock classification and a Markov chain segmentation approach to segment the captured images.



Figure 2.1: Image of Carnegie Mellons Nomad Rover (Image courtesy of Carnegie Mellon). Nomad is a 4 wheel drive rover measuring $2.4 \text{ m} \times 2.4 \text{ m} \times 2.4 \text{ m}$, and has a total mass of just over 700 kg

2.1.1 Image Segmentation

Image segmentation for the RAMS project is made easier by the environment. The land is covered with snow and ice and is therefore white. Rocks and meteorites which are brought to the surface by glacial motion are usually quite dark in colour and stand out quite clearly from their background. It is still a non-trivial problem as rock shadows and partial snow cover can

degrade results. As previously mentioned a Markov chain segmentation approach was adopted to try and alleviate this problem. The Nomad rover camera system has been designed to provide images along with scale information and a centroid of all rock-like pixel areas (Pedersen, 2000). It is assumed that no rocks are close together and all rocks are fully surrounded by their ice background. The work of (Pedersen, 2000) asserts that if pixels are examined along a radial projecting out from the centroid in sequence at some unique point they cease being a rock and start becoming ice or background pixels. In this work this sequence is modelled by a partially observable Markov Chain.

2.1.2 Rock Classification

At the core of the RAMS system lies the rock classification agent. It encapsulates the system's scientific knowledge. Its goal is to use sensor data to classify targets as belonging to one of the pre-defined categories/types (Apostolopoulos *et al.*, 2000). It also calculates the potential information gain that could result from deploying additional sensors. The classifier is responsible for deciding based upon gathered sensor data whether a processed target is a terrestrial rock or a meteorite. This is non trivial as it is very difficult for expert geologists to classify what they are looking for. The common analogy of not knowing exactly what you are looking for until you find it is quite fitting. The problem will also change as the area being investigated changes and environmental conditions fluctuate. In order to deal with this issue an adaptive learning approach has been adopted.

The initial problem with this approach is the limited number of available training targets. In an attempt to alleviate this issue two earlier expeditions to Antarctica along with trips to the Arctic and the Atacama desert in Chile were conducted to search for additional samples to use as training data. Prior application specific data was also included in to the classifier in order to compensate for the limited amount of training data.

The robot also has several deployable sensors which must be deployed in turn. Some of these sensors have a high deployment cost associated with them (such as the micro spectrometer, which requires the rover to move to locate the sample in the target envelope) so it is desirable not to deploy

them unless it is deemed that they will add beneficial data.

2.1.3 Bayes Network

The RAMS development team stipulate that a Bayes network based approach fits well with this problem. The benefits put forward by (Pedersen, 2000) are presented below:

- The classification of uncertainty and any ambiguity is handled by computing explicit probabilities for each possible rock class, rather than just the most likely.
- Evidence from sensor readings can be incrementally compounded by Bayesian updates.
- Prior rock and meteorite probabilities in a specific area are accounted for.
- The structure of a Bayes network reflects the statistical relationships between rock samples and sensor measurements. These have been deduced from knowledge of geology and the physics of the sensors. This has allowed the relationships between variables to be constrained by domain specific knowledge, and the intrinsic dimensionality controlled.
- Given a suitable network structure, the statistical model can be learned from statistically biased training data available.

(Pedersen, 2000) shows how the Bayes network based generative model can be extended to allow autonomous profiling of the environment in order to learn rock probabilities and exploit the correlations amongst the rock samples in a certain area. Furthermore, in addition to being able to handle incremental data, a Bayes network can be used to determine which unused sensors are likely to be useful to classify a sample, enabling active sensor selection, reducing unnecessary deployments of sensors.

2.1.4 Final Notes on RAMS

RAMS is a good example of an autonomous exploration vehicle. It has produced excellent results in Antarctica during several different field trials,

responsible for the first autonomous discovery of a meteorite. However, the discovery and classification of targets in Antarctica on the ice and snow is significantly different from discovery and classification of targets on Mars (or any other extra terrestrial body). The Bayes network used in this work has preformed relatively well in this situation, but it requires the user to pre-define what target types will be encountered so the system can categorise rocks into them. There appears to be no way to characterise the science value of a never before encountered target. This presents a substantial weakness should a system like this be used to classify unknown rock types in an unpredictable environment. The system has also been designed to classify targets based on their rock type, as a result a marble target would receive a value which would be different to a meteorite or a granite sample. This is suitable for the RAMS system but would not be suitable for an autonomous extra-terrestrial exploration vehicle as a rock type in a particular configuration (e.g., outcropping) is potentially more valuable than the same rock in a different configuration (e.g., boulder field).

2.2 CREST Autonomous Robotic Scientist (ARS)

The UK PPARC (now STFC) funded the Collaborative Research in Exploration and Technology (CREST) scheme to support preliminary technology development for ExoMars instrumentation and to position the UK industry to compete for ESA contracts. This project focused on the production of a framework to enable a robotic scientist to discover opportunistic science autonomously (see Figure 2.2). In order to accomplish this goal several intermediate aims were identified (Shaw *et al.*, 2007), which are given as follows:

- Establish an initial scientific methodology for the automation of science assessment and planning based on a human field practise.
- Prototype a system architecture which can support the concept of autonomous science.
- Prototype elements of the methodology provided by the science team in order to establish the feasibility of this approach.

- Demonstrate the prototype system in a representative Mars Yard environment.
- Use the forthcoming ESA ExoMars mission as a target and source of operations and science results.

The primary task was to demonstrate opportunistic science in a representative ExoMars type environment. The work presented by the project was to demonstrate that a mobile platform could traverse a rock field en-route to a target destination, both detecting and responding to targets of scientific interest that were encountered en-route (Woods *et al.*, 2009; Woods *et al.*, 2008).

In order to accomplish this, an extensive architecture of planners and agents had to be produced and integrated (see Figure 2.3). The basic operation or usage of this model is as follows:

- Nominal exploration time-lines or plans are up-linked from the mission control centre.
- The rover executes the planned sequence which is mainly a traverse action between designated way-points.
- At selected points the imagery collected during the traverse is assessed for science interest.
- If sufficient interest is detected, the science component will request a more detailed analysis via the time-line validation and control (TVCR).
- TVCR is to assess the current plan, resource state and mission priorities before recommending a go/no go for the new opportunistic science request.
- The request may involve a close-up image activity or an actual ARM placement on a target object such as a rock or outcrop.

2.2.1 Science Assessment and Response Agent (SARA)

The SARA is responsible for the identification and assessment of scientific targets within the CREST architecture (see Figure 2.3). In this section the SARA agent is documented in isolation from the rest of the system.

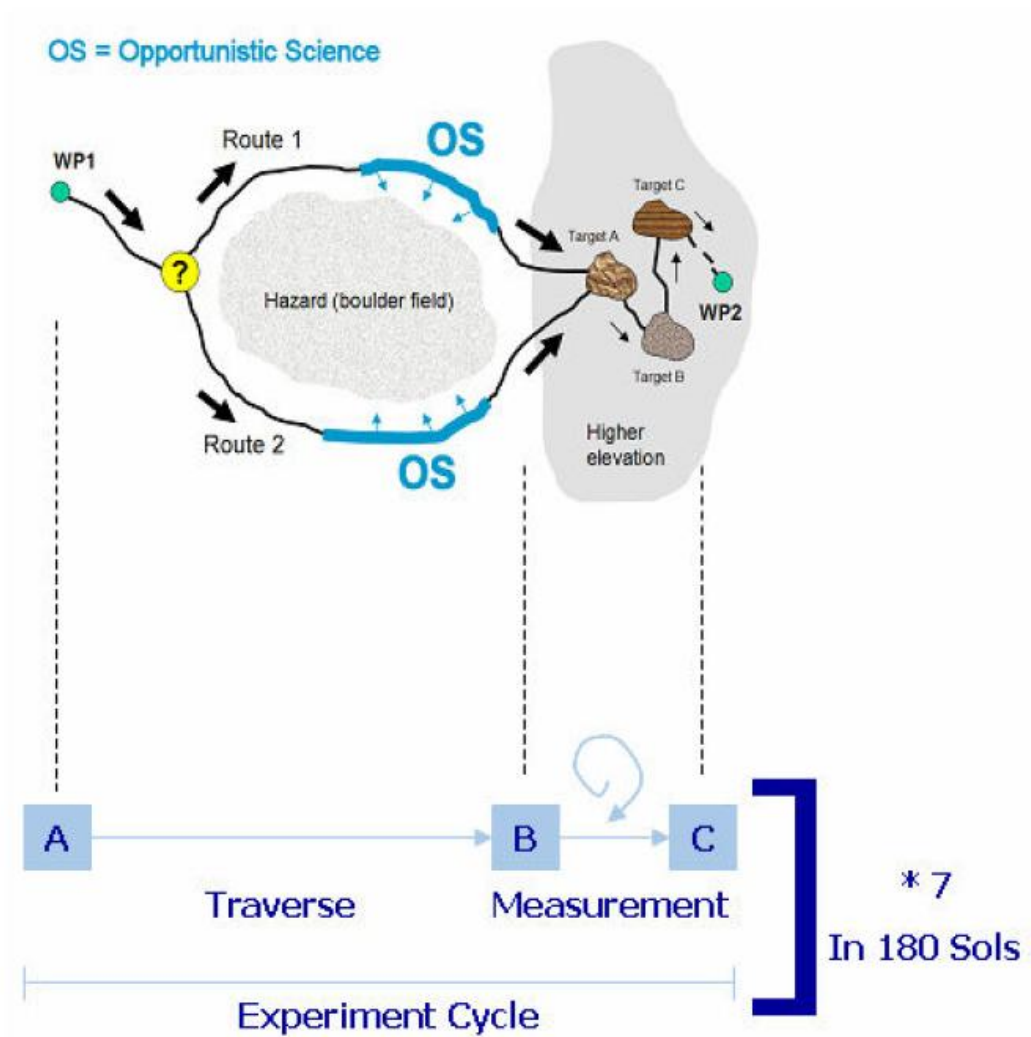


Figure 2.2: Opportunistic science aims of CREST (Image courtesy of SciSys, (Woods *et al.*, 2009)). This image outlines a basic ExoMars exploration cycle, showing the potential for opportunistic science activities. The main objective is to traverse from a previously explored site (A) and progress toward the next site at B, where detailed sample assessment will be carried out. The intention is to visit seven sites over the nominal 180-sol period. Opportunistic science is clearly possible during the traverse phase and could be used to improve the robustness of data acquisition and prioritisation during the measurement cycle.

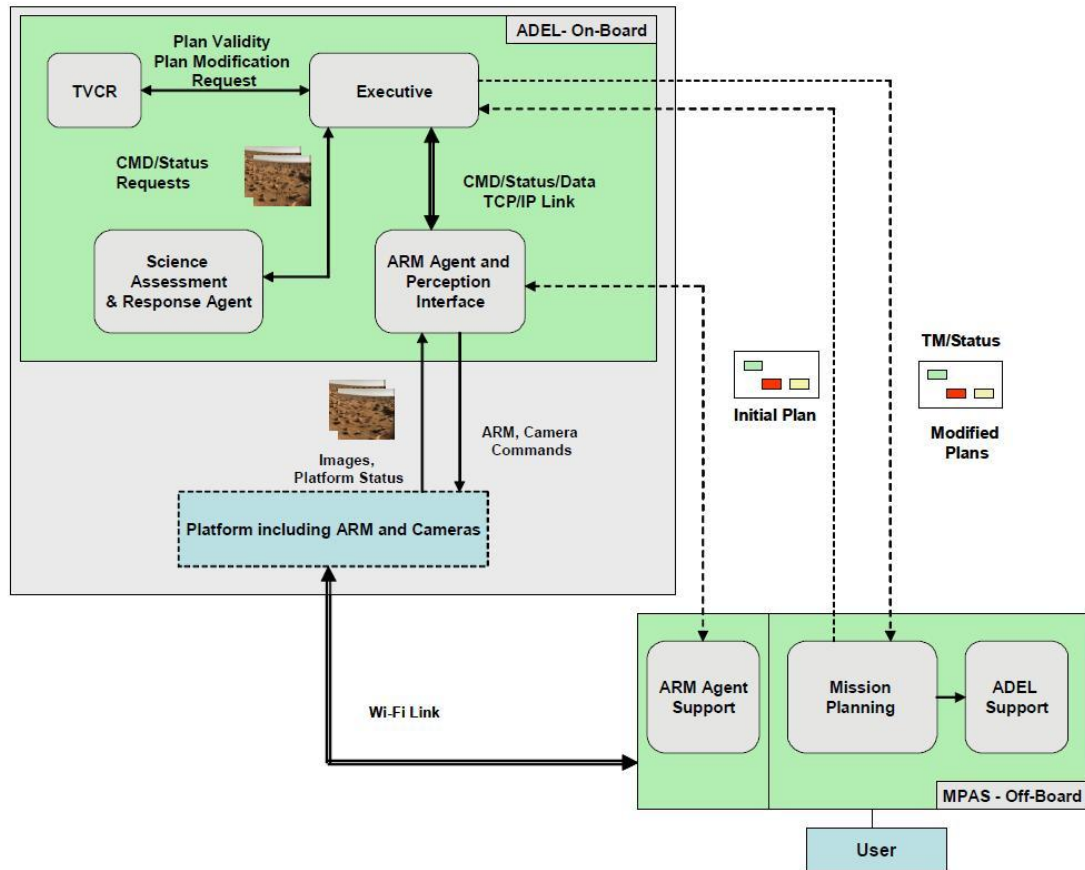


Figure 2.3: CREST Project Architecture (Image courtesy of SciSys (Woods *et al.*, 2009))

2.2.1.1 Science Assessment Framework (SAF)

The SARA is based on an underlying scientific scoring framework outlined in (Pullan, 2006). Within the afore mentioned report, a planetary geologist domain expert Dr Derek Pullan put forward a science assessment framework (SAF) to unravel the often complex process that a human expert goes through to assess a potential scientific target. The expert asserts that three primary attributes of a potential target can be used to determine the science value of that target. These three primary attributes can then be further broken down and characterised by a group of predefined features. The expert has gone further and produced a scoring system to characterise the scientific value of individual features such as albedo, colour and shape. The full list of features can be seen in Tables 2.1, 2.2 and 2.3. Once these features are identified and scored they can be combined using the following sum:

$$SVS = (\sum Structure + \sum Composition + \sum Texture + CompositeAttributeScore) * Quality * Bias$$

CompositeAttributeScore is a score which can be given to a composite group of related attributes which alone in isolation do not provide much value but when combined produce a desirable target. The Quality value can be used to represent the quality of the image or of an identified target, this value is generally used to degrade the targets score by multiplying the score by a factor smaller than 1. Bias is used to represent a scientific bias towards sampling certain kinds of targets. If for example the system had identified a basalt bomb as being a high priority target during an initial run, it will degrade its value during future observations.

2.2.1.2 Science Agent

The science agent's architecture is shown in Figure 2.4. Target detection is achieved through the use of a segmentation algorithm. Once these targets are identified they are processed and scored according to the data provided by the expert in the science assessment framework. Currently the system analyses six individual features: two from each of the three primary attributes (Structure, Composition and Texture). Once the scores of these six features are derived, they are combined by summing the totals together.

2.2.2 Final Notes on CREST

The CREST Robotic Scientist project has demonstrated an end to end implementation of an autonomous opportunistic platform. It has proved the concept of the Science Assessment framework produced by (Pullan, 2006). It has also proved the concept of a geology based image assessment of potential science targets. It is still at an early stage and as yet does not implement any sophisticated method of assessing the science values obtained from the Science Assessment Framework (SAF). This is due to the focus of the system being primarily on the image processing aspects responsible for identifying the features that are present, currently a simple summation of the SVS is carried out. This will limit the system's ability to deal with uncertainty as it is not possible to partially discover anything, either it is or it is not there. It has also been suggested that at a later stage the context of the images processed by the system will be considered by a learning technique,

Table 2.1: Structure feature list (Table courtesy of (Pullan, 2006)).

ID	Feature	SVS	Note
S000	Signature: No structure	0	Not available or beyond resolution
S001	Signature: Structural	5	Clasified or unclassified
S002	Quality: Distinct signature	15	Sharp or enhanced by weathering
S003	Quality: Indistinct signature	10	Poor resolution or masked by drift
S004	Stratification: Continuous	20	Continuous within context of FOV
S005	Stratification: Discontinuous	10	Discontinuous within context of FOV
S006	Type: Planar	10	
S007	Type: Wavy	50	
S008	Type: Curved	20	
S009	Type: Lenticular	40	
S010	Type: Irregular (smooth)	30	
S011	Type: Irregular (chaotic)	60	Includes draped
S012	Type: Nodular	50	Includes slumped
S013	Sub-type: Parallel	10	
S014	Sub-type: Sub-parallel	30	
S015	Sub-type: Non-parallel	50	
S016	Scale: Very thick (bedding)	100	> 100cm
S017	Scale: thick (bedding)	100	30cm to 100cm
S018	Scale: Medium (bedding)	10	10cm to 30cm
S019	Scale: Thin (bedding)	10	3cm to 10cm
S020	Scale: Very thin (bedding)	10	1cm to 3cm
S021	Scale: Thick (lamination)	10	0.6cm to 1cm
S022	Scale: Medium (lamination)	10	0.3cm to 0.6cm
S023	Scale: Thin (lamination)	50	0.1cm to 0.3cm
S024	Scale: Very thin (lamination)	100	< 0.1cm
S025	Orientation: Horizontal	10	
S026	Orientation: Inclined (left)	10	
S027	Orientation: Inclined (right)	10	
S028	Orientation: Vertical	10	

Table 2.2: Texture feature list (Table courtesy of (Pullan, 2006)).

ID	Feature	SVS	Note
T000	Signature: No texture	0	Not available or beyond resolution
T001	Signature: Textural	5	Clasified or unclassified
T002	Quality: Distinct signature	50	
T003	Quality: Indistinct signature	5	
T004	Fabric: Random	5	Continuous within context of FOV
T005	Fabric: Orientated	50	Discontinuous within context of FOV
T006	Fabric: Imbricated	100	
T007	Surface: Dull	5	
T008	Surface: Polished	50	Aeolian weathering (desert polish)?
T009	Surface: Rough	10	
T010	Surface: Striated	50	Aeolian weathering?
T011	Surface: Concoidal	100	Glassy fracture planes
T012	Surface: Vesiculated	10	Gas bubbles (lava)
T013	Surface: Pitted	40	Blueberry casts
T014	Surface: Bumpy	50	Blueberries in outcrop

which will then influence the SVS based on contextual information derived from the mission requirements and from the recent system activity.

The system has been demonstrated working in the Aberystwyth University PAT-Lab (Woods *et al.*, 2009) with a successful outcome, there is also evidence within the literature of SARA being run on MER images and successfully identifying potential high value science targets. There is however little characterisation of the quality of the achieved results against that of a planetary geologist expert.

2.3 Single Command Approach and Instrument Placement (SCAIP)

Closed Loop Control for Autonomous Approach and Placement of Science Instruments by Planetary Rovers or “Single Command Approach and Instrument Placement” (SCAIP) was a project also led by JPL to create a closed loop system to autonomously place a scientific instrument on a foreign planetary surface. The

Table 2.3: Composition feature list (Table courtesy of (Pullan, 2006)).

ID	Feature	SVS	Note
C000	Signature: None	0	Not available or beyond resolution
C001	Signature: Discernibly	5	Classified or unclassified
C002	Quality: Distinct	100	
C003	Quality: Indistinct	50	
C004	Reflectivity: Low albedo	10	
C005	Reflectivity: Medium albedo	50	Ice ($\sim 35\%$)
C006	Reflectivity: High albedo	100	
C007	Reflectivity: Low specularity	10	
C008	Reflectivity: Medium specularity	50	Crystallographic surfaces
C009	Reflectivity: High specularity	100	Mirror-like
C010	Distribution: Homogeneous	10	
C011	Distribution: Heterogenous	50	
C012	Colour: Red	0	
C013	Colour: Green	100	
C014	Colour: Blue	20	
C015	Colour: Black	50	Fresh mafic or primitive material?
C016	Colour: White	50	Salt or ice?
C100	Mineralogy: Carbonate	9999	First discovery?
C101	Mineralogy: Jarosite	50	Acid aqueous formation
C102	Mineralogy: Pyroxene	20	
C103	Mineralogy: Ilmenite	20	Ti
C104	Mineralogy: Goethite	5	
C105	Mineralogy: Hematite	10	Aqueous formation
C106	Mineralogy: Gypsum	5	Evaporite
C107	Mineralogy: Phyllosilicate	200	Clays (neutral/alkaline formation?)
C108	Mineralogy: Kamacite	200	Meteorite
C200	Petrology: Basalt	10	
C201	Petrology: Andesite	50	
C202	Petrology: Carbonaceous chondrite	200	Meteorite

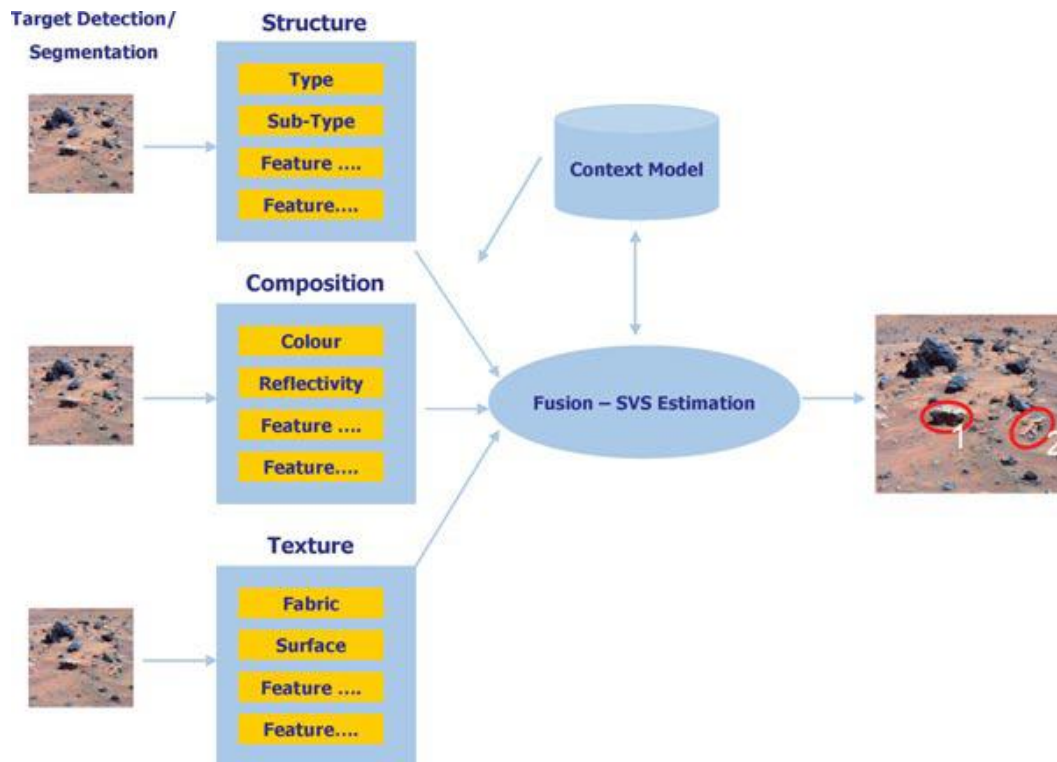


Figure 2.4: SARA architecture (Image courtesy of SciSys (Woods *et al.*, 2009))

main aim of the SCAIP project was to cut down the length of time required to take a sample. This was achieved by reducing the level of human interaction with the rover thus reducing the amount of time required for transmission of intermediate data and control instructions.

This system, although not a complete solution, focused upon the autonomy associated with the rovers command sequence. It assumed that an Earth based scientist had already specified a suitable target from down-linked images. The system would then proceed through a six stage sequence. The stages were as follows:

- Drive to stand-off position using interest points.
- Hand-off goal position from Navcams (navigation cameras) to Hazcams (hazard cameras).
- Plan final approach path.
- Drive to final offset position and acquire Hazcam image.
- Plan arm path with collision checks.

- Place instrument and acquire science data or determine a safe substitute placement goal.

The SCAIP control software gave primary importance to mission safety. If rover safety could not be guaranteed the rover would simply stop and call Earth for help. The system showed great promise. Figure 2.5 shows an image overlaid with yellow crosses showing an earlier systems placement attempts (Schenker *et al.*, 2003). The red circle illustrates the accuracy of the SCAIP system as all trials of the system lie within this circle. This represents a significant step forward in instrument placement technology which will form an essential part of any future autonomous scientific rover.

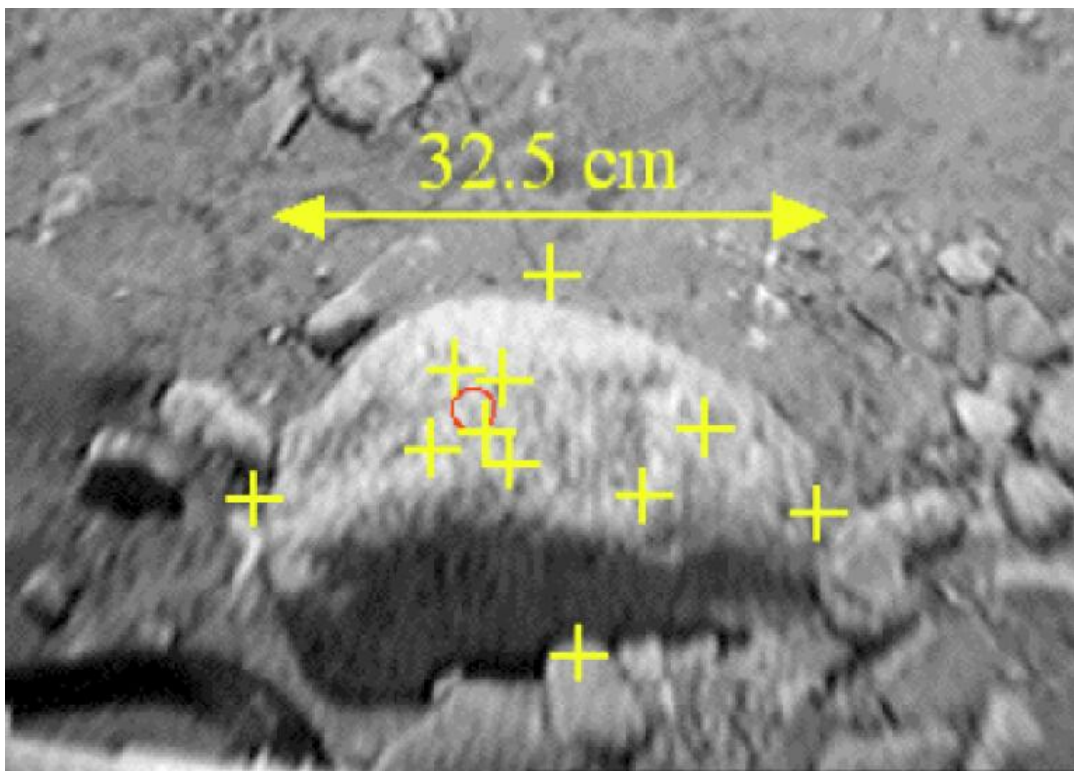


Figure 2.5: Instrument placement results from 11 trial runs of the prior algorithm with the distance being 32.5cm between the most-left yellow cross and the most-right yellow cross, with crosses at the positions where the instrument arm made contact overlaid on the short range image used for arm trajectory planning. Instrument arm contact positions for the SCAIP effort all lie within the 1cm radius red circle centred on the designated target. Image courtesy of NASA/JPL

2.3.1 Final Notes on SCAIP

The SCAIP project itself only goes part of the way towards producing a fully functional autonomous planetary scientist. The focus on the autonomous instrument placement has enabled it to produce a robust mission ready system. Unfortunately, as previously mentioned it is only part of a full system and still relies heavily on a human scientist selecting the target and producing an activity plan. The system also loses some of its efficiency if you are not able to see the exact sample point from the initial image of the sample site. The rover may have to be manually moved towards the site until the exact sample location is identified. This manual interaction, although not always necessary will reduce the efficiency of the system. In the case of rocks displaying lamination or bedding features such as those seen in Figure 2.6, the exact target location may not be obvious until the macro imaging stage has been reached.



Figure 2.6: Example rock target demonstrating lamination features.

2.4 On-board Autonomous Rover Science Investigation System (OASIS)

The On-board Autonomous Rover Science Investigation System (OASIS) is designed to operate on-board a rover identifying and reacting to serendipitous science opportunities. These science opportunities can include detection of dust devils, clouds, novel rocks (novel meaning, the kinds of rocks that the system has not seen before) and interesting rocks. The OASIS system analyses data that the rover gathers, and then prioritises the data based on established criteria. There are three main components within the OASIS system (Castano *et al.*, 2007b), these include:

- Feature extraction from gathered images: This concentrates on locating rocks based on shape, texture and albedo.
- Analyse and prioritise data: This uses the features extracted to determine scientific value of the planetary scene.
- Plan and schedule new command sequence: This dynamically modifies the rovers current plan to accommodate new observations.

The following subsections provide an overview of each of these components. The full architecture diagram of the OASIS system can be seen in Figure 2.7.

2.4.1 Feature Detection

The techniques presented in the OASIS literature are applicable to a wide range of data modalities. However, the initial OASIS focus has been on image analysis as images are much more commonly available and provide a large amount of information about the scene. The first step of an image evaluation for OASIS is to identify the features of interest within the scene. This can potentially be done before or after segmentation depending on what feature the system is trying to identify. Currently OASIS contains two segmentation algorithms and three feature extraction modules. Each of these modules applies general data analysis principles to identify and characterise image features that are representative of distinct scientific phenomena.

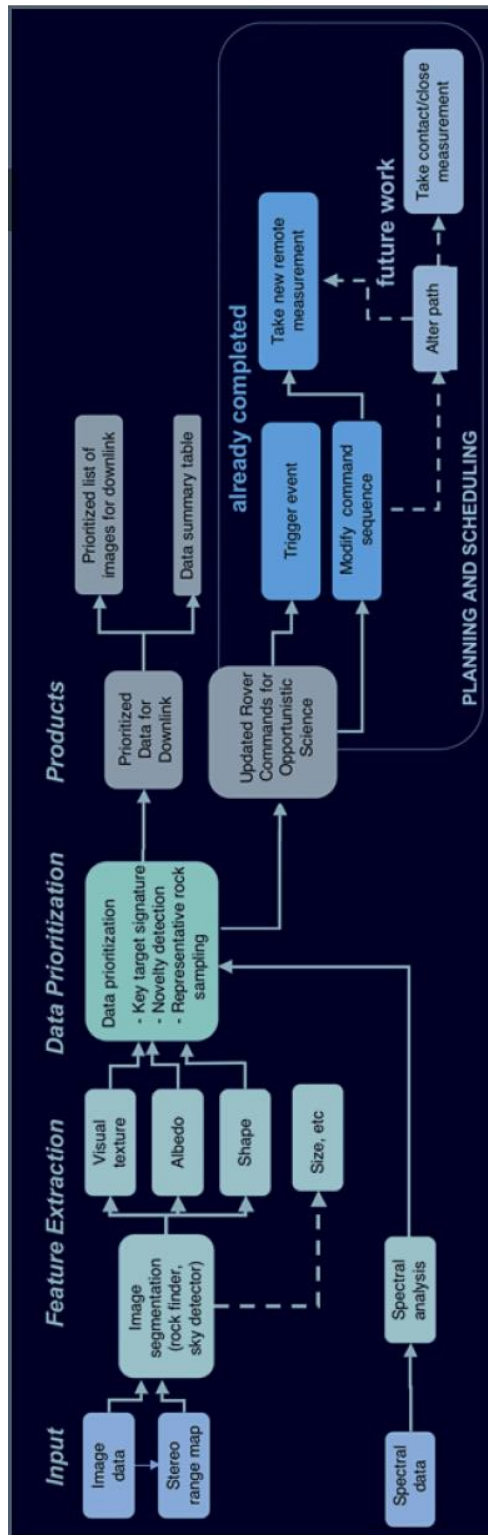


Figure 2.7: Full architecture of the OASIS system. Image courtesy of NASA/JPL

2.4.2 Image Segmentation

Sky detection Detection of the sky is an essential activity for any automatic scene processing, to be carried out by an autonomous system. It quickly identifies a proportion of the scene which could be deemed of little interest and one of primary interest. For example while searching for rocks it is unnecessary for items above the skyline to be processed. The approach used in OASIS is based on a region growing technique and is composed of four distinct steps (Castano *et al.*, 2007a):

- Find Seeds - This determines if the sky is present in the scene, with areas of low variance searched for and identified as seeds.
- Identify variance edge - This is identified by performing an edge detection on the variance image.
- Grow Seeds - The seeds identified in step one are then grown down to the variance edge identified in step two.
- Fill in region gaps - All enclosed gaps above the variance edge are filled in.

The algorithm is documented as demonstrating approximately 90% accuracy while tested on 301 MER images.

Rock detection The rock detection algorithm currently used on the OASIS system is based on the analysis of intensities on a single greyscale image (Castano *et al.*, 2007a; Castao *et al.*, 2004). The detection of rocks is carried out by finding closed shapes within the processed image. The image is initially normalised, filtered with an edge preserving smoother filter (bilateral filter, (Tomasi & Manduchi, 2004)). Its edges are then enhanced using an Unsharp Mask (USM) process. Sobel and Canny edge detectors are then both applied to the resulting image and all enclosed shapes are identified using an edge walker. The output of both detectors are then combined and a list of the contours of the identified shapes is produced. This algorithm is documented in (Castano *et al.*, 2007a), and has been tested on 65 MER Spirit PanCam images where 92% of the regions identified as “rocks” were in fact rocks.

2.4.2.1 Feature Extracion

Cloud detetor The cloud detector assumes that all large variations in intensity within the sky region are clouds (Castao *et al.*, 2006). The approach adopted to identify these features is to identify the sky region and then to look for areas of high variance. The work of (Castano *et al.*, 2007a) reports that the algorithm achieved a 93% accuracy in testing on 210 hand labelled images taken by the MER Opportunity.

Dust Devil detector A Dust Devil (Figure 2.8) is a strong well-formed whirlwind. They occur commonly on both the surface of Earth and Mars. OASIS attempts to detect dust devils by looking for motion within a temporal sequence. Dust devils are not the only thing that can move in a Martian scene as clouds will also move. However it is asserted in (Castao *et al.*, 2006) that, if interference noise can be accounted for within the sample images, it can be assumed that significant changes in an image sequence would be caused by a Dust Devil. The algorithm consists of a preprocessing step to reduce the level of noise in the image followed by image averaging. The difference between the averages of two adjacent images in a sequence are then computed. Noise effects are removed from the resulting image and a blob detection is performed to identify potential Dust Devils. The Dust Devil algorithm was tested on 385 images, divided into 25 sequences (acquired by the MER Spirit) ranging from 6 images to 20 images. The algorithm achieved an 85% accuracy rate when the average image was determined using a set of four continuous images (Castano *et al.*, 2007a).

Boundary detection An important task for a human field geologist is to develop an understanding of the field area. Generally, this involves going into the field area, identifying rock types present, key landforms and landscapes, mapping geological contacts or boundaries, developing a geologic map, and creating a model based on historical interpretations and the dynamic processes that have shaped the landscape. Rocks exposed at the surface provide a record of the surface history. Their physical appearance and location testify to the environmental setting in which they were formed. To gain an understanding of the basic geologic history of a region, it is necessary to identify where the rocks on the surface originated. In order to do this, the geological contacts/boundaries in the field must be identified and mapped. The identification and mapping of geological boundaries ranges from simplistic boundary detection (e.g., hills, plains, and river channels), to complex identification of different rock and cast types, to erosional and depositional



Figure 2.8: Dust Devil as observed by MER Spirit rover (Image courtesy of NASA/JPL)

histories of the landscape. For a rover, it is the critical hardware interface in conjunction with the scientist on Earth that collects the data. For future long-range rovers on a planetary surface, it is critical for the rover's on-board software to be capable of identifying simple boundary transitions during long traverses (Castano *et al.*, 2007a).

Rock properties The identification of geological features such as rock properties has been the primary focus of the OASIS feature extraction routines. OASIS currently estimates albedo, texture, size and shape. The albedo of a rock is used as an indicator of the reflectance of the rock which in turn gives an indication of the composition of the rock. This value is approximated by averaging the greyscale values of the pixels that are identified as part of the rock. OASIS uses Gabor filters to estimate the visual texture of identified rock targets (Castao *et al.*, 1999). Identified textures are used to gather information about the target's history and composition. Shape is also gathered and used to provide information about the targets provenance (source of target) and about the environmental conditions that the target has been exposed to. In order to calculate a target's shape the OASIS system fits an ellipse to the outline of the target. The eccentricity of that ellipse along with the error is computed. The angularity of each rock is also assessed using a measure of ruggedness.

Analysis and prioritisation After assessing all identified targets the information gathered is used to affect either the downlink data queue or the rover activity schedule. OASIS utilises four methods to facilitate analysis and prioritisation. The first method known as “detected events”, is used in conjunction with the environment detectors, clouds and Dust Devils. The remaining three: “target signature”, “novelty detection” and “representative sampling”, are used to react to rock target discovery. There are briefly introduced below.

Detected event Simply, when an event is detected a flag is set to identify that something of interest is present and has been identified. This flag can be applied to an image or a sequence, as in the case of a Dust Devil.

Target signature This technique recognises key signatures that have been pre-identified by planetary geologists as interesting. This can be done by stipulating the value of feature combinations (Castano *et al.*, 2007a) or by identifying a rock with interesting properties from the rocks already observed. The system then prioritises rocks as a function of the distance of their extracted feature vector from the specified weighted feature vector.

Novelty detection This technique assesses new targets and produces a novelty value based on the previously observed targets. Different techniques are developed to implement this, including: distance-based, probability-based and discriminative (Castao *et al.*, 2008).

Representative sampling This technique prioritises data for down-link to ensure that representative rocks of the traversed region are returned. This is in order to satisfy one of the main objectives for rover traverse science, gaining an understanding of the region being traversed.

2.4.2.2 Planning and execution

When a science target is identified by OASIS, a science event is raised. This causes a new science event to be passed to the scheduling module which decides if the event can be accommodated. If it can, the science plan is modified and new data is gathered. The scheduler and planner are major components of OASIS and primarily focus on the discovery of unexpected or opportunistic science. This means that dynamic re-planning and scheduling can take place on-board the rover and the rover’s command sequence can be altered. An in-depth explanation can be found in (Castao *et al.*, 2006).

2.4.3 Final Notes on OASIS

OASIS provides an excellent example of a fully integrated autonomous robotic planetary exploration rover. The subject of the research here is to explore the feasibility of an on board autonomous planetary scientist. There are some subtle differences between endowing a system with the ability to make decisions based on geological cues or evidences detected in the assessed scene, and enabling a system to examine how close preserved targets are to what a human geologist would assert as interesting. The “target signature” method of analysis and prioritisation does the latter. A human planetary geologist can specify that targets are prioritised based on specific feature values: e.g., the scientist may choose to prioritise targets based upon two aspects of the target’s shape, such as eccentricity and ellipse fit. Or the scientist can identify a target signature that is “interesting” and prioritise targets based upon their similarity to this signature. However, in order to emulate a planetary geologist an autonomous system would need to access the science value of the specified target itself in some way and identify the scientific triggers which stipulate its value.

There are other obstacles not addressed by the OASIS project. Colour is not used to identify potential targets as the system uses only greyscale images. Colour could potentially be a great indicator of science value and could also add some additional information regarding the target’s chemistry. The type of target that is being searched for in OASIS also presents a limitation. Here OASIS has adhered to the classic approach of target selection, that is, to look for “rocks”. A recent report produced by a planetary geologist has indicated that bedrocks and exposed rock shelves should carry a much higher science priority than loose rock fields. This is primarily due to the fact that the structure of these potential target sites can provide valuable information about the geological processes that have been at work in the area over extended periods of time (Pullan, 2006). OASIS does not appear to cater for this type of science target.

2.5 Summary

During this chapter the current state of the art in autonomous science and autonomous sample selection and acquisition has been presented for four autonomous science systems. RAMS is an autonomous exploration vehicle for the autonomous

discovery of a meteorite. A Bayes network approach has been adopted for rock classification and a Markov chain segmentation approach to segment the captured images. The system can classify rocks into different target types that have been pre-defined by the user. The CREST Robotic Scientist project has demonstrated an end to end implementation of an autonomous opportunistic platform. It has proved the concept of the Science Assessment framework and the concept of a geology based image assessment of potential science targets. The SCAIP project goes part of the way to produce a fully functional autonomous planetary scientist. The focus on the autonomous instrument placement has enabled it to produce a robust mission system. However it is only part of a full system and still relies heavily on a human scientist selecting the target and producing an activity plan. OASIS provides an excellent example of a fully integrated autonomous robotic planetary exploration rover. The subject of such research is to explore the feasibility of an on board autonomous planetary scientist. These reviews provide background information for the subsequent development to be reported in this thesis.

Chapter 3

Target Detection and SIFT-Based Matching Desired Keypoints

Planetary scientists and geologists will benefit from approaches for automated segmentation and measurement of rocks in natural environment. Since rocks show different morphologies can be difficult to be distinguished from the background soil, they are poorly fitted for current visual segmentation techniques. In this chapter, an automated detection and segmentation method is proposed to address this challenge. Additionally, a novel approach is introduced to measure the size of a detected rock.

3.1 Background

In terms of rock segmentation research in intensity images of a planetary surface, several supervised and unsupervised approaches have been developed and produced to identify rocks. For supervised techniques, existing methods typically employ a belief network based on machine learning to classify homogeneous regions from colour images (Thompson *et al.*, 2005). However, a rock may have different intensity and colour due to the illumination and geometry of the rock surface. Dunlop (Dunlop *et al.*, 2007) proposed an approach applying a normalized-cut strategy to fragment an original image into superpixels and then to merge them into rock regions with support vector machine (SVM) classifiers. In this method training set determination influences the quality of the resulting detections for large rocks and also the misclassification rate of structured soil. Shang and Barnes

(Shang & Barnes, 2011; Shang & Barnes, 2013) have constructed image classifiers combining fuzzy-rough feature selection (FRFS) (Jensen & Shen, 2008) (Jensen & Shen, 2009) and SVMs (Mitchell, 1997) to increase classification efficacy. As colour images are at the present manually produced by scientists on Earth, this method is impossible to be practically used on-board rover.

With regard to unsupervised techniques, Gor (Gor *et al.*, 2001) implemented a rock detection approach where large rocks are identified using range data through ground-plane fitting and height information, whilst edge-flow segmentation along with image intensity information is employed for small rocks. In this method, a key control parameter is image scale and the range data is generated from stereo imagery. Castano (Castano *et al.*, 2007a; Castano *et al.*, 2004) proposed a method to detect the closed contours of rocks by combining an edge-based rock detector with multi-scale image pyramid. However, this algorithm is efficient only when there are obvious intensity differences between rocks and soil. Other unsupervised techniques include: a method using the texture-based rock segmentation and the edgeflow-based boundary refinement is proposed by Song (Song, 2008); a k -Means-based method for rock clustering (Fink *et al.*, 2008); and a similar region-growing method for rock identification in the context of segmentation (Pugh *et al.*, 2010). Thompson (Thompson & Castano, 2007) conducted a comparison for the performance of a number of existing rock detection algorithms.

In this chapter, an unsupervised method is proposed to address a segmentation problem to extract rocks from an image. This method appears to be more competent for the complex Mars environment, with little rover-Earth communication required than the supervised approaches. In the Martian exploration all supervised systems require interaction with Earth-based scientists for either training or parameter setting. Unfortunately, sufficient downlink is not available to allow interactions between scientists on Earth and rover on Mars for science data analysis. Unsupervised techniques however, help the development of full autonomous systems.

3.2 Target Identification

3.2.1 Overview of the Proposed System

In order to achieve autonomy (i.e. minimizing human intervention), unsupervised techniques are taken as the start point (Gor *et al.*, 2001). The general issue that is addressed by the present work is the identification of scientifically interesting rocks (such as sedimentary, metamorphic and igneous ones) that are able to provide scientists knowledge relating to the history of the geology and environment conditions on Mars. The proposed system deal with this challenge, having the ability to detect scientific targets in Mars images and to generate a closed contour of an identified rock. In Figure 3.1 *Rock Detection* is a key stage and implements the extraction of interesting features from the images taken over a given terrain. Here, the segmentation performance of typical automatic global thresholding methods were evaluated for Mars images, including Co-occurrence matrix, Histogram concavity, Minimum error, OTSU and Moment-preserving methods (?). However, OTSU leads to the best result. So, a tri-level thresholding OTSU method (Otsu, 1979) has been employed to address the issue of background segmentation. Several edge detector approaches were evaluated for Mars images, including Canny, Sobel, Prewitt, Robert, LoG, Basic Declivity and Modified Declivity edge detectors (?). The method of Canny achieved the best qualitative results. Hence, edges from the Canny method (Canny, 1986) have been utilized to merge the regions from the tri-level thresholding OTSU into closed contours which identify the rock boundaries.

3.2.2 Rock Detection

Rock detection is in this work, an important stage in the process of rock sample acquirement, which utilises a tri-level thresholding OTSU method to segment foreground (rock) from its background. The Canny algorithm is then employed not only to investigate the entire edges in an image but also to form the spatial dependency of regions which are returned by the tri-level thresholding OTSU. Finally, a Template Dilatation Edge Linking (TDEL) method is adopted to detect the closed contour of each rock within an image. These techniques are detailed below.

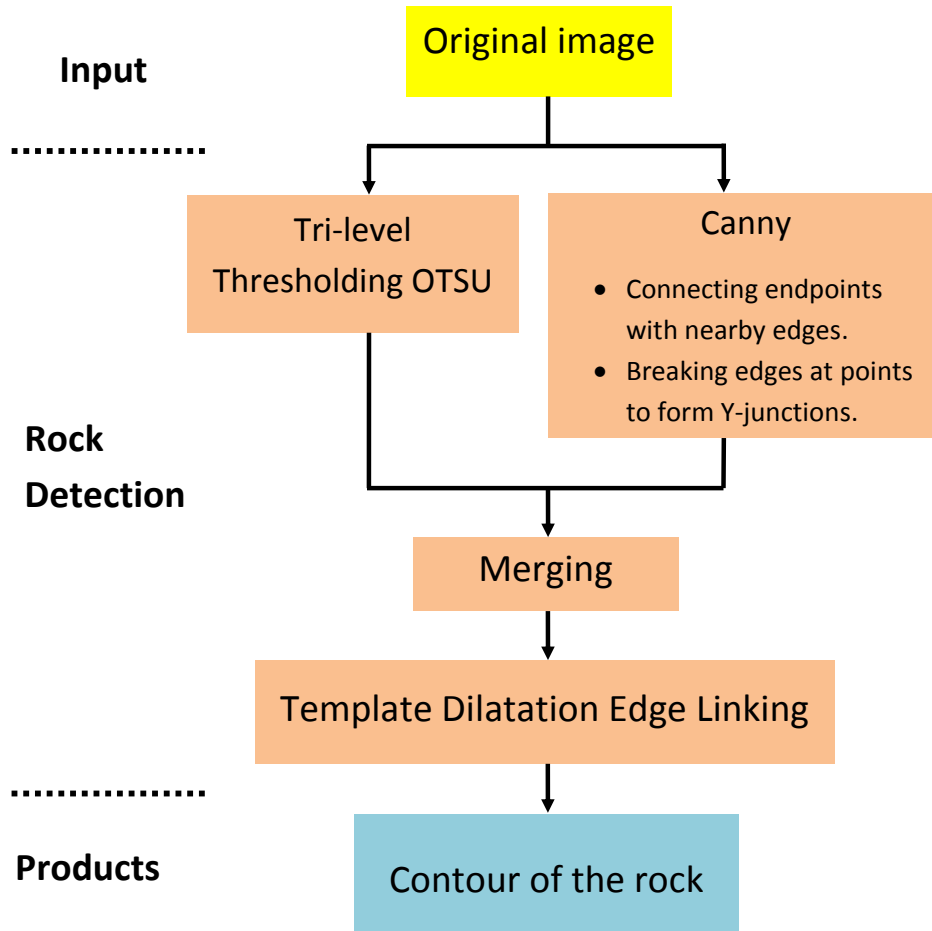


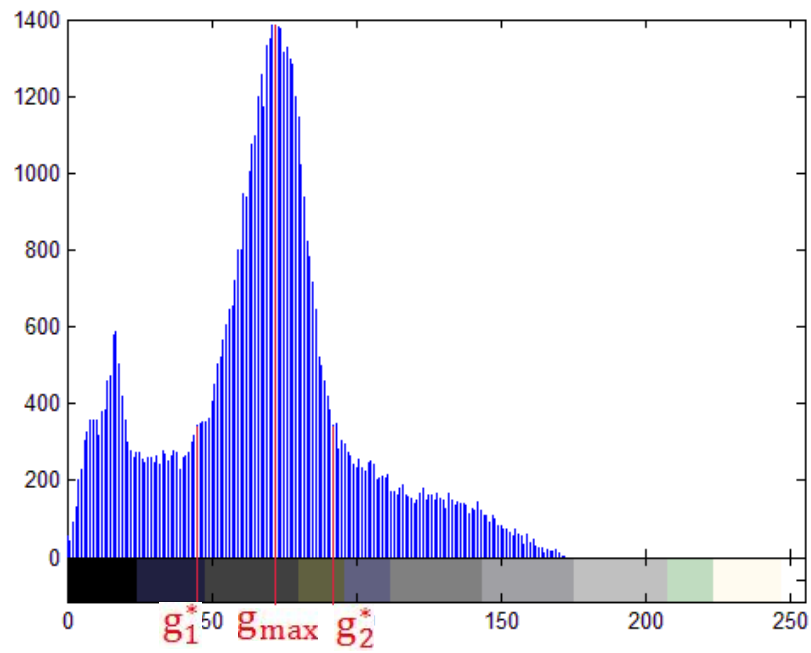
Figure 3.1: An overview of the proposed system.

3.2.2.1 Tri-level Thresholding OTSU

On the basis of the observations and surveys obtained from the MER panoramic and navigation camera images, it is found that in most cases the number of background pixels is more than the foreground pixels in a given image. For simplicity, in this research the shadow of a rock is considered as part of the rock identified. Accordingly, the popular OTSU's approach is not able to perform its usual a task. The reason is that conventional OTSU is a bi-level thresholding algorithm which just partitions the image into two regions; in other words, only one threshold is derived. In order to meet the need for rock identification in Mars images, an improved OTSU method is required to break down a given image into three regions, thereby having to obtain two thresholds to be obtained (see Figure 3.2). Details of the enhanced algorithm are as follows.



(a)



(b)

Figure 3.2: An image example and histogram from MER Navcam data showing the optimal thresholds g_1^* and g_2^* ($[0, g_1^*]$:shadow; $[g_1^*, g_2^*]$:rock; $[g_2^*, 255]$:ground)

OTSU's thresholding technique (Otsu, 1979; Liao *et al.*, 2001) is based on a discriminant analysis which partitions a given image into two classes of grey levels. An image can be seen as a 2D greyscale intensity function, which includes N pixels with grey levels in the range of 0 to G , where G is typically 255 if 8-bit quantization is assumed. Let the number of pixels with grey level i be indicated by f_i , and the probability of the occurrence of grey level i in an image be defined by:

$$p_i = f_i/N \quad (3.1)$$

Also, let g_{max} denote a grey level value corresponding to the maximum probability of p_i in Eq.(1). Hence, the grey level of an image can be partitioned into two regions R_0 and R_1 at the boundary defined by the grey level g_{max} such that $R_0 = \{0, 1, 2, \dots, g_{max} - 1\}$ and $R_1 = \{g_{max}, g_{max} + 1, g_{max} + 2, \dots, G\}$. Subsequently, OTSU applies a method that maximizing between-class variance to derive an optimal grey level threshold for the two regions R_0 and R_1 , respectively. Here, the algorithm details are just shown regarding the region R_0 , because it is similar for the region R_1 .

In the region R_0 , the pixels are divided into two classes, C_1 with grey levels $[0, 1, \dots, t]$ and C_2 with grey levels $[t + 1, t + 2, \dots, g_{max}]$. Therefore, the grey level probability distributions for the two classes are as follows:

$$\begin{cases} C_1 : p_0/\omega_1(t), \dots, p_t/\omega_1(t) \\ C_2 : p_{t+1}/\omega_2(t), p_{t+2}/\omega_2(t), \dots, p_{g_{max}}/\omega_2(t) \end{cases} \quad (3.2)$$

where $\omega_1(t) = \sum_{i=0}^t p_i$ and $\omega_2(t) = \sum_{i=t+1}^{g_{max}} p_i$. Also, the means for classes C_1 and C_2 are

$$\mu_1 = \sum_{i=0}^t i * p_i/\omega_1(t) \quad (3.3)$$

and

$$\mu_2 = \sum_{i=t+1}^{g_{max}} i * p_i/\omega_2(t). \quad (3.4)$$

Let μ_T be the mean luminance value for the entire image. It is easy to show that

$$\omega_1\mu_1 + \omega_2\mu_2 = \mu_T \quad (3.5)$$

$$\omega_1 + \omega_2 = 1 \quad (3.6)$$

Using discriminant analysis, OTSU defined the between-class variance of the threshold image is defined in OTSU by

$$\sigma_B^2 = \omega_1(\mu_1 - \mu_T)^2 + \omega_2(\mu_2 - \mu_T)^2. \quad (3.7)$$

For bi-level thresholding, the optimal threshold g_1^* is selected so that the between-class variance σ_B^2 is maximized; that is,

$$g_1^* = \text{ArgMax} \{ \sigma_B^2(t) \} . (0 \leq t \leq g_{max}) \quad (3.8)$$

Likewise, the optimal threshold g_2^* can be obtained in the region R_1 (Figure 3.2).

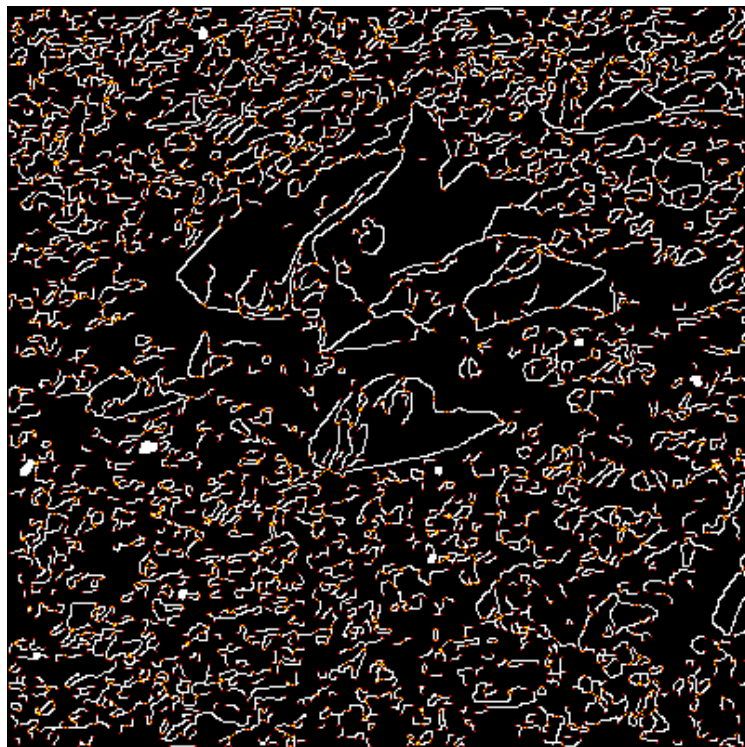
3.2.2.2 Merge of Regions

Through the use of the above work, a lot of the regions found may be regarded as parts of the rocks in an image as shown in Figure 3.3(a). It is obvious that certain regions may belong to the same rock, however, here they are segmented into the different rocks, and this resulting in a serious over-segmentation situation. In order to address this problem, spatial details are taken into account for establishing the relation of those regions which are adjacent. Canny's edge detector is one of the popular ways in which edge detection is employed for spatial details. Post-processing of the edges is required with the Canny algorithm. There are two popular edge cleaning operations that can be used for the edge post-processing which are described as below:

- Connecting endpoints. Because the vast majority of the edges detected using Canny are not able to generate a closed contour relating to the object of interest, those endpoints off one pixel are connected with a straight line. In Figure 3.3(b) the white curves are the edges detected, and the red points are the endpoints of the edges, and the yellow points are the connect lines.



(a)



(b)

Figure 3.3: (a) Resultant image of proposed method from Tri-level Thresholding OTSU. (b) Resultant image from connecting endpoints.

- Breaking edges. Because a good contour of the interest object is required without branched edges, those edges with points that form a Y-junction are broken. See Figure 3.4, where four types of Y-junction are shown, each individual is comprised of a 3×3 window in which the white pixels form a ‘Y’ shape.

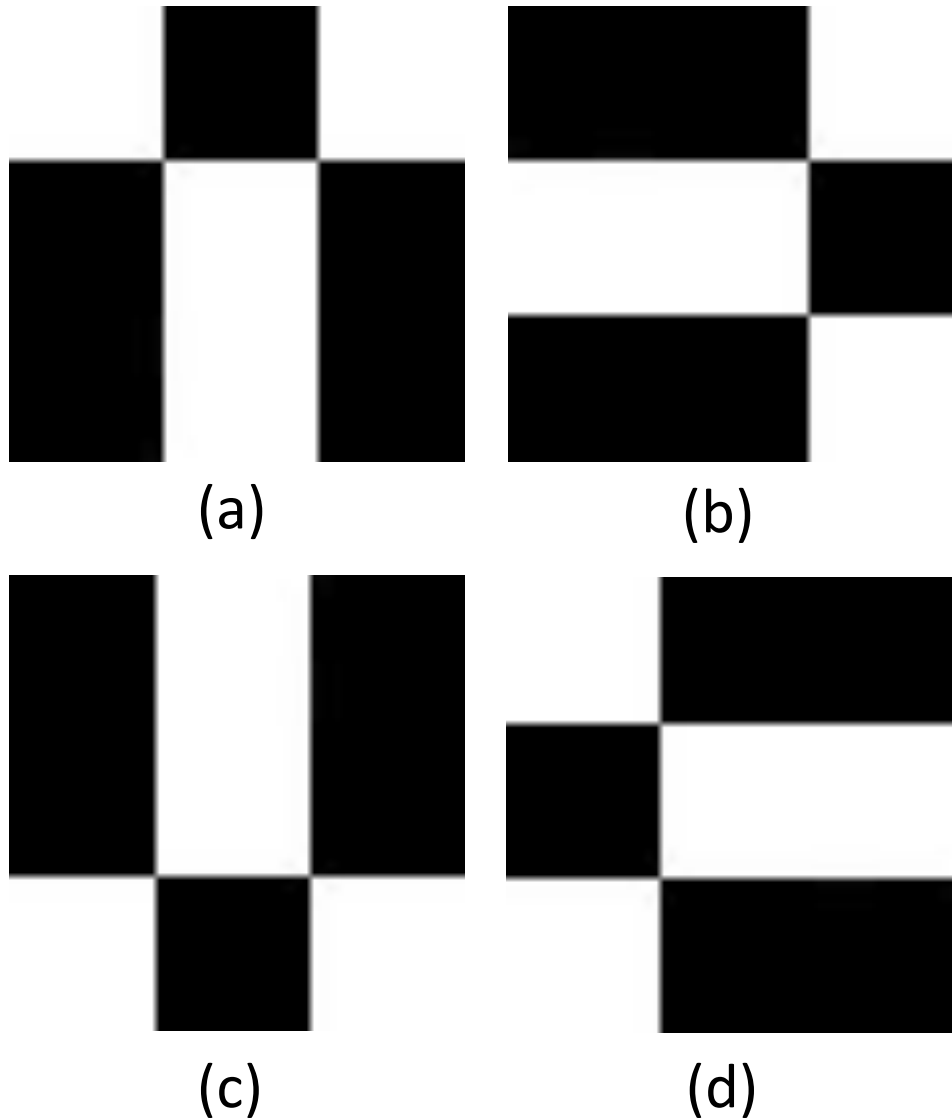


Figure 3.4: Four types of Y-junction.

Regions merging aims to combine regions which are potential portions of the same rock. Here, the merging operation is associated with the following set operation is defined as:

$$L_i = R_i \cap E_j; \quad \{1 \leq i \leq n; 1 \leq j \leq m\} \quad (3.9)$$

$$O_k = \begin{cases} L_i \cap L_j, & \text{if } L_i \cap L_j \neq \Phi \quad (i \neq j) \\ L_i, & \text{otherwise} \quad \{1 \leq i, j \leq n; 1 \leq k \leq l\} \end{cases} \quad (3.10)$$

where $R_i \ni \{R_1, R_2 \dots, R_n\}$, which denotes a set of regions from the results of the Tri-level Thresholding OTSU method. $E_i \ni \{E_1, E_2 \dots, E_m\}$, which represents a set of edges from the results of the post-processing of the edges. L_i expresses the intersection between regions (R_i) and edges (E_i). The number of L_i is equal to the number of R_i . The ultimate result of the regions merging is O_k , which means that the distinct regions (R_i) have been combined with a single edge. Note that if edges do not involve shared regions, the merging operation does nothing. Figure 3.5(a) shows the results of the intersection with respect to regions and edges. The merging results are given in Figure 3.5(b).

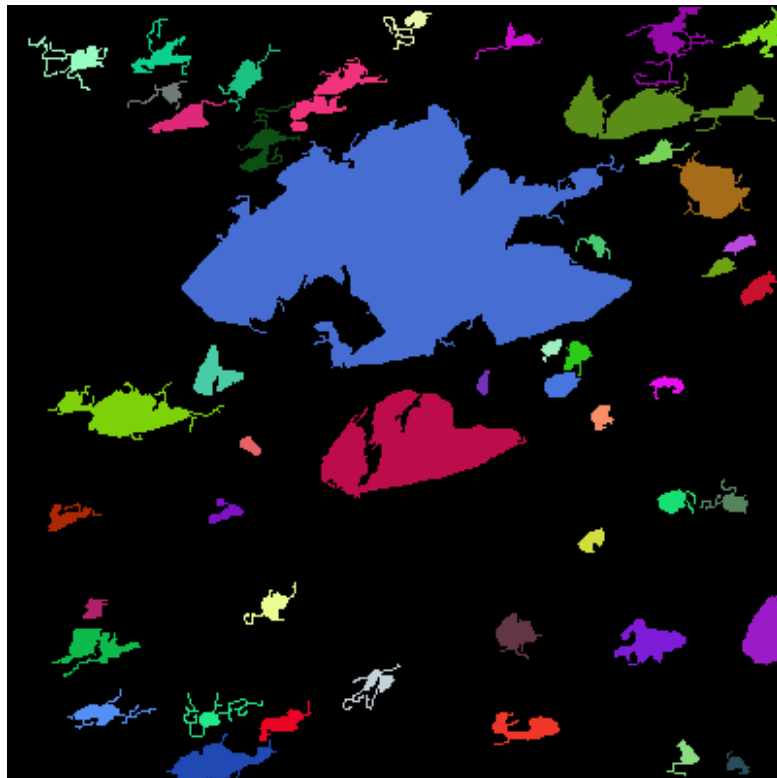
3.2.2.3 Template Dilatation Edge Linking (TDEL)

In the preceding section, the algorithm for merging regions and edges has been described. However, as shown in Figure 3.5(b), certain targets do not have a closed contour along their border, and the majority of detected rocks include burred edges. To address this problem the Template Dilatation Edge Linking method (TDEL) (Gui *et al.*, 2012a; Gui *et al.*, 2012b), is applied to construct the closed contour for each rock in the image. The algorithm of TDEL is described as follows:

1. Build the irregular bounding box of the desired rough rock boundary. This is achieved by down-sampling twice the merged image (Figure 3.5(a)), then the result of the procedure is achieved by up-sampling twice. As a result, an irregular bounding box encompassing the corresponding desired rock is generated for each individual rock (Figure 3.6).
2. Choose an random pixel as the start point on the irregular bounding box.
3. Generate a $m \times m$ template based on the start pixel ($m = 3$ initially) (Figure 3.7(a)).
4. Judgement: Are there other colour pixels in the template? If Yes then do: (a) if these pixels are of the same colour, sequentially connect them



(a)



(b)

Figure 3.5: Intersection (a) and merging (b) of Regions and Edges.

- using a straight line and go to (5); (b) if there are different colours in these pixels, connect the nearest two pixels of the different colour using a straight line and go to (6); else, repeat. until all pixels are visited.
5. Dilate the current template ($m = m + 2$), then to (4) (Figure 3.7(b)).
 6. Select the next neighbor pixel point relative to the current pixel point on the irregular bounding box.
 7. If the pixel point is the end of all sequential traversal pixels on the irregular bounding box, then the algorithm ends; else, then go to (3).

Finally, the morphological methods of image processing erosion and dilation are applied to remove the ‘burrs’ on the closed contour of the identified rock.

3.3 Matching Keypoints

In Mars exploration missions the size of rocks restricts instrument deployment and sampling. Hence, one of the most important steps is to match keypoints for calculating the size of a rock in this research. Here, keypoints are defined as the following: top-most, bottom-most, left-most, right-most and centroid points on the bounding box of a rock in an image. The work of matching desired keypoints involves three key stages: (a) To match the feature points on the body of the rocks in a pair of images based upon the SIFT-RANSAC algorithm (see later). (b) To employ a simple method combining Euclidean distance with the rotation angle of the image to obtain rough matching points. (c) To apply a correlation method to compute accurate matching points.

3.3.1 SIFT-RANSAC Algorithm

Considering characteristic of Mars missions, although SIFT is low, it is more stable than SURF in most situations (Juan & Gwun, 2009). SIFT (Lowe, 1999; Lowe, 2001; Lowe, 2004) stands for Scale Invariant Feature Transform, which is a feature point detection and matching algorithm initially proposed by Lowe in 1999, and finally summarized in 2004. SIFT features are not only invariant to image scaling, translation, and rotation, but also partially invariant to illumination changes and affine. It has been used in many fields, such as object recognition, image mosaic, mobile robot localization and map building.

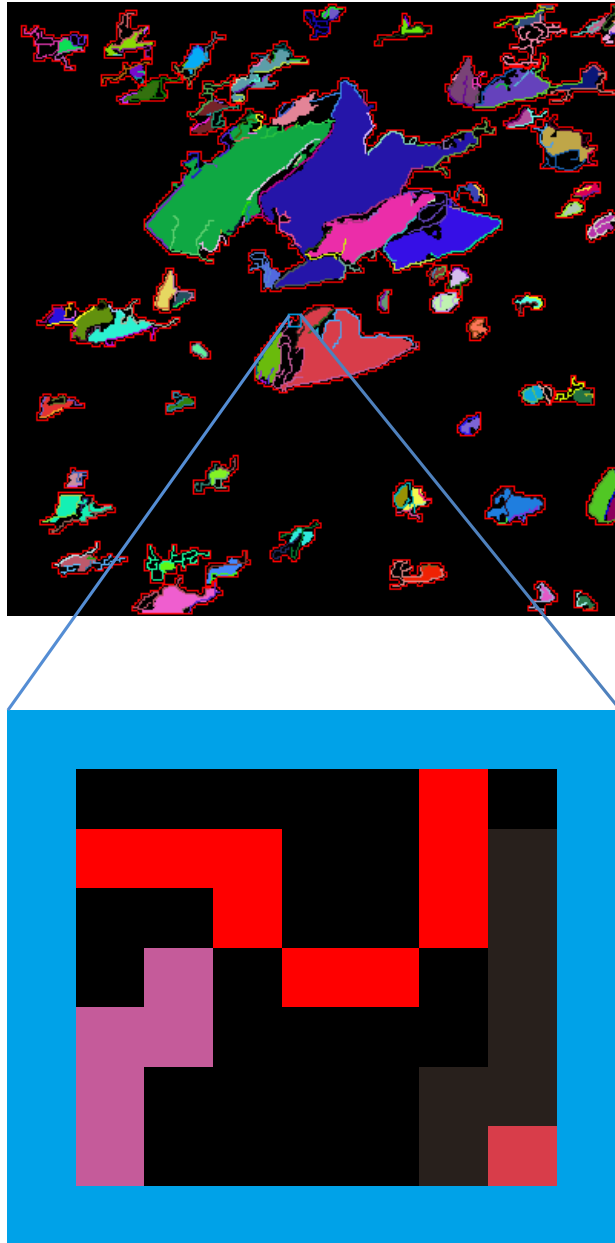
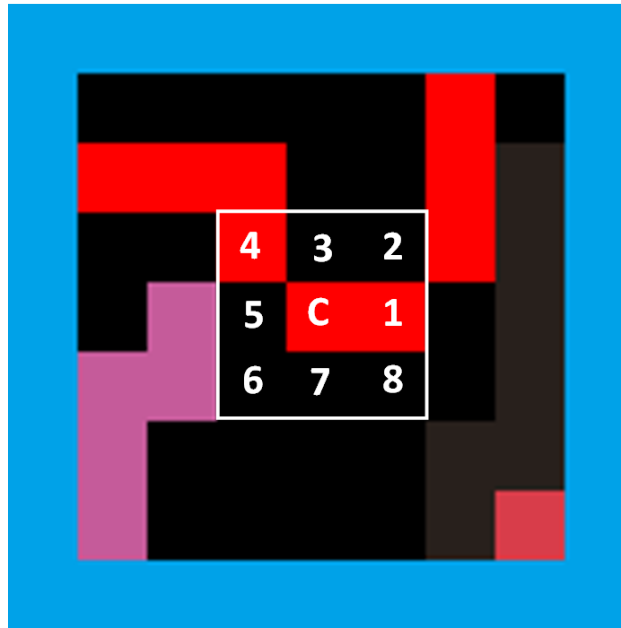


Figure 3.6: Top: The rocks included in the irregular bounding box. [Red line denotes the irregular bounding box]. Bottom: Patch of the image for subsequently explaining the TDEL algorithm. In the patch red pixels form a rough rock boundary, the other colour pixels from the real rock boundary that can be connected.

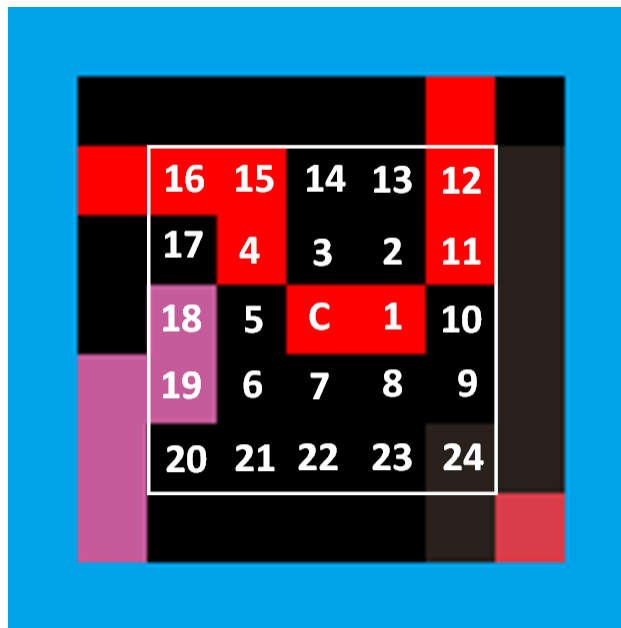
The extraction of SIFT feature points mainly includes four subroutines shown below:

1. Scale-space extreme detection

SIFT algorithm selects scale space extreme points as candidate feature



(a)



(b)

Figure 3.7: (a) 3×3 template. 'C' pixel is the center of the template on an irregular bounding box. Here no pixel has a different colour except for the red and black, so there is no connection performed. (b) 5×5 template. The template is a dilatation of the above 3×3 template. Here '18', '19' and '24' pixels are in different colours in addition to red and black, and the colour of '18' and '19' is different from the colour of '24'. Therefore, the distances between '18' and '24', '19' and '24' are calculated separately. The nearest distance is from '19' to '24' in the two results, so these two pixels are connected using a straight line.

points. The scale space is of an image $I(x, y)$ defined by:

$$L(x, y, \sigma) = G(x, y, \sigma) * I(x, y) \quad (3.11)$$

Detect the extreme in the result of the DoG (Difference of Gaussian) between the following image convolutions:

$$D(x, y, \sigma) = L(x, y, k\sigma) - L(x, y, \sigma) \quad (3.12)$$

In the above, the symbol $*$ represents two-dimensional convolution; $G(x, y, \sigma)$ represents a Gaussian function; and σ represents the standard deviation of normal Gaussian distribution; k represents a constant multiplicative factor.

2. Key point localization

Construct the Taylor expansion in the scale space constructed by the DoG function:

$$D(X) = D + \frac{\partial D^T}{\partial X} X + \frac{1}{2} X^T \frac{\partial^2 D}{\partial X^2} X \quad (3.13)$$

Then solve the formulae:

$$\hat{X} = -\frac{\partial D^T}{\partial X} \left(\frac{\partial^2 D}{\partial X^2} X \right)^{-1} \quad (3.14)$$

$$D(\hat{X}) = D + \frac{1}{2} \frac{\partial D^T}{\partial X} X \quad (3.15)$$

3. Orientation assignment

Assign a main direction for each feature point, containing gradient magnitude $m(x, y)$ and gradient direction $\theta(x, y)$:

$$m(x, y) = [(L(x, y + 1) - L(x, y - 1))^2 + (L(x + 1, y) - L(x - 1, y))^2]^{\frac{1}{2}} \quad (3.16)$$

$$\theta(x, y) = \arctan \frac{L(x, y + 1) - L(x, y - 1)}{L(x + 1, y) - L(x - 1, y)} \quad (3.17)$$

4. Keypoint descriptor

Divide the image region around each critical point to blocks, calculate the gradient histogram in each block, and generate a unique 128-dimensional vector.

In order to match a pair of images, whose SIFT feature vectors are separately generated using the above algorithm. Euclidean distance between the corresponding keypoint feature vectors is employed. It measures the similarity relative to the keypoints in a given pair of images. A certain keypoint is picked in one of the two images, then keypoints are found out with the closest and second-closest Euclidean distance in relation this keypoint in the other image. Compare the distance of the closest to that of the second-closest for matching the keypoints. When the distance is less than a predefined threshold, it can be considered to be the correct matching. The matching effect is shown in Figure 3.8.

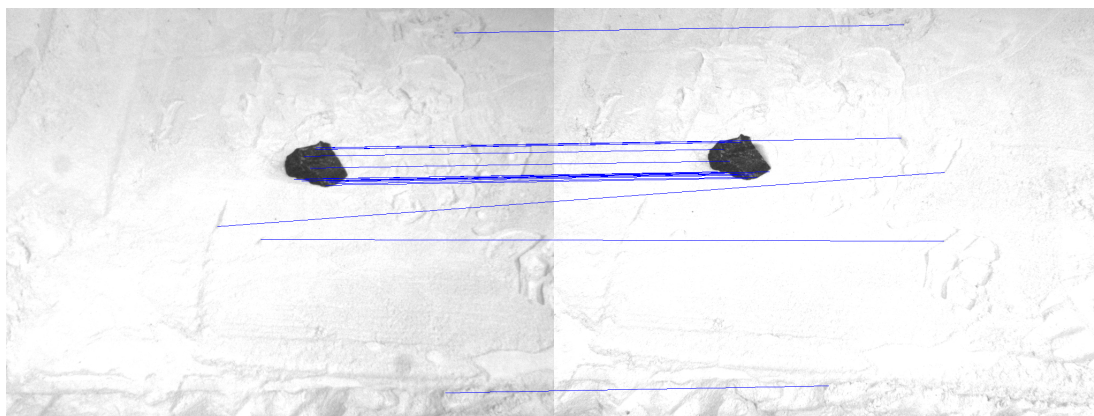


Figure 3.8: SIFT based matching result.

Note that in applying this method, when reducing the threshold, the number of matching points will decrease, but with fewer mismatches. When raising the threshold, the number of matching points will increase, but there will be more mismatches returned. In general, the more feature points matched correctly the better. To obtain a reasonable trade off between the number of matching points and that of mismatches, a robust estimation method needs to be developed. One of the useful techniques is the RANSAC algorithm (Mikolajczyk & Schmid, 2002) that can help remove mismatches.

RANSAC (Fischler & Bolles, 1981) stands for Random Sample Consensus which is an iterative robust method to estimate parameters of a mathematical model from a set of observed data which contains outliers. The RANSAC algorithm divides the data into inliers that fit to the estimate model and outliers that do not. It works mainly based on the random voting principle (Feller, 1971), tolerating the condition that the data space contains more than half of the outliers and being capable of effectively dealing with multiple structure data. Figure 3.9 shows an

application example of RANSAC, to the matching result of Figure 3.8.

There are the following assumptions:

Let ω denotes probability of a feature point selected as the correct feature point. Then, the following conditions hold:

If it is needed to select n points to estimate the model, the probability of the n points in the inlier is ω^n . Then the probability of at least one point in the outlier is $1 - \omega^n$. This shows that a bad model is estimated.

If the model is run for k times, the probability of the n points never occurring in the inlier is $(1 - \omega^n)^k$.

Let P stand for the probability of estimating a wrong model, then

$$P = (1 - \omega^n)^k \quad (3.18)$$

$$k = \frac{\ln P}{\ln(1 - \omega^n)} \quad (3.19)$$

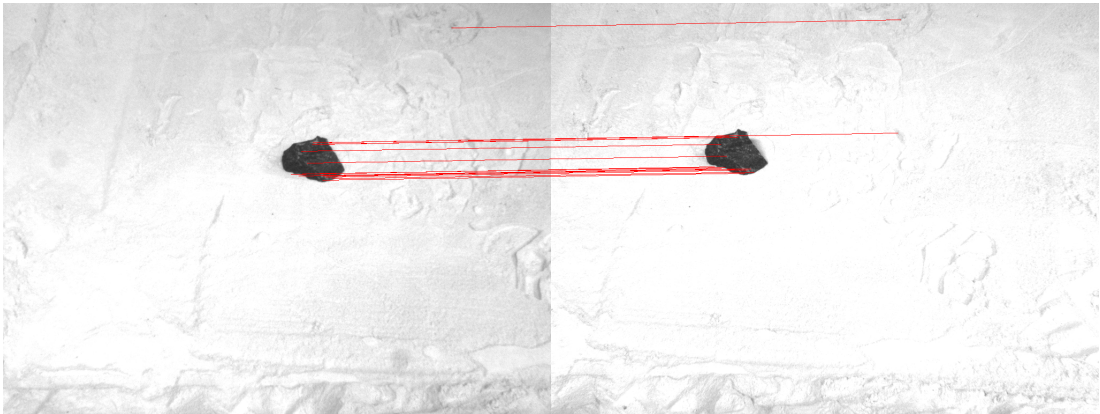


Figure 3.9: RANSAC result relative to Figure 3.8.

3.3.2 Fundamental Matrix

The notion of fundamental matrix in computer vision (Faugeras, 1992) is not only developed to capture the information about the translation and rotation that relate the cameras in a certain physical space, but also that about the intrinsics of both cameras. As such, it relates the two cameras in pixel coordinates. A fundamental matrix F is a 3×3 matrix which relates the points on the image plane of one camera

to the points on the image plane of the other camera. Therefore, collectively all pairs of the corresponding points in a stereo image pair can be expressed as follows:

$$q_r^T F q_l = 0 \quad (3.20)$$

In this expression, q_r is a pixel point in one image, say the right image, and q_l is a corresponding pixel point relative to q_r in the other, or the left image.

Based upon the above expression, the matrix F can be computed if a number of known correspondences are provided which may be obtained from the SIFT-RANSAC algorithm. In this algorithm, the RANSAC method is applied iteratively using a random subset of known correspondences. The fundamental matrix F is taken to be the solution closest to the average or the median solution over the iterations.

3.3.3 Epipolar Geometry

The basic geometry of a stereo imaging system is referred to as epipolar geometry. Epipolar geometry combines two pinhole models (one for each camera) and certain interesting new points called the epipoles (see Figure 3.10). The lines $X_L e_L$ and $X_R e_R$ (from the points of projection to the corresponding epipolar points) in Figure 3.10 are called the epipolar lines. The epipolar line is important for matching keypoints in this research. For example, if X_L is a matching keypoint, X_R is the matched keypoint of X_L on the epipolar line.

Once the fundamental matrix F is obtained, for any given point in one image, there is a different corresponding epipolar line which can be computed in the other image by equation (3.20). Each computed line is encoded in the form of a vector of three parameters (a, b, c) such that the epipolar line is defined by the following equation:

$$ax + by + c = 0 \quad (3.21)$$

3.3.4 Rough Matching Points

For the present work, the ExoMars PanCam Emulator developed at Aberystwyth University (Pugh *et al.*, 2012) is equipped with two wide angle multi-spectral

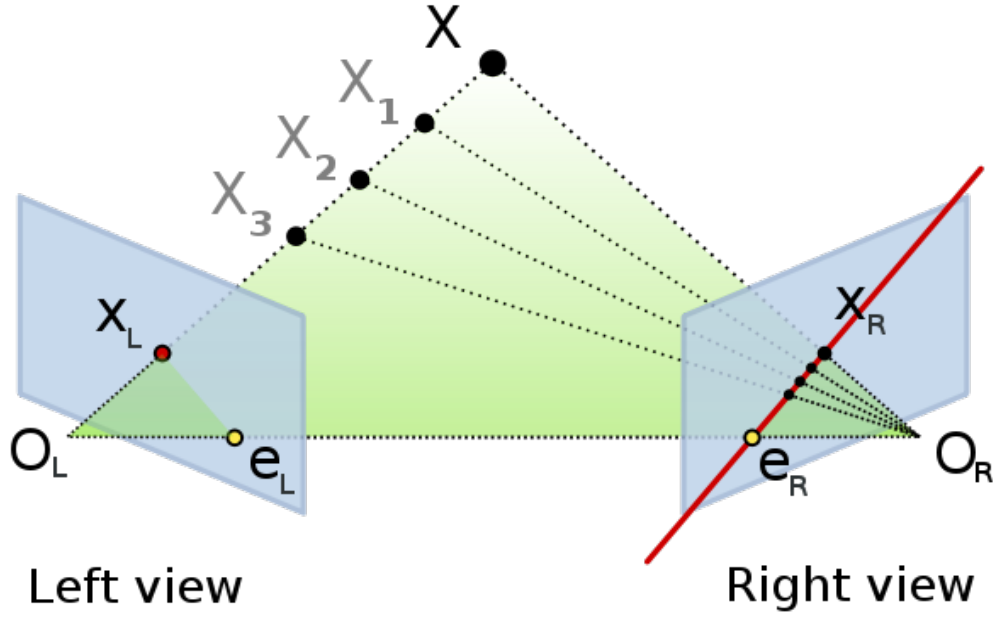


Figure 3.10: Epipolar geometry. Two cameras are used to observe a point X , with their respective centers of projection being O_L and O_R . The projection of X onto each of the image planes is denoted X_L and X_R . Points e_L and e_R are the epipoles.

cameras (WACs). The two cameras are fixed on a vertical mast with a baseline distance of approximately 20 centimetre. However, due to the mounting separation of the WACs, a slight error rotation may be produced between the homologous images. Fortunately, the angle of rotation between the two corresponding images can be obtained by calculating the difference angle of two pairs of feature points based on the SIFT-RANSAC algorithm. However for improving precision when a keypoint is matched on a rock, the nearest and secondary feature points are chosen from the desired keypoint to calculate the angle of rotation for each pair of images. The formula for computing the approximate location of a homologous point is as follows:

$$\theta = \arccos \frac{\overrightarrow{AB} \cdot \overrightarrow{A'B'}}{|\overrightarrow{AB}| |\overrightarrow{A'B'}|} \quad (3.22)$$

$$\arctan \overrightarrow{A'C'} = \arctan \overrightarrow{AC} + \theta \quad (3.23)$$

$$|\overrightarrow{A'C'}| = \frac{|\overrightarrow{AC}|}{|\overrightarrow{AB}|} \cdot |\overrightarrow{A'B'}| \quad (3.24)$$

where AA' and BB' are a pair of feature points obtained by SIFT. C is a matched point in the left image, C' is the rough matching point of C in the right image, θ is the rotation angle of a pair images, $\arctan \overrightarrow{AC}$ denotes the direction of vector AC and $|\overrightarrow{AC}|$ represents the distance from A to C . This is shown in Figure 3.11.

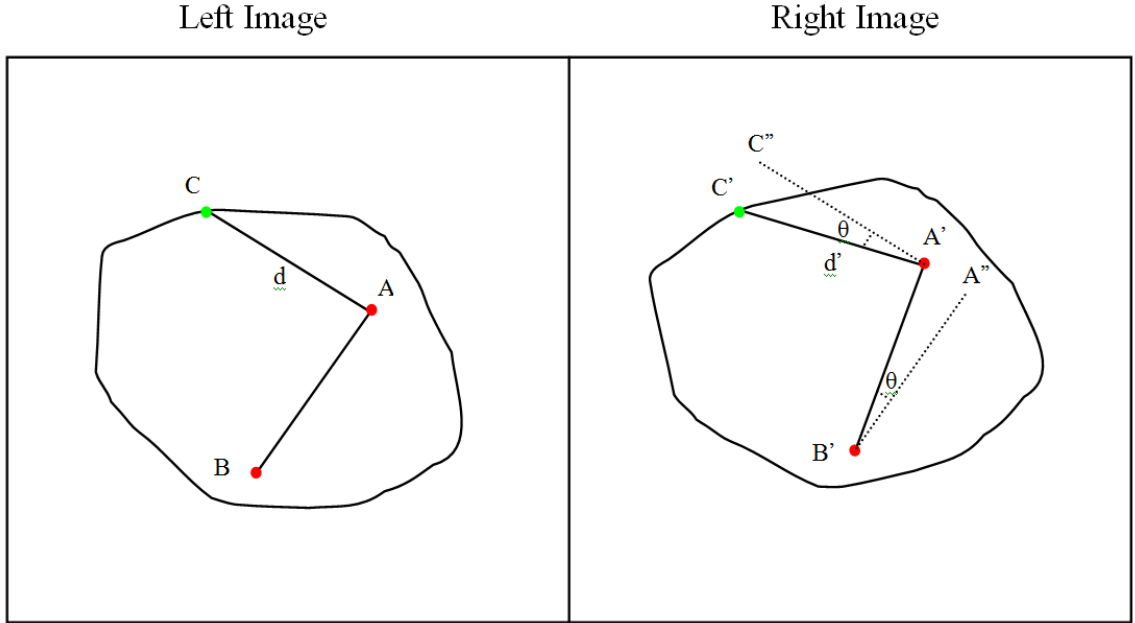


Figure 3.11: Angle of rotation determination.

3.3.5 Matching through Correlation

Matching interest points in two uncalibrated images is a fundamental problem in computer vision. Normalized cross correlation is widely used in many applications that require matching parts of images (Tsai & Lin, 2003). Traditional matching methods based on normalized cross-correlation can handle the situation where there are only translation or small rotation and scale changes between the two images. Since the images used in this work satisfy this condition, normalized cross-correlation is used here to perform accurate matching points.

The normalized cross correlation coefficient between two windows \mathbf{f} and \mathbf{g} of size

N is defined by:

$$r = \frac{\sum_{x=0}^{N-1} \sum_{y=0}^{N-1} f(x, y)g(x, y)}{\sqrt{\sum_{x=0}^{N-1} \sum_{y=0}^{N-1} f(x, y)^2 \sum_{x=0}^{N-1} \sum_{y=0}^{N-1} g(x, y)^2}} \quad (3.25)$$

where $f(x, y)$ and $g(x, y)$ are pixel values at the location (x, y) of f and g , respectively. The normalization helps reduce the effects of lighting differences between f and g , so that they have a mean of zero. The value of r changes between -1 and +1, and the closer r is to +1, the more similar the two windows will be.

When the search area is M and the template size is N ($N < M$), r is computed for each shift position (which is $(M - N + 1)^2$ shift positions) such that

$$r(u, v) = \frac{\sum_{x=0}^{N-1} \sum_{y=0}^{N-1} f(x, y)g(x + u, y + v)}{\sqrt{\sum_{x=0}^{N-1} \sum_{y=0}^{N-1} f(x, y)^2 \sum_{x=0}^{N-1} \sum_{y=0}^{N-1} g(x + u, y + v)^2}} \quad (3.26)$$

where $u, v = 0, 1, 2, \dots, M - N$.

Among all the computed r , the one with the largest value is taken to be the normalized cross correlation coefficient which is used to compute the best match.

In this work the search area is concerned with a certain part of the epipolar line, and the matched point is regarded as the center of the template. As shown Figure 3.12, the red square box is the template window and the center of the template is the matched point (i.e., the keypoint) in the left image. In the right image, the blue point is the rough matching point taken by the above proposed method. The projection point of the rough matching point is the orange point on the epipolar. The red line is the epipolar line and the green line, as a part of the epipolar line, is the search area, whose size depends on the distortion model of the camera calibration at both sides of the projection point using the same window with template window. Finally, the accurate matching point taken by the normalized cross correlation method is the red point on the green line.

3.3.6 Triangulation

According to the above analysis, the corresponding point of the desired keypoint can be derived in image pairs. Thus, if the camera calibration parameters are

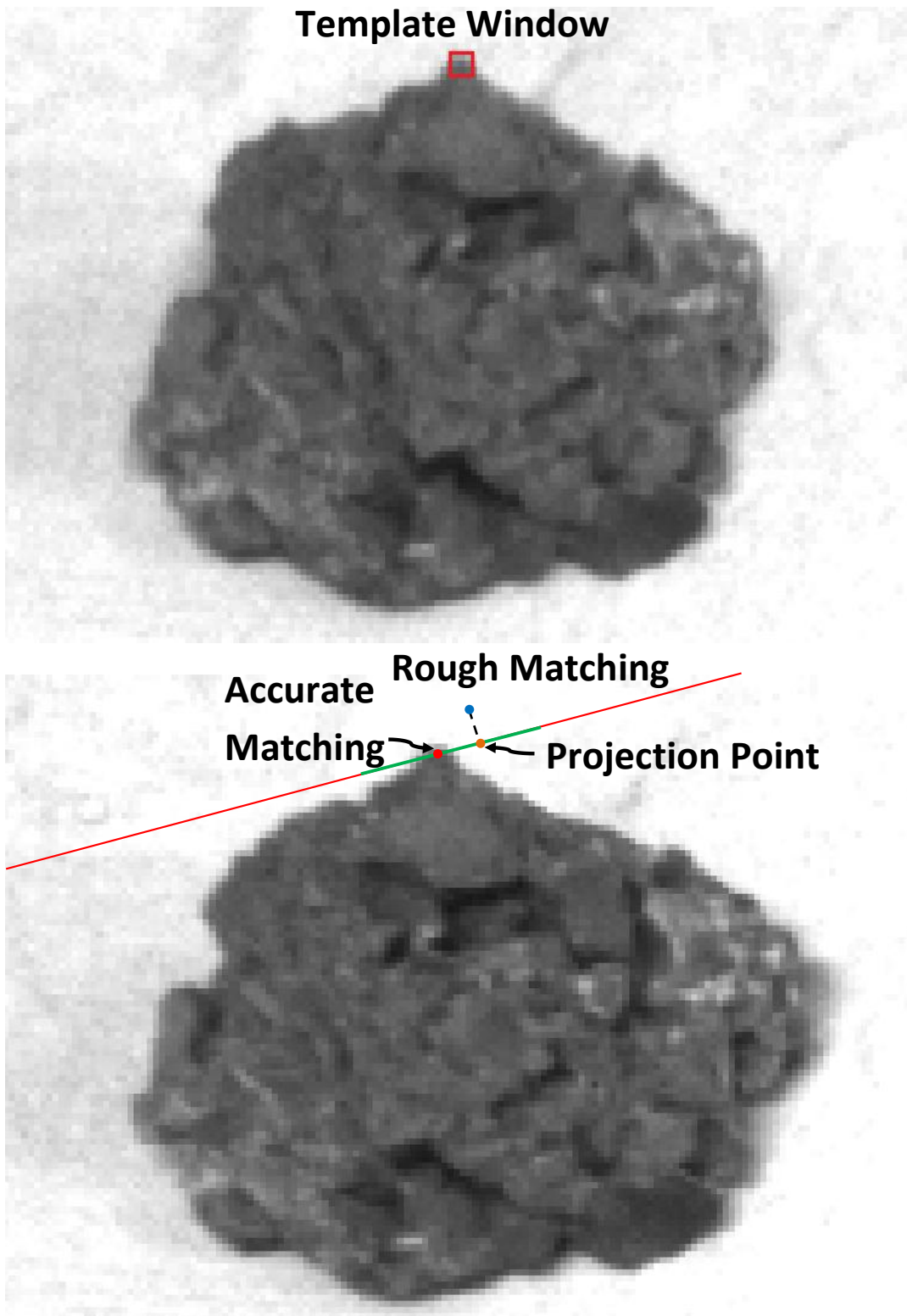


Figure 3.12: Correlation.

known, then the 3D point location of the desired keypoint is able to be reconstructed. Note that the camera calibration is completed in the Chapter 5. Here, the triangulation method is employed for the reconstruction of the 3D point location. For triangulation the linear algebraic approach is given as follows:

$$Z \begin{bmatrix} u_1 \\ v_1 \\ 1 \end{bmatrix} = M \begin{bmatrix} X \\ Y \\ Z \\ 1 \end{bmatrix} \quad (3.27)$$

$$Z \begin{bmatrix} u_2 \\ v_2 \\ 1 \end{bmatrix} = N \begin{bmatrix} X \\ Y \\ Z \\ 1 \end{bmatrix} \quad (3.28)$$

where $\begin{bmatrix} u_1 \\ v_1 \\ 1 \end{bmatrix}$ and $\begin{bmatrix} u_2 \\ v_2 \\ 1 \end{bmatrix}$ are correspondences in a pair of images.

$M = \begin{bmatrix} m_{11} & m_{12} & m_{13} & m_{14} \\ m_{21} & m_{22} & m_{23} & m_{24} \\ m_{31} & m_{32} & m_{33} & m_{34} \end{bmatrix}$ and $N = \begin{bmatrix} n_{11} & n_{12} & n_{13} & n_{14} \\ n_{21} & n_{22} & n_{23} & n_{24} \\ n_{31} & n_{32} & n_{33} & n_{34} \end{bmatrix}$ are the projection

matrices regarding the left camera and right camera, respectively. $\begin{bmatrix} X \\ Y \\ Z \\ 1 \end{bmatrix}$ represents

the space 3D coordinates. That is, each 2D point provides 2 independent equations for a total of 3 unknowns (which are X , Y , Z) based upon the equations (3.27) and (3.28). The four Linear equations are given as follows.

$$\begin{aligned} X m_{11} + Y m_{12} + Z m_{13} + m_{14} - u_1 X m_{31} - u_1 Y m_{32} - u_1 Z m_{33} &= u_1 m_{34} \\ X m_{21} + Y m_{22} + Z m_{23} + m_{24} - v_1 X m_{31} - v_1 Y m_{32} - v_1 Z m_{33} &= v_1 m_{34} \\ X n_{11} + Y n_{12} + Z n_{13} + n_{14} - u_1 X n_{31} - u_1 Y n_{32} - u_1 Z n_{33} &= u_1 n_{34} \\ X n_{21} + Y n_{22} + Z n_{23} + n_{24} - v_1 X n_{31} - v_1 Y n_{32} - v_1 Z n_{33} &= v_1 n_{34} \end{aligned} \quad (3.29)$$

This set of overconstrained equations are resolved using conventional Least-squares

method (Golub, 1965).

3.4 Experimental Study

3.4.1 Segmentation Based Upon Mars Images

The proposed approach has been implemented and run on a set of six representative Mars images, as listed in Table 3.1 to demonstrate its effectiveness via comparison with other conventional methods. These images are obtained from two datasets: the navigation camera (Navcam) imagery, and the panoramic camera (Pancam) imagery, both were acquired by the NASA Mars Exploration Rover (MER) and directly downloaded from Planetary Image Atlas of National Aeronautics and Space Administration (NASA) (<http://pds-imaging.jpl.nasa.gov/search/search.html#QuickSearch>). Note that during mission operations, Navcam is mounted on the optical bench of the rover for terrain mapping and navigation, and has a pair of monochrome stereo cameras; Pancam is fixed on the uniform optical bench and employed for scientific survey of the geology, morphology and topography on the landing sites (Bell *et al.*, n.d.). The six images selected involve distinct illuminations, spectral bands and scenes (see Table 3.1). Qualitative and quantitative approaches is employed for the evaluation of performance about image segmentation.

Table 3.1: Selected images for experimentation (Spirit Rover)

Image Name	Image NO.	Local Solar Sol/Time	Spectral Band	Instrument
2n136853953ilf4000p1977l0m1	1.png	118/16:04:42	-	NAVCAM
1p163700052edn5000p2384l2m1	2.png	400/14:43:25	753NM	PAMCAM
2p130811027edn1000p2421l6m1	3.png	50/14:00:54	483NM	PAMCAM
2p130974937eff1100p2568l7m1	4.png	52/10:20:08	440NM	PAMCAM
2p162142844esfa600p2558l5m1	5.png	403/13:42:44	535NM	PAMCAM
2p179724220esfaeghp2570l2c1	6.png	601/15:40:32	753NM	PAMCAM

3.4.1.1 Qualitative Comparison

Qualitative comparison is a comparison of human visual perception about the results of the different segmentation methods. Rock candidates considered in

this study are each with an area greater than 50 pixels. Figure 3.13 shows the resulting segmentations produced by Rockfinder, Rockster, Multiple Viola-Jones (MVJ), Marsokhod Shadow Detector, SVM Pixel Classification from (Thompson & Castano, 2007) and the present algorithm, for the image 1.png. Rockfinder finds only partial large rocks. Similarly, the Stereo method can only find the large rocks, but poor contours for the rocks are obtained. Rockster loses the main large rocks, but can find smaller rocks. The results of MVJ, Shadows and SVM methods fail to find the contour outlines of the rocks. As opposite to these method, the techniques proposed herein are effective in detecting the entire large rocks and gaining the relatively accurately the closed contours of the detected rocks.

The segmentation results of the proposed method and those of OTSU, Pugh's (Pugh & Barnes, 2007) and Fink's method (Fink *et al.*, 2008) are shown in Tables 3.2 - 3.4, for all six typical images. It can be seen that the segmentation effects of the proposed approach are more consistent with human visual perception than the others.

3.4.1.2 Quantitative Comparison

Quantitative comparison is a comparison carried out numerically to assess the results of the different segmentation methods. To quantitatively assess the accuracy of the proposed approach, the results are again compared with those obtained by the use of OTSU, Pugh's and Fink's methods. The underlying ground-truth images used in this study include a total of 128 rocks that have been identified manually. Precision, Recall and the misclassification error (ME) methods (Sezgin & Sankur, 2004) are adopted as the criteria to evaluate the grey-level images given in Tables 3.2 - 3.4. In particular, Precision denotes those detections which are actually true rocks; Recall represents the fraction of rocks which are detected; and ME quantifies the proportion of foreground pixels mistakenly allocated to the background and also, background pixels falsely attributed to the foreground. For binary segmentation these performance indices are defined by

$$Precision = \frac{|F_O \cap F_T|}{F_T} \quad (3.30)$$

$$Recall = \frac{|F_O \cap F_T|}{F_O} \quad (3.31)$$

Table 3.2: Qualitative comparison about 1.png and 2.png images amongst OTSU, Pugh's, Fink's and the present method.

	1.png	2.png
Original Image		
OTSU		
Pugh's Method		
Fink's Method		
Proposed Method		

Table 3.3: Qualitative comparison about 3.png and 4.png images amongst OTSU, Pugh's, Fink's and the present method.

	3.png	4.png
Original Image		
OTSU		
Pugh's Method		
Fink's Method		
Proposed Method		

Table 3.4: Qualitative comparison about 5.png and 6.png images amongst OTSU, Pugh's, Fink's and the present method.

	5.png	6.png
Original Image		
OTSU		
Pugh's Method		
Fink's Method		
Proposed Method		

$$ME = 1 - \frac{|B_O \cap B_T| + |F_O \cap F_T|}{|B_O| + |F_O|} \quad (3.32)$$

In the above, B_T and F_T represent the set of background pixels and that of foreground pixels in the test image, respectively, and B_O and F_O express the set of background and that of foreground pixels in ground-truth, respectively. Note that the value of ME varies from 0 for a completely perfect resulting segmentation to 1 for a totally wrong segmentation result.

Tables 3.5 and 3.6 list the results in terms of Precision and Recall respectively, for the four methods on the test images. For the images 1.png, 5.png and 6.png, the present work leads to the maximum precision. For the images 2.png, 3.png and 4.png the best results are obtained from OTSU, Pugh's and Fink's method, respectively. With regard to Recall, except for the image 3.png, the proposed approach result in the maximum value, while the best result for 3.png is obtained by Pugh's method. On average, the present work outperforms the other three with regard to this criterion. Furthermore, minimum ME is obtained for all the test images by the algorithm developed here as shown in Table 3.7.

Table 3.5: Comparison of Precision for the four methods

	1.png	2.png	3.png	4.png	5.png	6.png	AVG
OTSU	0.261	0.955	0.712	0.942	0.314	0.679	0.644
Pugh's	0.739	0.950	0.593	0.975	0.446	0.703	0.734
Fink's	0.246	0.948	0.846	0.967	0.247	0.663	0.653
Our	0.824	0.936	0.780	0.881	0.589	0.810	0.803

Table 3.6: Comparison of Recall for the four methods

	1.png	2.png	3.png	4.png	5.png	6.png	AVG
OTSU	0.533	0.808	0.532	0.298	0.297	0.433	0.484
Pugh's	0.785	0.826	0.791	0.387	0.722	0.708	0.703
Fink's	0.534	0.820	0.133	0.289	0.312	0.434	0.420
Our	0.871	0.868	0.703	0.784	0.785	0.857	0.811

Table 3.7: Comparison of ME for the four methods

	1.png	2.png	3.png	4.png	5.png	6.png	AVG
OTSU	0.332	0.091	0.090	0.109	0.108	0.155	0.148
Pugh's	0.083	0.089	0.099	0.094	0.094	0.119	0.096
Fink's	0.353	0.089	0.117	0.109	0.131	0.158	0.160
Our	0.053	0.076	0.065	0.049	0.061	0.069	0.062

3.4.2 Rocks Size Measurement and Results

3.4.2.1 PATLab

The experiments on the measurement of the size of rocks are accomplished in the AU Planetary Analogue Terrain Laboratory (PATLab) at Aberystwyth University (AU) (Barnes *et al.*, 2008). Facilities at PATLab allow emulation experiments on comprehensive mission operations to be performed. These trials and experiments are essential when learning how to deploy and use a robot science instrument (Tyler & Barnes, 2008) for a given mission, thereby maximizing potential quality scientific data return. Work has resulted in a unique facility that has a terrain region composed of Mars Soil Simulant-D. It includes science target rocks that have been fully characterized.

The PATLab terrian has been designed to support a new rover chassis which is based upon the ExoMars rover Concept-E mechanics (Chien *et al.*, 1998). It is heavily instrumented and all data and control facilities are available via high speed links to remote users. In particular, a panoramic camera instrument has been created to emulate the proposed ExoMars PanCam (Paar *et al.*, 2008). Experiments on the motion of the rover chassis wheel mechanics, rover attitude, robot arm deployment can be carried out, and PanCam pan and tilt mechanism can be measured using a Vicon motion capture system. The PATLab has a large selection of software tools for rover, robot arm and instrument modelling and simulation also, for the processing and visualisation of captured instrument data, and for simulating planetary environmental conditions.

3.4.2.2 Experimental Results

The experiments reported here were implemented using the Aberystwyth University PanCam Emulator at PATLab with two wide angle multi-spectral cameras (WACs). The intrinsic and extrinsic parameters of both cameras are obtained by

camera calibration (Heikkila & Silven, 1997). then rocks of different sizes were used for the experiments, including Rock 1, Rock 2, Rock3, CONGLOMERATE, BRECCIA, SANDSTONE aolian, SANDSTONE torridonian, MUDSTONE, OXFORD CLAY, CRINOIDAL LIMESTONE. The ground truths of the rock sizes were measured using a micrometer.

The following 10 Figures (Figure 3.14 - 3.23) present the matching results for calculating the size of each of the 10 rocks and the location of each rock centroid at the touchable point, using the proposed rock detection method in this work. In these figures, pink points represent the matched and matching points which are centroid, top-most, bottom-most, left-most and right-most points. Blue lines are the epipolar relative to the pink points. Yellow points denote the closest and secondary points obtained by SIFT with respect to pink points. Green points are the projection points of the rough matching points on the epipolar. The accurate matching points are shown by the red points.

A comparison was achieved between the present work and the standard disparity equation method. This traditional disparity method has been adopted here due to its maturity and also, its popularity in the literature (March, 1988). Tables 3.8 and 3.9 show the experimental results, nothing that the average error of using the proposed approach is 3.62% (this error includes measurement error and calibration error), whereas produced the average error when using the standard disparity method is 61.22%. The very large errors using the standard disparity method were not expected, and may be due to calibration errors. However, given that all experiments used the same calibrated images, these results demonstrate how resilient the present work is to possible systematic errors.

3.5 Summary

In this chapter, an unsupervised method for image segmentation has been proposed for Mars terrain images. An improved OTSU and Canny operator are utilized for detecting rock regions and their space relations respectively. The closed contours of detected rocks are gained by the use of template dilatation edge linking (TDEL) for a given set of images. Qualitative and quantitative comparisons have shown that the proposed approach outperforms many typical classical algorithms. A novel approach has been presented to measure the size of a detected rock. For this, the SIFT-RANSAC algorithm is used to properly match the prominent feature

Table 3.8: Distance of ToptoBottom (mm)

Rock Name	Proposed Method	Disparity Method	Micrometer Value
Rock 1	105.47	170.06	103.46
Rock 2	67.86	109.57	66.16
Rock 3	85.88	126.01	84.43
CONGLOMERATE	47.35	67.22	45.53
BRECCIA	49.71	72.03	46.73
SANDSTONE aolian	52.61	83.6	51.89
SANDSTONE torridonian	46.42	73.42	45.86
MUDSTONE	62.74	112.2	59.85
OXFORD CLAY	51.91	75.33	48.66
CRINOIDAL LIMESTONE	52.89	82.89	49.38

Table 3.9: Distance of LefttoRight (mm)

Rock Name	Proposed Method	Disparity Method	Micrometer Value
Rock 1	161.52	249.02	158.96
Rock 2	96.86	146.47	96.15
Rock 3	98.35	157.61	95.68
CONGLOMERATE	56.55	88.97	54.06
BRECCIA	58.33	95.08	57.75
SANDSTONE aolian	51.33	78.61	50.61
SANDSTONE torridonian	67.26	105.38	63.68
MUDSTONE	66.27	105.41	63.15
OXFORD CLAY	59.73	91.65	55.54
CRINOIDAL LIMESTONE	59.38	89.04	56.5

points in a given pair of images. The work carries out an initial rough matching of non-feature points based upon those feature points found by SIFT-RANSAC, and then a correlation method is applied for accurately matching the points. A comparison is achieved between the proposed method and the standard disparity equation method using real rocks. The experiment results have demonstrated that the average error of the proposed work is less than that of the standard disparity technique.

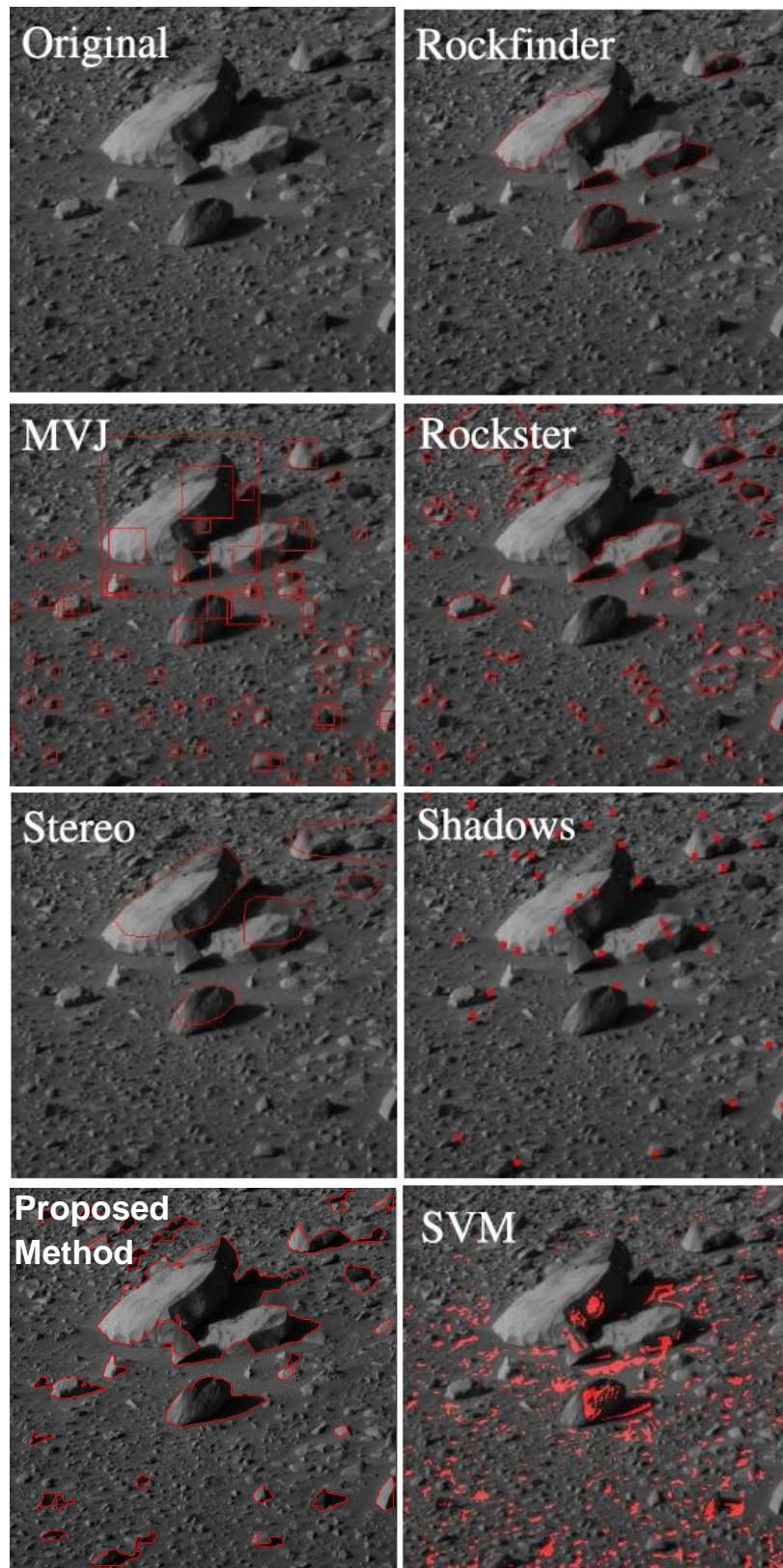


Figure 3.13: Qualitative comparison among the results using different methods.

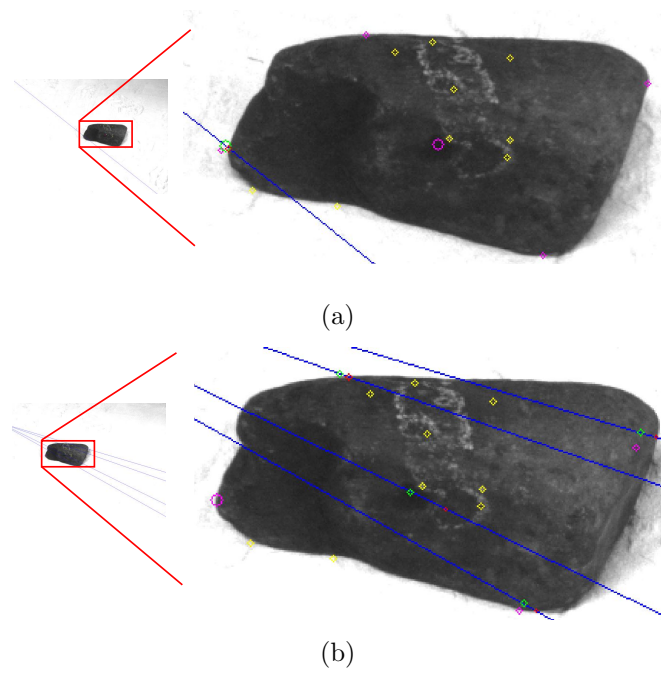


Figure 3.14: Matching algorithm results for rock 1 ((a): left image results. (b): right image results).

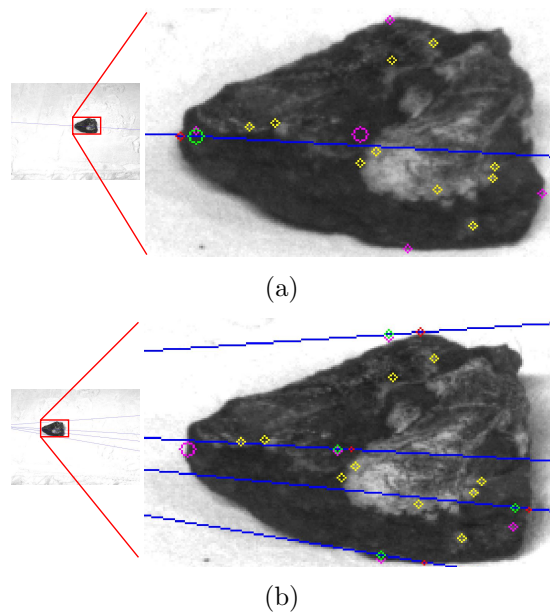
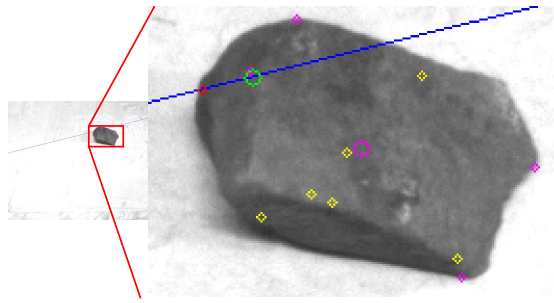
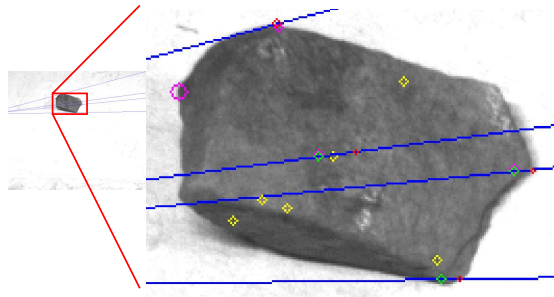


Figure 3.15: Matching algorithm results for rock 2 ((a): left image results. (b): right image results).

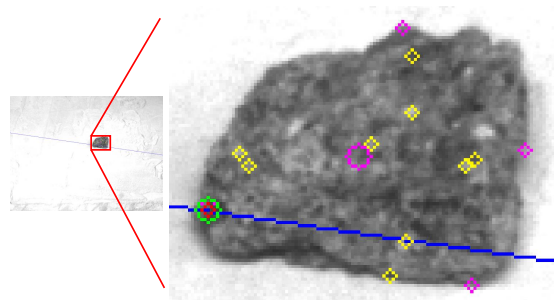


(a)

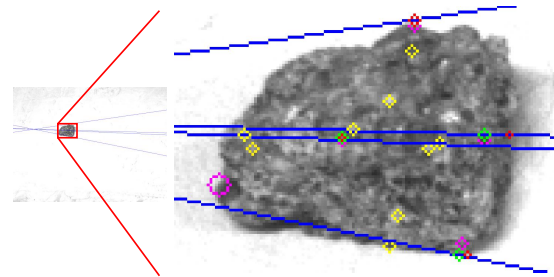


(b)

Figure 3.16: Matching algorithm results for rock 3 ((a): left image results. (b): right image results).



(a)



(b)

Figure 3.17: Matching algorithm results for rock CONGLOMERATE ((a): left image results. (b): right image results).

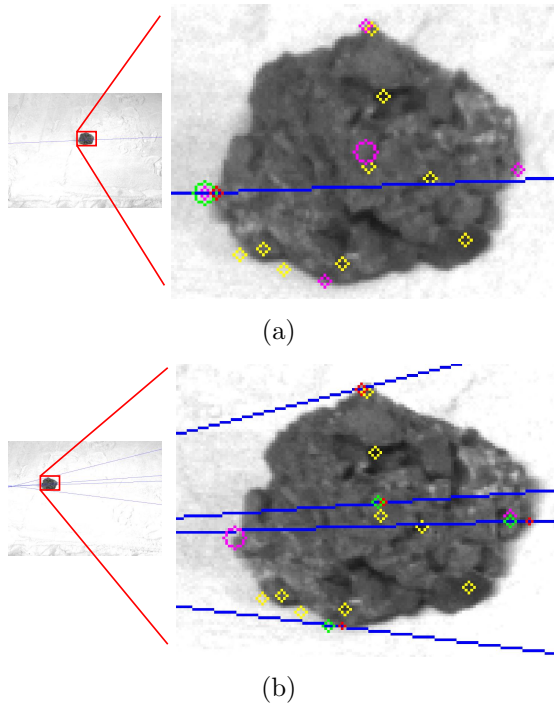


Figure 3.18: Matching algorithm results for rock BRECCIA ((a): left image results. (b): right image results).

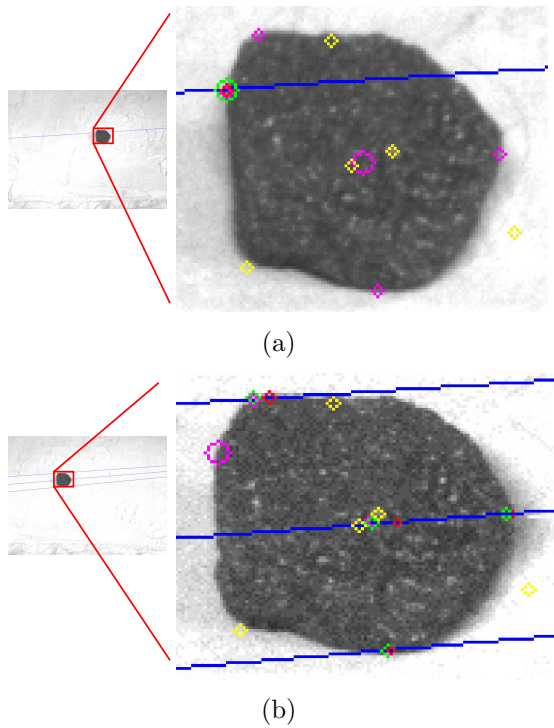


Figure 3.19: Matching algorithm results for rock SANDSTONE aolian ((a): left image results. (b): right image results).

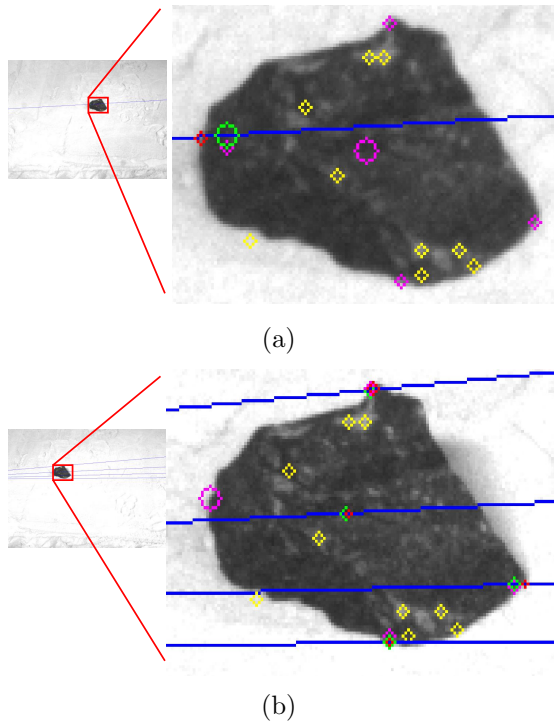


Figure 3.20: Matching algorithm results for rock SANDSTONE torridonian ((a): left image results. (b): right image results).

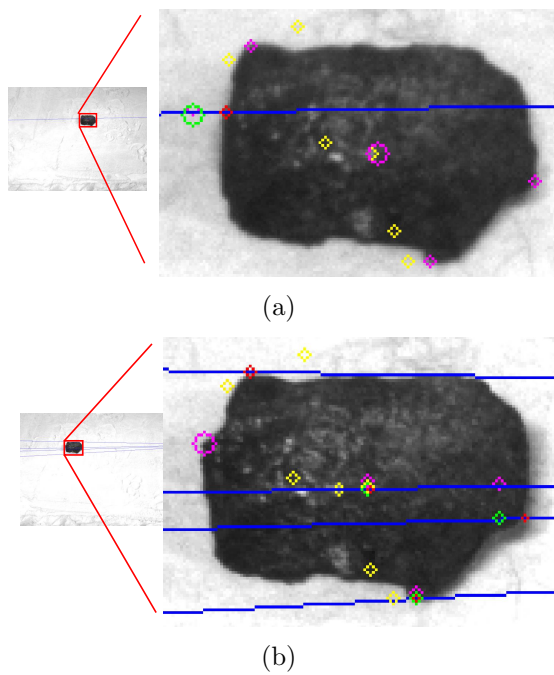


Figure 3.21: Matching algorithm results for rock MUDSTONE ((a): left image results. (b): right image results).

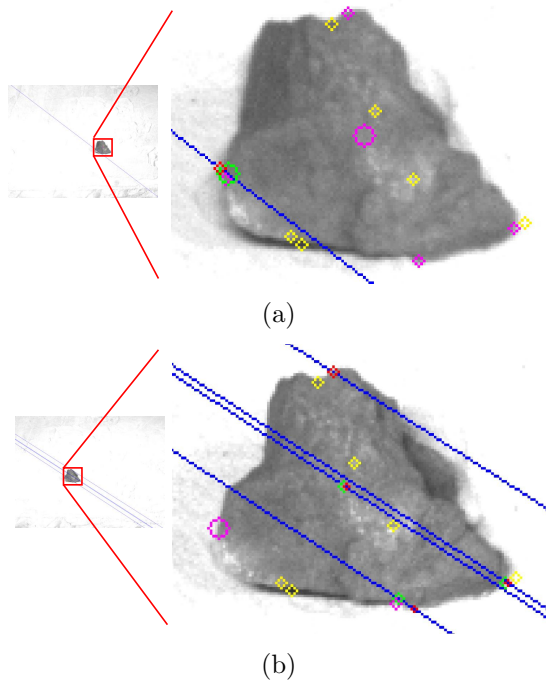


Figure 3.22: Matching algorithm results for rock OXFORD CLAY ((a): left image results. (b): right image results).

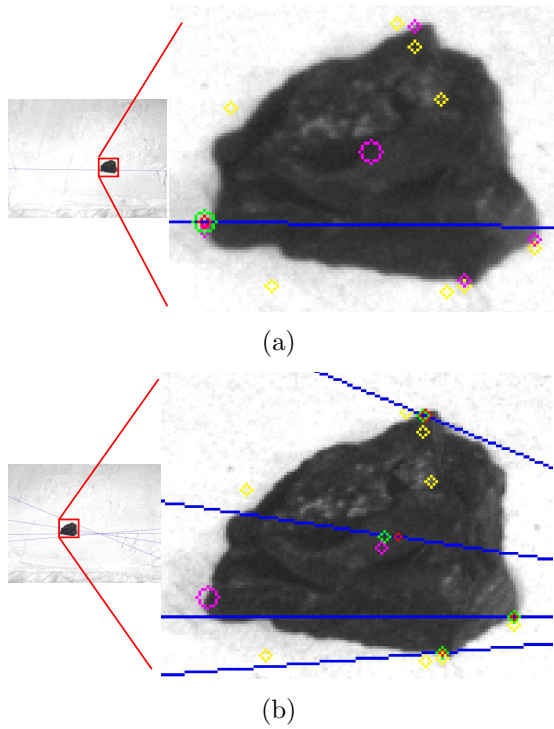


Figure 3.23: Matching algorithm results for rock CRINOIDAL LIMESTONE ((a): left image results. (b): right image results).

Chapter 4

Designing Algorithms for Touchability Index Evaluation

Fuzzy systems have already been applied in a variety of aspects for planetary exploration, such as rover navigation (Martin-Mur *et al.*, 2014), path planning (Carsten *et al.*, 2007) and science value assessment (Woods *et al.*, 2009). In this chapter, a fuzzy logic-based controller for the touchability of the science targets has been achieved. Here, touchability is deemed to be the capability of whether a positive decision can be made in that a potential science target can be reached by the robotic hand (for instrument deployment and sampling). The membership functions and fuzzy rules have been designed and the defuzzification has been finally carried out under the domain expert's instruction. The simulation experiment about the rank of science objects touchability has accomplished and the result has shown the validity of the proposed system.

4.1 Background

The application of fuzzy logic in planetary exploration is currently one important subject of studies. Recently, Seraji (Seraji, 1999) proposed the construction of a so-called traversability index, which is meant to classify the difficulty a rover would encounter when attempting to traverse a region of terrain in a no priori knowledge environment. Howard et al. (Howard *et al.*, 2002) have presented an approach that combines the traversability map with a fuzzy map representation of traversal difficulty of the terrain, involving the path planning logic. This approach

concentrates on planning over an optimally safe path of minimum traversal cost. Mahmoud (Mahmoud, 2008) has utilized a fuzzy adaptation technique that examines the paths population throughout the execution of the underlying algorithm and adjusts operator probabilities to attain better solutions for path planning.

Not only has fuzzy logic been employed for the achievement of the traversability and path planning, it has also seen applied to planetary landing and the tier-scalable robotic planetary reconnaissance. Navid (Navid & Homayoun, 2007) has addressed the issue of landing site selection using fuzzy rule-based reasoning. In that work the score of each potential candidate landing site is obtained from sensor measurements that are feed into the fuzzy system to settle spatial and temporal dependence in the reasoning process. Furfaro et al. (Furfaro *et al.*, 2008) have built a fuzzy system where the appropriate past/present water/energy indicators can be acquired when the tier-scalable mission framework is deployed, and used to estimate the habitability on Mars. Barnes et al. (Barnes *et al.*, 2009), and Pugh et al. (Pugh, 2009), have proposed a fuzzy rule based expert system (KSTIS 1.0) that adopts knowledge elicitation from a planetary geologist to obtain the primary clues (Structure, Texture and Composition) regarding the geological background of the rock. The system can generate a useful science value score (SV) with respect to each rock in a given image.

4.2 Fuzzy Control System

Fuzzy control systems are emerged on the foundation of Zadeh's fuzzy set theory (Zadeh, 1965). A fuzzy control system is an intelligent control system that simulates human thinking and reacts on the basis of fuzzy logic. Here, the word "fuzzy" is utilized to represent terms that are either not well-known or not clear enough, or their closer specification depends on subjectivity, estimation, and even the intuition of the person who is describing these terms.

In this section, the basic definitions of fuzzy sets and operators on fuzzy sets are described. It is necessary to introduce the basic definitions of terms such as linguistic variables, fuzzy propositions, relations, implications, and inference engines. The way of defuzzification, namely, calculation of crisp controller output values, is presented. The description also covers the fuzzy controller structure that is most generally used in practice.

4.2.1 Fuzzy Sets

In order to define and illustrate a fuzzy set, the following example is used. Let A be a set X of all integers greater than 10. This statement can be written as:

$$A = \{x : x \in X, x > 10\} \quad (4.1)$$

Let B be set of all integers much greater than 10. The statement can be expressed as:

$$B = \{x : x \in X, x \gg 10\} \quad (4.2)$$

In these two sets the key difference is that set A is fully defined by relation (4.1), whilst relation (4.2) is not enough for a complete definition of set B. The reason is that the term much greater is of vagueness. It is obvious that 11, 12, 1234, and 3456 belong to the elements of set A. A majority of people will agree that 12345 and 67899 undoubtedly belong to set B. But they will doubt if 17 is an element of set B.

This problem can be solved if one uses an alternative way of describing a set. According to traditional set theory, a set can be defined by its characteristic function. In other words, instead of individually declaring each element of a set a function can take on values 1 or 0 depending on full membership or no membership of a particular element belonging to that set, respectively.

Definition 1 (*Characteristic function and crisp set*) Let S be a set from the domain X . A characteristic function of the set S attains value $\mu_S(x) = 1$ if $x \in S$, and $\mu_S(x) = 0$ if $x \notin S$, $\mu : X \rightarrow \{0, 1\}$. Set S with such a characteristic function is called a crisp set.

The characteristic function cannot describe set B in the above example, that is, it cannot deal with the vagueness in determining the lowest integer which would belong to set B. However, broadening the notion of a characteristic function offers an elegant way to define set B. Instead of determining the lowest integer belonging to set B, we may say that all integers greater than 10 belong to set B but with a different membership degree. The characteristic function, obtaining partial, or graded, values from the interval $[0, 1]$, now becomes a membership function.

Definition 2 (*Membership function and fuzzy set*) Let F be a set from the domain X . A membership function $\mu_F(x)$ of set F is a function that assigns a value, or membership degree, to every $x \in F$, $\mu : X \rightarrow [0, 1]$. Then set F is called a fuzzy set.

Crisp sets can be treated as a special case of fuzzy sets since the characteristic function can assume only margin values from the interval $[0, 1]$ on which a membership function is defined.

Now fuzzy set B can be completely defined as a set of pairs:

$$\mu_B(x) = \begin{cases} 0, & x < 10 \\ \frac{x-10}{100}, & 10 \leq x \leq 110 \\ 1, & x > 110 \end{cases} \quad (4.3)$$

From the above definition we can see that numbers with membership degree 0 do not belong to fuzzy set B . Number 11 is an element of B with membership degree $\mu_B(11) = 0.01$, while membership degree of number 100 $\mu_B(100) = 0.9$. Fuzzy set B is pictured in Figure 4.1.



Figure 4.1: A graphical representation of a fuzzy set.

In fuzzy sets theory, the domain or collection of possible quantitative values considered as the fuzzy set members is called the universe of discourse. A universe

of discourse can be continuous or discrete. A discrete universe of discourse is normally bounded and contains a finite number of elements. A fuzzy set defined on a discrete universe of discourse is called a discrete fuzzy set. The measure of fuzziness of each element is determined using a membership function spread either over a part or over the entire universe of discourse. The membership function converts the degree of fuzziness into the normalized interval $[0, 1]$ where the boundary values 0 and 1 resemble the membership degrees of crisp set members. Membership functions can attain different forms. However, triangular, trapezoidal, Gaussian, and bell-shaped forms, shown in Figure 4.2, are used more than others:

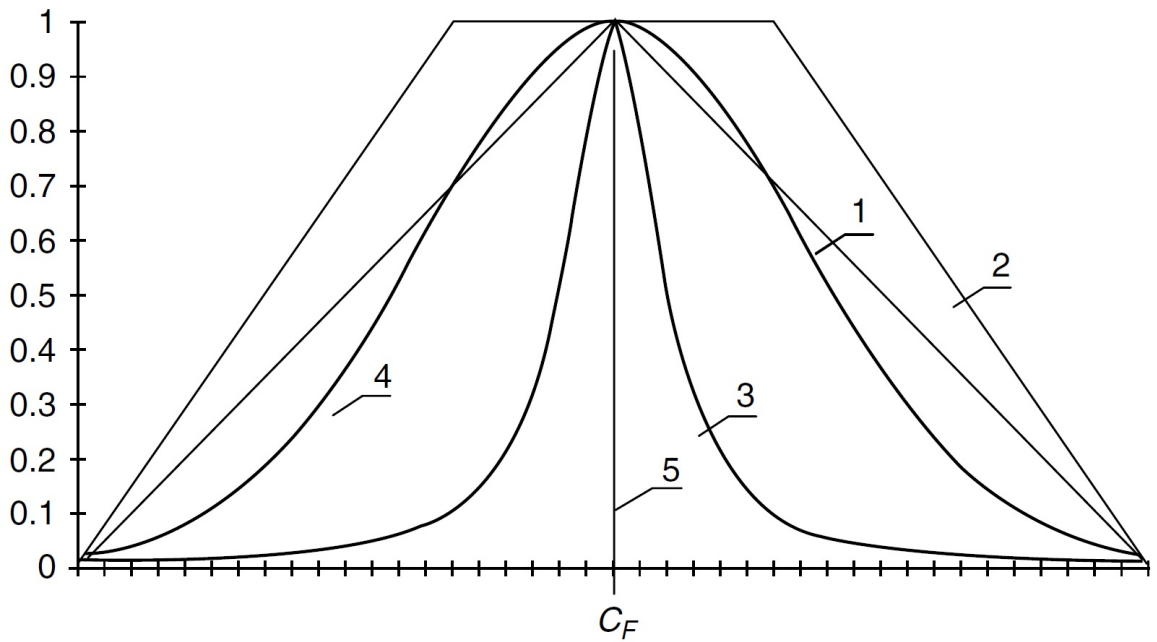


Figure 4.2: Typical shapes of membership functions: 1: triangular, 2: trapezoidal, 3: Gaussian, 4: bell-shaped, 5: singleton.

$$\text{triangular} : \quad \mu_F(x) = \begin{cases} 0, & x < a \\ \frac{x-a}{b-a}, & a \leq x \leq b \\ \frac{c-x}{c-b}, & b \leq x \leq c \\ 0, & x > c \end{cases} \quad (4.4)$$

$$\text{trapezoidal : } \mu_F(x) = \begin{cases} 0, x < a \\ \frac{x-a}{b-a}, a \leq x \leq b \\ 1, b \leq x \leq c \\ \frac{c-x}{c-b}, c \leq x \leq d \\ 0, x > d \end{cases} \quad (4.5)$$

$$\text{Gaussian : } \mu_F(x) = e^{-(x-C_F)^2/w} \quad (4.6)$$

$$\text{bell - shaped : } \mu_F(x) = \frac{1}{1 + (x - C_F)^2} \quad (4.7)$$

4.2.2 Linguistic Variables

In daily life and communication we often use short words and sentences, which carry the same amount of information as their longer counterparts. In speaking of age, when we say that “Roger is young”, we are less precise than when we say, “Roger is 22”. In this sense, the label “young” may be taken as a linguistic value of the variable Age, with the understanding that it plays a similar role as the numerical value 22 but is less precise and hence less informative. Variables, whose values are not numbers but words or sentences in a natural or artificial language, are called linguistic variables. Linguistic variables may assume different linguistic values over a designated universe of discourse. This means that linguistic values introduced by an appropriate semantic rule represent nothing but informative attributes about the physical values defined over a certain part of a specified universe of discourse.

A linguistic variable can be expressed in this way:

$$[x, T, X, M] \quad (4.8)$$

where, x is the name of a linguistic variable, $T = \{T_i\}$ is the set of linguistic values which x may attain, $i = 1, 2, \dots, l$, X is the quantitative universe of discourse of x . M is the semantic function which associates linguistic values in T with the universe of discourse X , that is, M is a mapping relation between T and X .

Definition 3 (*Fuzzy proposition*) Let $x \in X$ be a linguistic variable and $T_i(x)$ be a fuzzy set associated with a linguistic value T_i . Then the structure

$$P_i : \quad x \text{ is } T_i \quad (4.9)$$

written in modified notation also as $P_i^x : x \text{ is } T_i$, expresses a fuzzy proposition.

A fuzzy proposition can be interpreted by a process known as fuzzification.

Definition 4 (*Fuzzification*) Let $x \in X$ be a linguistic variable and $T_i(x)$ be a fuzzy set associated with a linguistic value T_i . The conversion of a numerical value of x into a corresponding linguistic value by associating a membership degree, $x \rightarrow \mu_{T_i}(x)$ is called fuzzification. The membership degree $\mu_{T_i}(x)$ represents the fuzzy equivalent of the value of x .

The definition of a linguistic variable, as well as definitions of a fuzzy proposition and fuzzification are illustrated with the following example.

Suppose that the size of the rocks takes values between 0 and $+\infty$. Then a possible fuzzy definition of a rock's size as a linguistic variable could be:

$$x: \text{Size}, \quad T: \{Small, Medium, Large\}, \quad X:(0, +\infty), \quad \text{and } M : X \rightarrow T$$

where the linguistic terms may be defined as:

$$\begin{aligned} \text{Small} &= \{(\mu_S(x), x) \mid x \in X\}, \\ \text{Medium} &= \{(\mu_M(x), x) \mid x \in X\}, \\ \text{Large} &= \{(\mu_L(x), x) \mid x \in X\}. \end{aligned}$$

whose membership functions are defined by:

$$\mu_S(x) = \begin{cases} 1, & x < 100 \\ \frac{300-x}{200}, & 100 \leq x \leq 300 \\ 0, & x > 300 \end{cases} \quad (4.10)$$

$$\mu_M(x) = \begin{cases} 0, & x < 100 \\ \frac{x-100}{200}, & 100 \leq x \leq 300 \\ \frac{600-x}{300}, & 300 \leq x \leq 600 \\ 0, & x > 600 \end{cases} \quad (4.11)$$

$$\mu_L(x) = \begin{cases} 0, & x < 300 \\ \frac{x-300}{300}, & 300 \leq x \leq 600 \\ 1, & x > 600 \end{cases} \quad (4.12)$$

According to the semantic function M , the fact that the numerical value of the size is equal to 360 may be interpreted using a fuzzy proposition:

size is medium

The fuzzy equivalent of the value 360 is obtained by fuzzification, that is, by inclusion of 360 in the relation that describes the membership function of the fuzzy set medium(x):

$$\mu_M(x) = \frac{600-360}{300}, 300 \leq x \leq 600 = 0.8$$

Fuzzy propositions are the building blocks of a fuzzy controller. They are elements used for description of one's experience or knowledge. Very often, two or more fuzzy propositions are put in the relation (in case of multiple input and multiple output controller configurations) to describe more complex knowledge about a control process.

4.2.3 Fuzzy Rules

Before fuzzy rules are presented, it is necessary to understand what a fuzzy relation is.

Definition 5 (*Fuzzy relation*) Let $x \in X$ and $y \in Y$ be linguistic variables, and $T_i(x)$ and $F_i(y)$ be fuzzy sets corresponding to the linguistic variables x and y , respectively. Then the structure

$$P_{ij} : \quad x \text{ is } T_i \quad \Psi \quad y \text{ is } F_j \quad (4.13)$$

denotes a fuzzy relation where Ψ represents an operator (the classical operators include AND and OR). The objective of fuzzy controllers is to make human-like decisions or simulate a human's actions through the use of the knowledge for controlling a target system. The selection of Ψ directly affects the structure of the resulting fuzzy controller. This is able to be achieved with fuzzy rules that constitute a fuzzy rule base, which is a central part of the fuzzy controller and is the representative of the "intelligence" in fuzzy control algorithms. An appropriate set of fuzzy rules are formed by the experience and knowledge of the system designer.

Definition 6 (*Fuzzy rule*) *Let X and Y be either fuzzy relations or fuzzy propositions. The the structure*

$$FR : \quad IF \quad X \text{ Then } Y \quad (4.14)$$

is called a fuzzy rule.

Each fuzzy rule can be partitioned into an antecedent part (IF relation) and a consequent part (THEN proposition), in which the antecedent part describes cause and the consequent part describes consequence or the control action. Such a form of fuzzy rules enables nonlinear mapping between inputs and outputs and thus enables the creation of versatile static nonlinear control functions. The nonlinear character of these functions allows fuzzy logic controllers to cope successfully with complex nonlinear control problems.

4.2.4 Defuzzification

The result of fuzzy inference through the use of a fuzzy rule base is a fuzzy output set. On the other hand, every control task will imply the existence of a crisp value at the fuzzy controller output. The procedure which extracts the crisp output value from a fuzzy output is called defuzzification.

There are various kinds of defuzzification. However, the crisp output value is most frequently calculated in control application according to the center of gravity

(COG) principle in the following way:

$$y^* = \frac{\sum_i u_i(y_k) \sum_{j=1}^r \mu_{FR^j}(x_k, y_k)}{\sum_i \sum_{j=1}^r \mu_{FR^j}(x_k, y_k)} \quad (4.15)$$

where y^* is the defuzzified output, r is the number of fuzzy rules activated by the crisp inputs x_k and $u_i(y_k)$ is the membership value of the output variable.

From Equation 4.15 it may be seen that the COG method does not require aggregation since it already works with individual output fuzzy sets obtained after the processing of fuzzy rules. The distinct features of this method are marked simplicity and very low computing effort. This is the main reason why this method of defuzzification is used for the present fuzzy controller design. The second reason is that if the max aggregation is used and several rules are activated, only the consequent associated with the highest membership function will contribute to the crisp output value, negating others. Ignoring the rules with lower membership functions may create a situation where a greater weight may be given to rules that are perhaps less important. The COG method takes into account such a situation and calculates contributions of all activated rules regardless of the fact that what rules are activated to generate the consequent parts may be the same.

4.2.5 Structure of Fuzzy Controllers

The structure of a fuzzy controller mainly depends on the process under control and the demanded quality of control. Since the application area for fuzzy control is really wide, there are many possible controller structures. These may differ significantly with respect to the number of inputs and outputs, the number of input and output fuzzy sets and their membership functions forms, or the form of control rules, the type of inference engine, and the method of defuzzification. It is up to the designer to decide which controller structure may be optimal for a particular given problem.

Despite the variety of possible fuzzy controller structures, the basic form of all common types of controller consists of:

- Input fuzzification
- Fuzzy rule base

- Inference engine
- Output defuzzification

The basic structure of a fuzzy controller is shown in Figure 4.3.

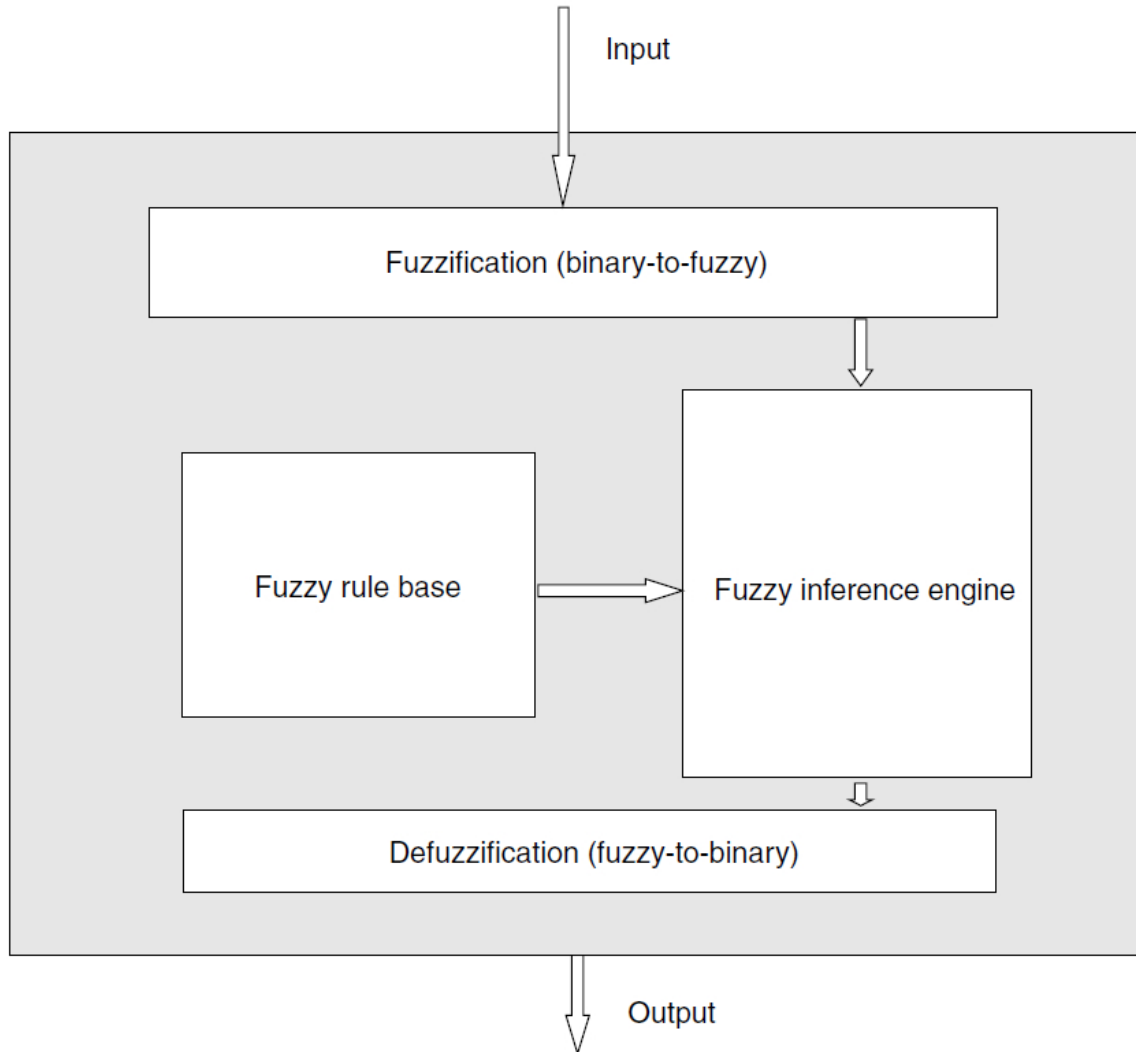


Figure 4.3: Basic structure of a fuzzy logic controller.

4.3 Fuzzy Logic Control of Touchability System

4.3.1 Overview of the Touchability System

This section introduces the structure of the proposed fuzzy logic based touchability system shown in Figure 4.4. The entire system is composed of six parts, which

are the vision system, KSTIS 1.0 (the Knowledge based Science Target Identification System), fuzzification, fuzzy inference engine, rule base and defuzzification. The inputs of the fuzzy logic controller are the outputs from the sensors of the vision system and KSTIS 1.0. The ability to autonomously detect and identify the scientifically interesting rocks and to accurately match and calculate the 3D location and the size of the targets, can be supported by this system (Gui *et al.*, 2012b; Gui *et al.*, 2012a).

In this control system the input data i_d, i_o, i_s are: the distance between arm base and the centroid of the target, the orientation of the arm's shoulder azimuth, and the size of the science target in the image, respectively. KSTIS 1.0 aims at assisting in ground-based interpretation of scientific targets via making use of a fuzzy expert system (Barnes *et al.*, 2009; Pugh, 2009). This system is based on the *Structure*, *Texture* and *Composition* associated with scientific targets whose values are provided by scientists/experts on Earth, and i_{SV} is the score of *Science Value* from KSTIS 1.0. The output signal o_t from the fuzzy controller is the touchability probability for the scientific targets.

4.3.2 Proposed Approach

The proposed fuzzy logic approach is uncomplicated, easy to comprehend, and provides a quick reaction capability. The resulting fuzzy logic controller for the touchability system adopts the conventional structure that includes fuzzification, inference mechanism and defuzzification. In the following these components are presented.

4.3.2.1 Fuzzification

The fuzzification procedure maps the crisp input values to the linguistic fuzzy terms with membership function values between zero and one. In this section the four physical properties i.e., size, distance, orientation and SV are expressed by linguistic fuzzy sets as described below.

4.3.2.1.1 Size (i_s) The bounding area is characterized as the size of the object. Currently the typical way such as MER (Thompson & Castano, 2007) to identify the surroundings of an object is to form a detailed DEMs (Digital Elevation

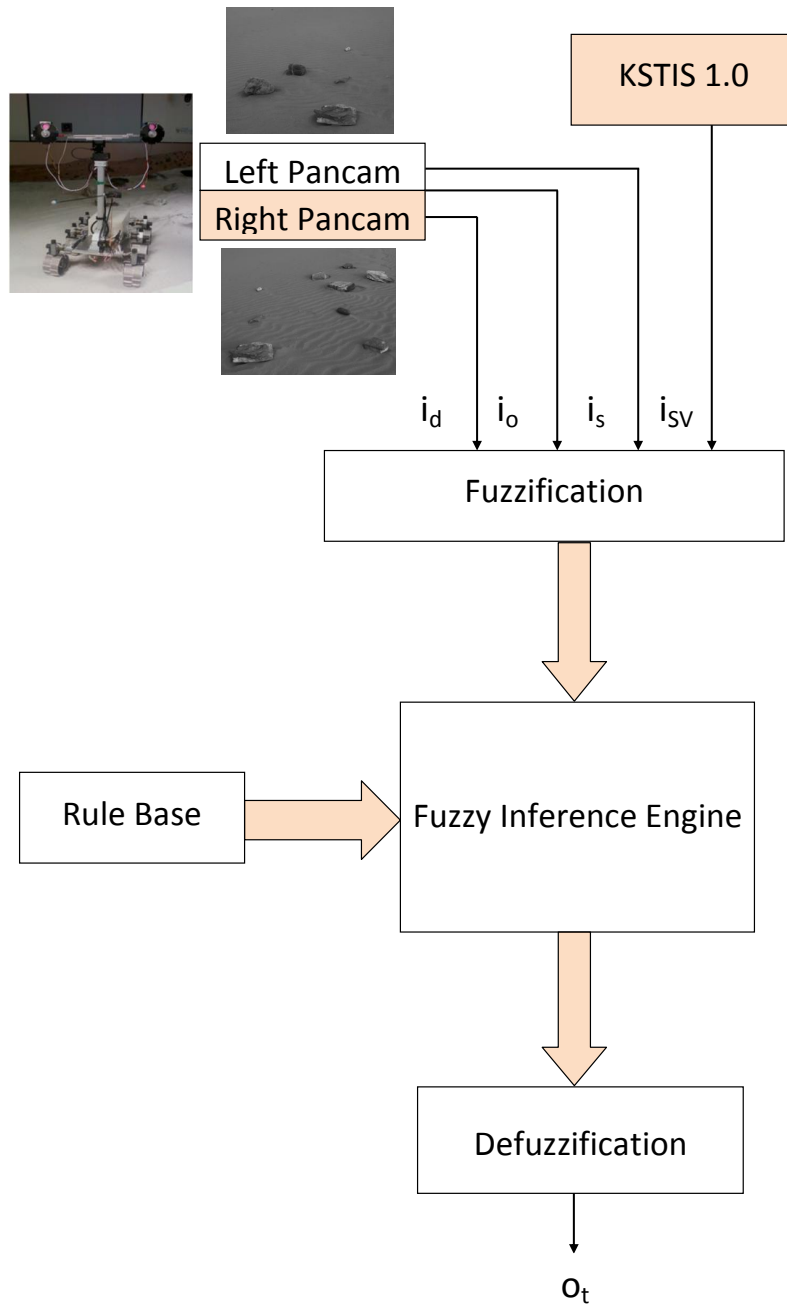


Figure 4.4: Fuzzy Logic Touchability Controller.

Models) by accomplishing stereo matching to the entire pixels in a pair of images. However in this study, in order to obtain the essential size information effectively just 5 points per object are applied for stereo matching (see Figure 4.5). In this figure the minimum rectangle (A , B , C and D) for each edge inscribes the leftmost, rightmost, uppermost and bottommost points (P_3 , P_4 , P_1 and P_2) of the

object, respectively. E , F , G and H are the middle points of the line segments ‘AB’, ‘BC’, ‘CD’ and ‘AD’, respectively. The point $C0$ is the cross point of the line segments ‘EG’ and ‘HF’ and is the centroid of the object. $P1$, $P2$, $P3$ and $P4$ represent the stereo matching points, whose three dimensional frame values are then derived by the external and internal parameters of the cameras.

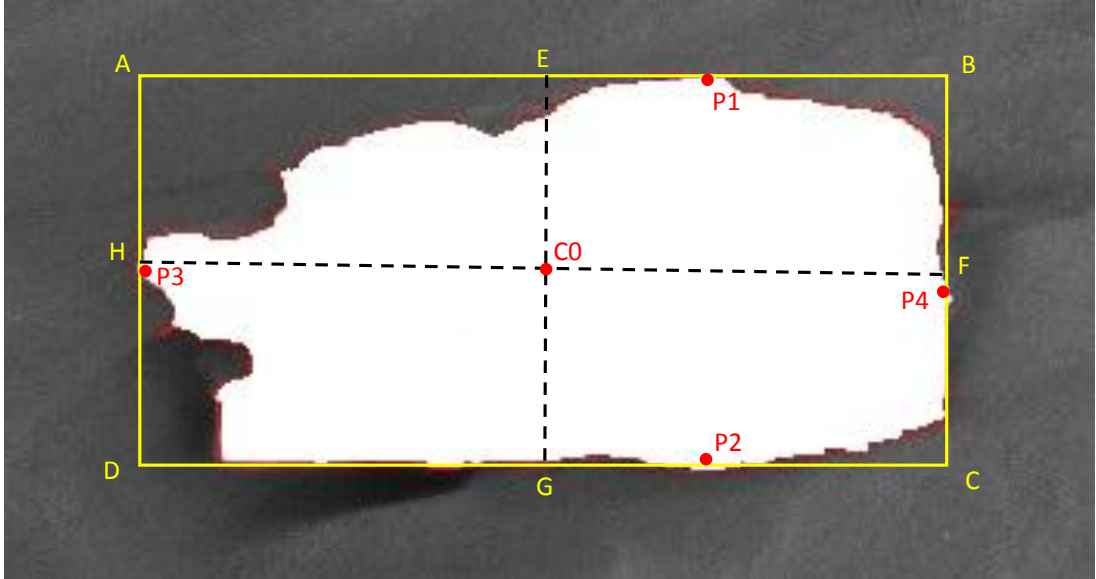


Figure 4.5: Stereo matching points selection.

The three linguistic fuzzy sets {SMALL, MEDIUM, BIG} are utilized to describe the size that is set up on the main five levels of object size. These levels are represented in Table 4.1. The membership functions of these fuzzy sets are empirically defined as given in Figure 4.6.

Table 4.1: Membership function levels for Size.

Level No.	Small	Medium	Big	Area(cm^2)
0	1	0	0	0
1.5	0.5	0.5	0	150
3	0	1	0	300
4.5	0	0.5	0.5	450
6	0	0	1	>600

4.3.2.1.2 Distance (i_d) The distance is a significant physical variable in this study, whose span is provided by the length of the robot arm. Here, we have employed the length of the Curiosity rover arm for subsequent simulation experiments. The length of the Curiosity arm is 2.3 meters from the front of the rover

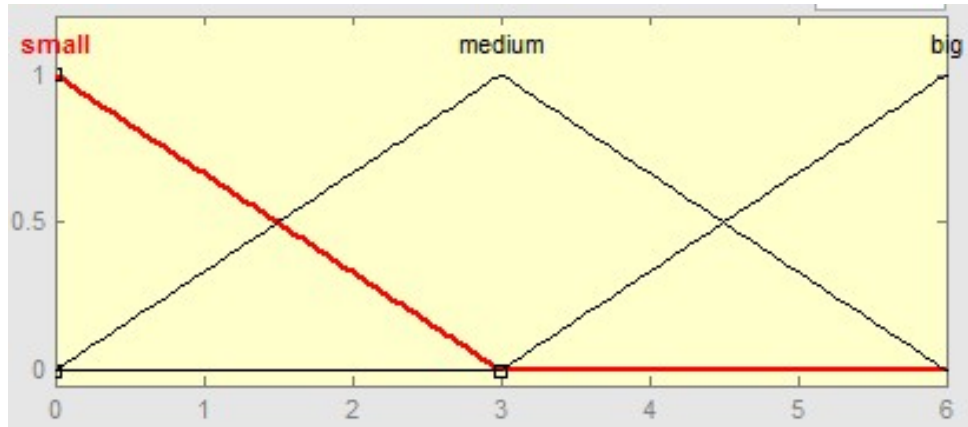


Figure 4.6: Membership functions for the Size (i_s).

body. In Figure 4.7, the distance is between the original point O in the mobile robot arm base frame seen and the centroid (C) of the object. The distance is represented by the three linguistic fuzzy sets {NEAR, MEDIUM, FAR}, which is again set up on five levels of the distance. These levels are represented in the Table 4.2. The membership functions of these fuzzy sets are given in Figure 4.8.

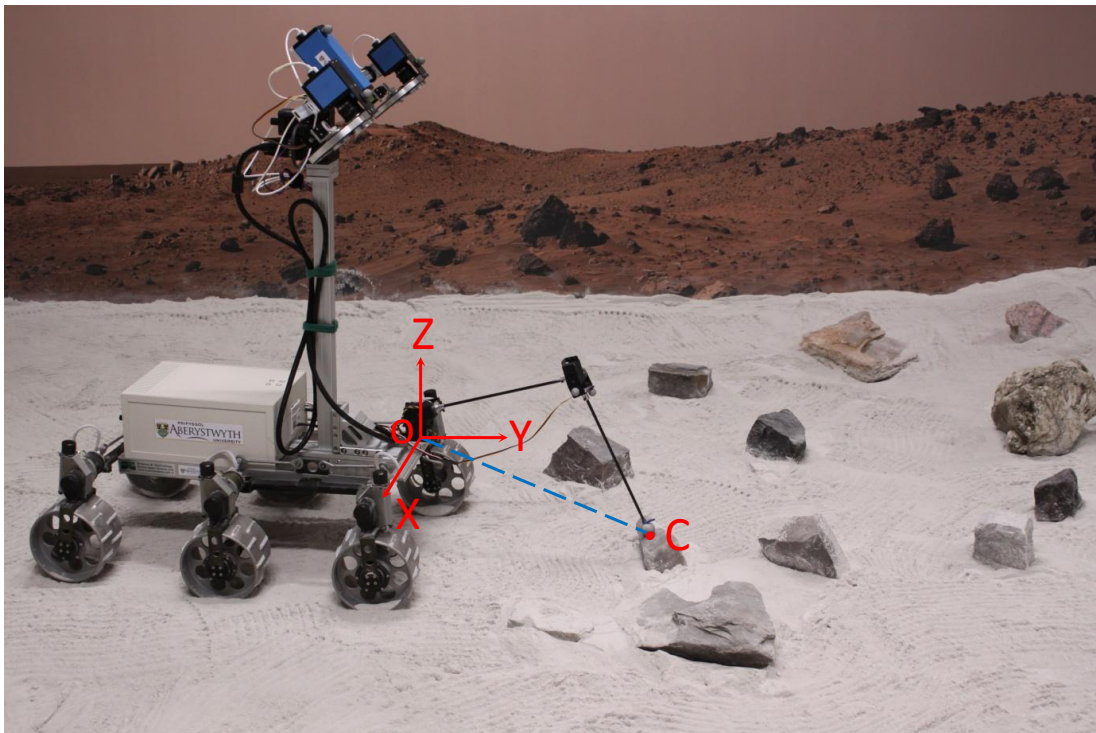


Figure 4.7: Distance between arm and object.

Table 4.2: Membership function levels for Distance.

Level No.	Near	Medium	Far	Distance(cm)
0	1	0	0	<60
1	0	0.5	0	105
2	0	1	0	145
3	0	0.5	0	185
4	0	0	1	230



Figure 4.8: Membership functions for the Distance (i_d).

4.3.2.1.3 Orientation (i_o) The orientation is the angle formed by the straight line defined relative to the heading of the rover, and the straight line that connects the projection of the centroid of the object with the reference arm (see Figure 4.9). As shown in this figure, a transparent plane is a plane that is constituted by the X and Y axes. C' is the projection of C on the transparent plane. θ is an angle between the straight line OC' and Y axis, and is the orientation. In Figure 4.10, the orientation in front of the rover is divided into six regions that are represented by the six linguistic fuzzy sets {very-bad(VB), bad(B), very-soso(VS), soso(S), good(G), very-good(VG)}. The “very-good”, “good”, “soso”, “very-soso”, “bad” and “very-bad” are sectors at $\pm 15^\circ$ (Red), between $\pm 15^\circ$ and $\pm 30^\circ$ (Turquoise), between $\pm 30^\circ$ and $\pm 45^\circ$ (Yellow), between $\pm 45^\circ$ and $\pm 60^\circ$ (Green), between $\pm 60^\circ$ and $\pm 75^\circ$ (Orange), and between $\pm 75^\circ$ and $\pm 90^\circ$ (Pink) relative to the heading of the rover, respectively. The membership functions of these sets are shown in Figure 4.11 in which “0”, “2”, “4”, “6”, “8”, “10” and “12” are corresponding to -90° , -60° , -30° , 0° , 30° , 60° and 90° , respectively.

4.3.2.1.4 Science Value (SV) (i_{SV}) The science value (SV) is a score computed from KSTIS 1.0 system between 0 and 9999, which is represented by one of

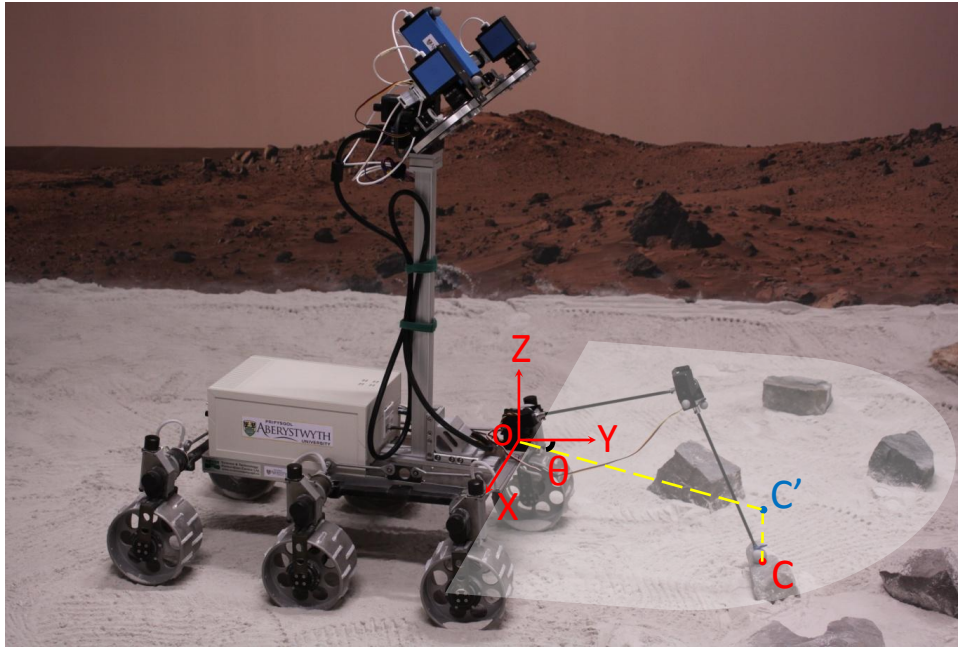


Figure 4.9: Orientation between arm and object.

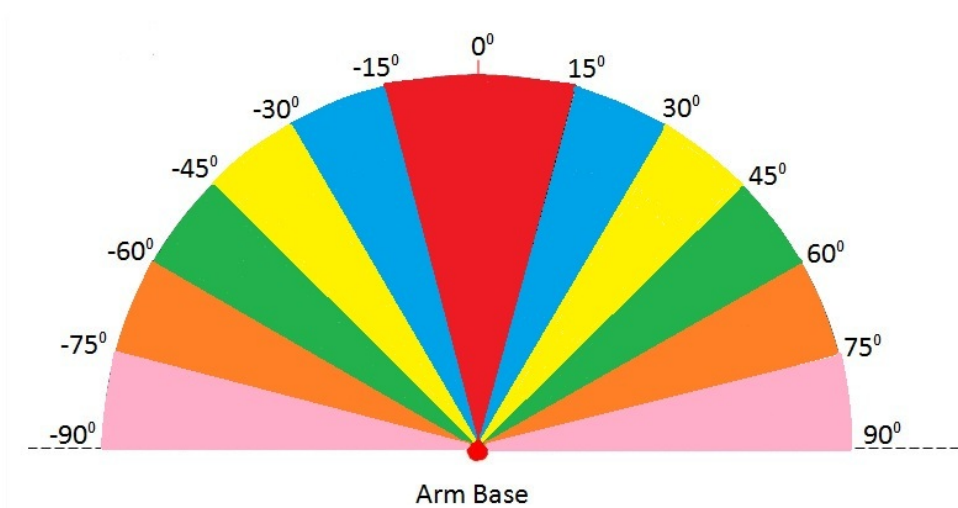


Figure 4.10: Decomposition of orientation regions.

the three linguistic fuzzy sets {LOW, MEDIUM, HIGH}, which is set up on six levels of significant science value. These levels are shown in the Table 4.3. The membership functions of these fuzzy sets are given in Figure 4.12.

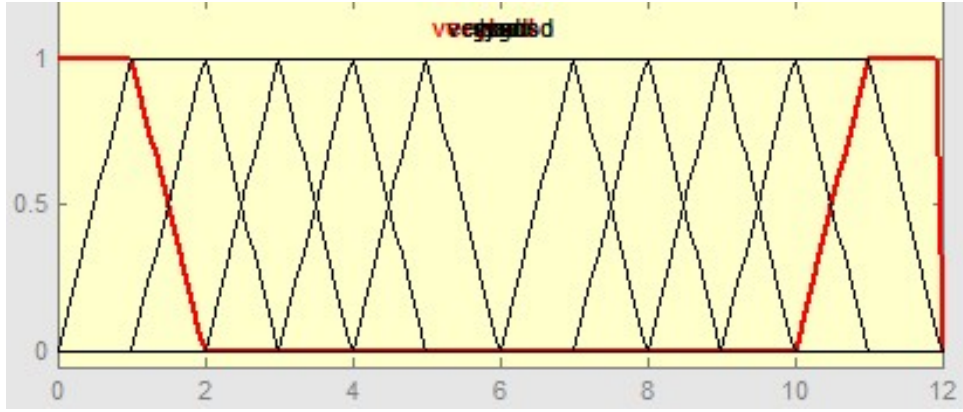


Figure 4.11: Membership functions for the Orientation (i_o).

Table 4.3: Membership function levels for SV.

Level No.	Low	Medium	High	SV Score
0	1	0	0	<20
1	0.667	0	0	40
2	0.333	0	0	60
3	0	1	0	80
4	0	0	0.5	100
5	0	0	1	>120

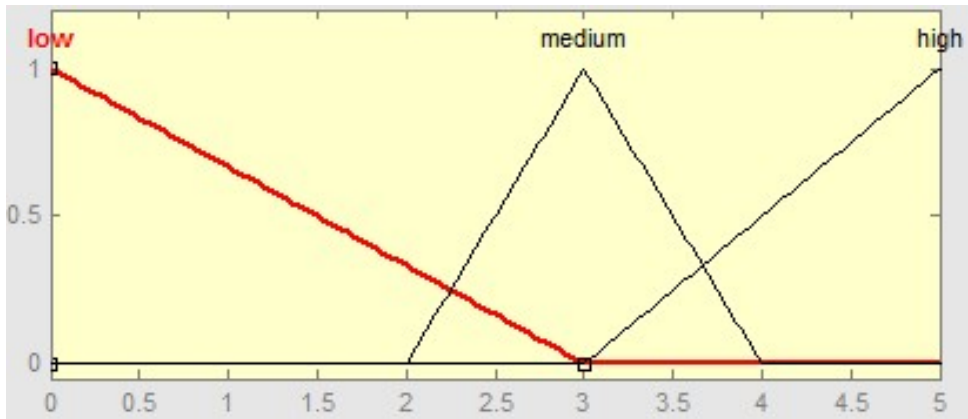


Figure 4.12: Membership functions for SV (i_{SV}).

4.3.2.2 Inference Mechanism

The inference mechanism is responsible for undertaking decision-making in the fuzzy logic controller using the fuzzy reasoning, achieving two fundamental tasks: (1) To determine the extent to which each rule is associated with the current situation as characterized by the inputs; and (2) To reach conclusions utilizing the

current inputs and the information in the rule base. Seventy-four rules are used for the proposed fuzzy controller, including the 72 rules shown in Figure 4.13 plus the two rules below. Here, an example that SV is high and Size is big is described.

- IF SV is HIGH and Size is BIG and Distance is NEAR and Orientation is VERY-BAD THEN TIndex is VERYLOW
- IF SV is HIGH and Size is BIG and Distance is NEAR and Orientation is BAD THEN TIndex is LOW
- IF SV is HIGH and Size is BIG and Distance is NEAR and Orientation is VERY-SOSO THEN TIndex is LOW
- IF SV is HIGH and Size is BIG and Distance is NEAR and Orientation is SOSO THEN TIndex is MEDIUMLOW
- IF SV is HIGH and Size is BIG and Distance is NEAR and Orientation is GOOD THEN TIndex is MEDIUMLOW
- IF SV is HIGH and Size is BIG and Distance is NEAR and Orientation is VERY-GOOD THEN TIndex is MEDIUM
- IF SV is HIGH and Size is BIG and Distance is MEDIUM and Orientation is VERY-BAD THEN TIndex is MEDIUMLOW
- IF SV is HIGH and Size is BIG and Distance is MEDIUM and Orientation is BAD THEN TIndex is MEDIUM
- IF SV is HIGH and Size is BIG and Distance is MEDIUM and Orientation is VERY-SOSO THEN TIndex is MEDIUMHIGH
- IF SV is HIGH and Size is BIG and Distance is MEDIUM and Orientation is SOSO THEN TIndex is HIGH
- IF SV is HIGH and Size is BIG and Distance is MEDIUM and Orientation is GOOD THEN TIndex is VERYHIGH
- IF SV is HIGH and Size is BIG and Distance is MEDIUM and Orientation is VERY-GOOD THEN TIndex is VERYHIGH
- IF SV is HIGH and Size is BIG and Distance is FAR and Orientation is VERY-BAD THEN TIndex is VERYLOW
- IF SV is HIGH and Size is BIG and Distance is FAR and Orientation is BAD THEN TIndex is LOW

- IF SV is HIGH and Size is BIG and Distance is FAR and Orientation is VERY-SOSO THEN TIndex is LOW
- IF SV is HIGH and Size is BIG and Distance is FAR and Orientation is SOSO THEN TIndex is MEDIUMLOW
- IF SV is HIGH and Size is BIG and Distance is FAR and Orientation is GOOD THEN TIndex is MEDIUMLOW
- IF SV is HIGH and Size is BIG and Distance is FAR and Orientation is VERY-GOOD THEN TIndex is MEDIUM

- IF Size is SMALL THEN TIndex is VERYLOW
- IF SV is LOW THEN TIndex is VERYLOW

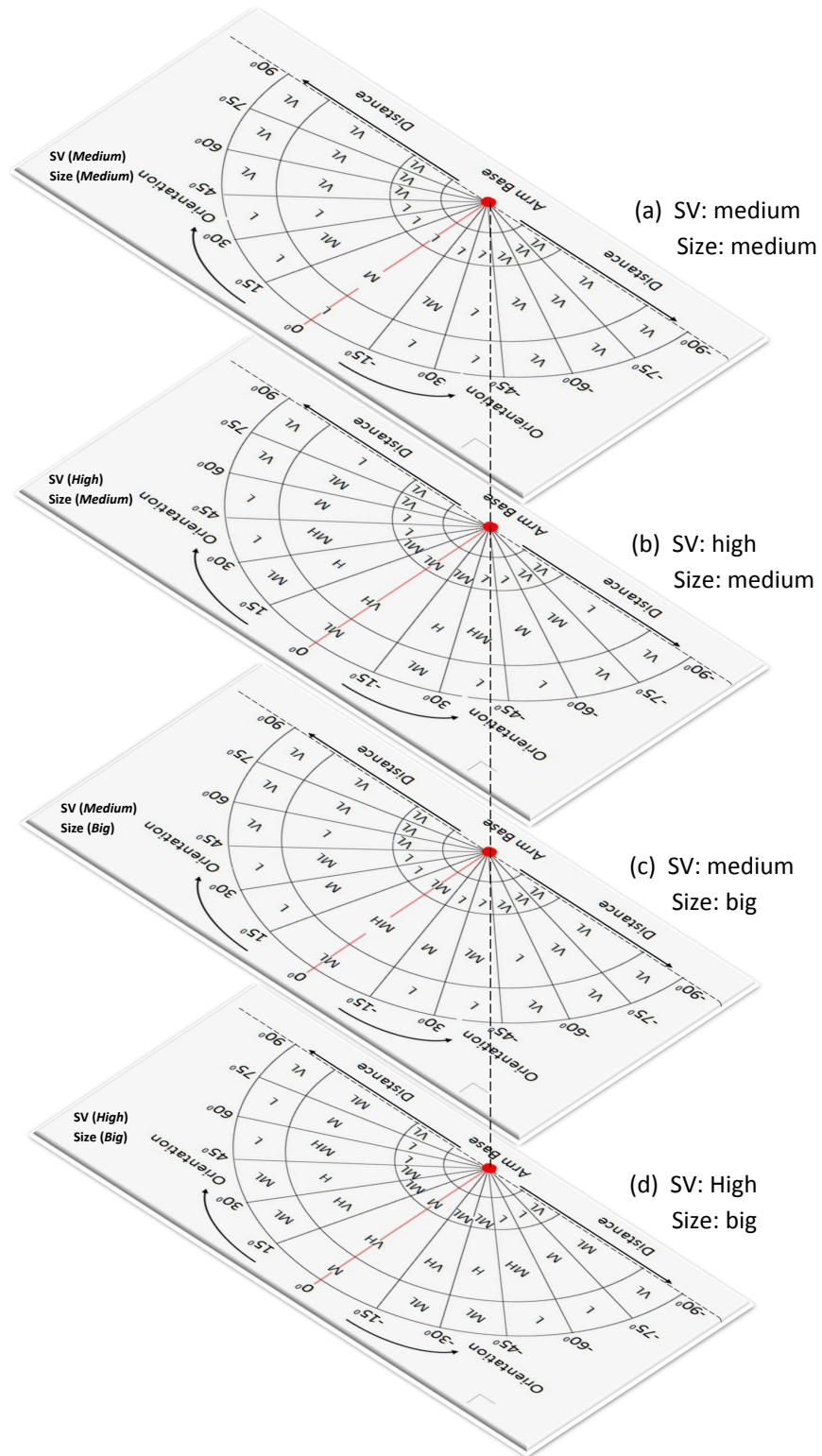


Figure 4.13: Rule base for touchability (VL-VeryLow, L-Low, ML-MediumLow, M-Medium, MH-MediumHigh, H-High, VH-VeryHigh).

4.3.2.3 Defuzzification

The output of the fuzzy controller from the inference mechanism is mapped to a crisp value called *Touchability Index* by the defuzzification procedure. There are a number of methods that can be used to implement the defuzzification, that transforms the conclusion of the inference mechanism into the subsequent output. Therefore defuzzification process is the opposite of the fuzzification process. In particular the “COG defuzzification” is used that combines the output represented by the implied fuzzy sets from all rules to calculate the gravity centroid of the possible distribution into a control action. The *Touchability Index* is represented by the seven linguistic fuzzy sets {VERYLOW, LOW, MEDIUMLOW, MEDIUM, MEDIUMHIGH, HIGH, VERYHIGH}. The membership functions of these sets are shown in Figure 4.14, where the horizontal axis is the Touchability Index and the corresponding relative to the actual output is 0: 0%; 1: 10%; 2: 20%...9 : 90%; 10 : 100%.

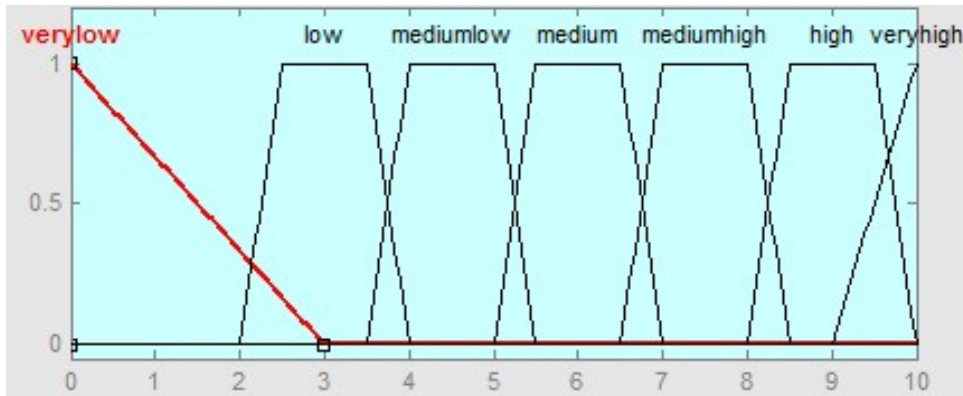


Figure 4.14: Membership functions for Touchability Index (o_t).

4.4 Simulation Results and Analysis

In the following simulation experiments a data set has been constructed to validate the fuzzy controller designed, and to work out the *Touchability Index* of the mock objects which are ranked by the *Touchability Index*. The results are compared with the manual rank by a human expert.

The fuzzy logic-based controller is specified by defining fuzzy variables, fuzzy membership functions and rules utilizing the MATLAB Fuzzy ToolBox simulator.

Nine rocks have been constructed, in which three kinds of the rock are used, i.e., small (10×15), medium (20×15) and big (30×20). The three science value scores used are 35, 65 and 105. In Table 4.4, $Length \times Width$ is the size of the goal.

Table 4.4: Simulation experiment data.

Rock No.	Length	Width	SV	Orientation	Distance
1	10	15	105	12	132
2	10	15	65	-65	166
3	10	15	35	50	111
4	20	15	105	-17	161
5	20	15	65	-33	126
6	20	15	35	72	151
7	30	20	105	5	148
8	30	20	65	32	167
9	30	20	35	-46	112

In order to better illustrate rock ranking based on the science values (SV), a colour coded table is designed where SV is represented by distinct colors (see Table 4.5).

Table 4.5: Correspondence between SV and colour.








Corresponding Colour	SV Scores
Cyan(c) 	<20
Green(g) 	20-39
Blue(b) 	40-59
Yellow(y) 	60-79
Magenta(m) 	80-99
Red(r) 	100-119
Black(k) 	>120

Figure 4.15 shows the resulting rock ranking. The centre of the frame is the arm base, the SV is represented by color, and the size of the rock is depicted by the diameter of the color circle. It demonstrates that the touchability sequence of these rocks can be intuitively ranked as shown in Table 4.6. In this table the numbers of the column $TIndex$ are generated by running the designed fuzzy controller in MATLAB, and the column $TRank$ is a rank that is produced by the magnitude sequence of $TIndex$. These results demonstrate the validity of the proposed approach, comparing perfectly with the ranking given by the human expert.

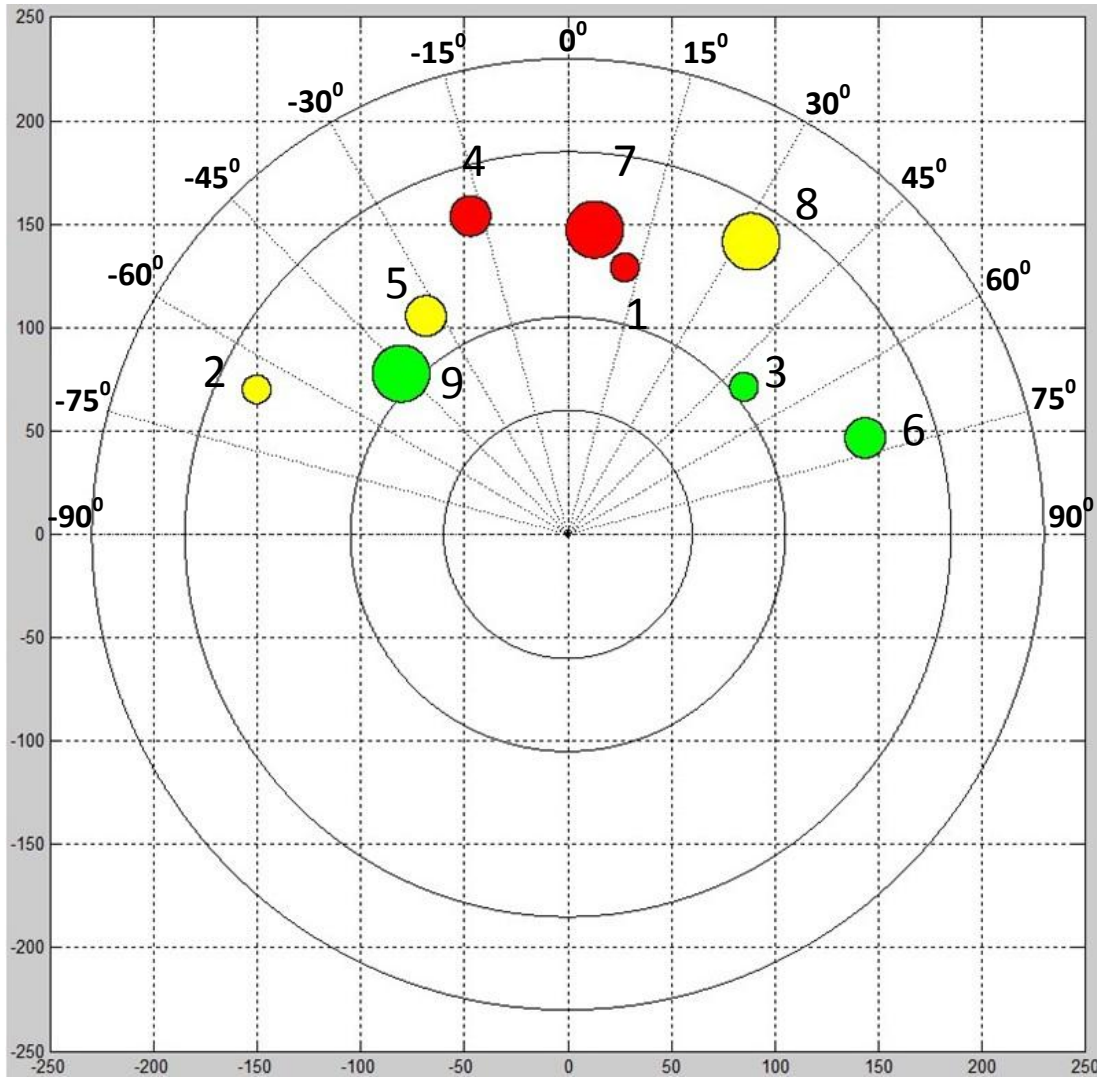


Figure 4.15: Simulated experiment environment.

4.5 Summary

The use of fuzzy logic control has two major benefits for the touchability system. First, the fuzzy rules are employed to emulate human experience for the acquisition of an object, which is readily intuitive and understandable. Second, because it is inevitable that the quality of the data for the SV and Size in measuring and interpreting is inaccurate, the tolerance of fuzzy logic to imprecision and uncertainty in sensor data is of particular appeal.

In this chapter, a fuzzy logic-based controller for the touchability of the science targets has been presented. The membership functions and fuzzy rules have been

Table 4.6: Simulation experiment result.

RockNO.	Artificial Rank	TIndex(%)	TRank
1	5	35.2	5
2	7	23.8	7
3	8	22.3	8
4	2	88.4	2
5	4	54.1	4
6	9	18.4	9
7	1	96.6	1
8	3	67.5	3
9	6	34.9	6

devised and the defuzzification mechanism identified. The simulation experimentation has shown the validity of the proposed system.

Chapter 5

Experimentation of the Touchability System

The simulation experiment environment is implemented here with respect to the proposed method for ranking the touchability of science targets that was presented in the preceding chapter. In particular, real rocks and data are employed to test and verify the validity of the fuzzy logic-based controller built for the touchability of the science objects through hardware implementation. In the experiment all images taken are segmented manually, but the measurement method described in chapter 3 is used to determine the size of each rock. The evaluation given by the domain expert is used as the ground truth in this study. The experimental results show that the designed fuzzy controller system has achieved the domain expert's performance.⁶

5.1 Experimental Platform

The experimental platform that is used to perform this set of experiments was built in the AU Intelligent System Laboratory (ISL) at Aberystwyth University. It mainly includes a robotic arm, two wide-angle cameras (WACs), a camera mast and optical bench (see Figure 5.1). In this section the experimental equipment used in order to run all experiments will be described.

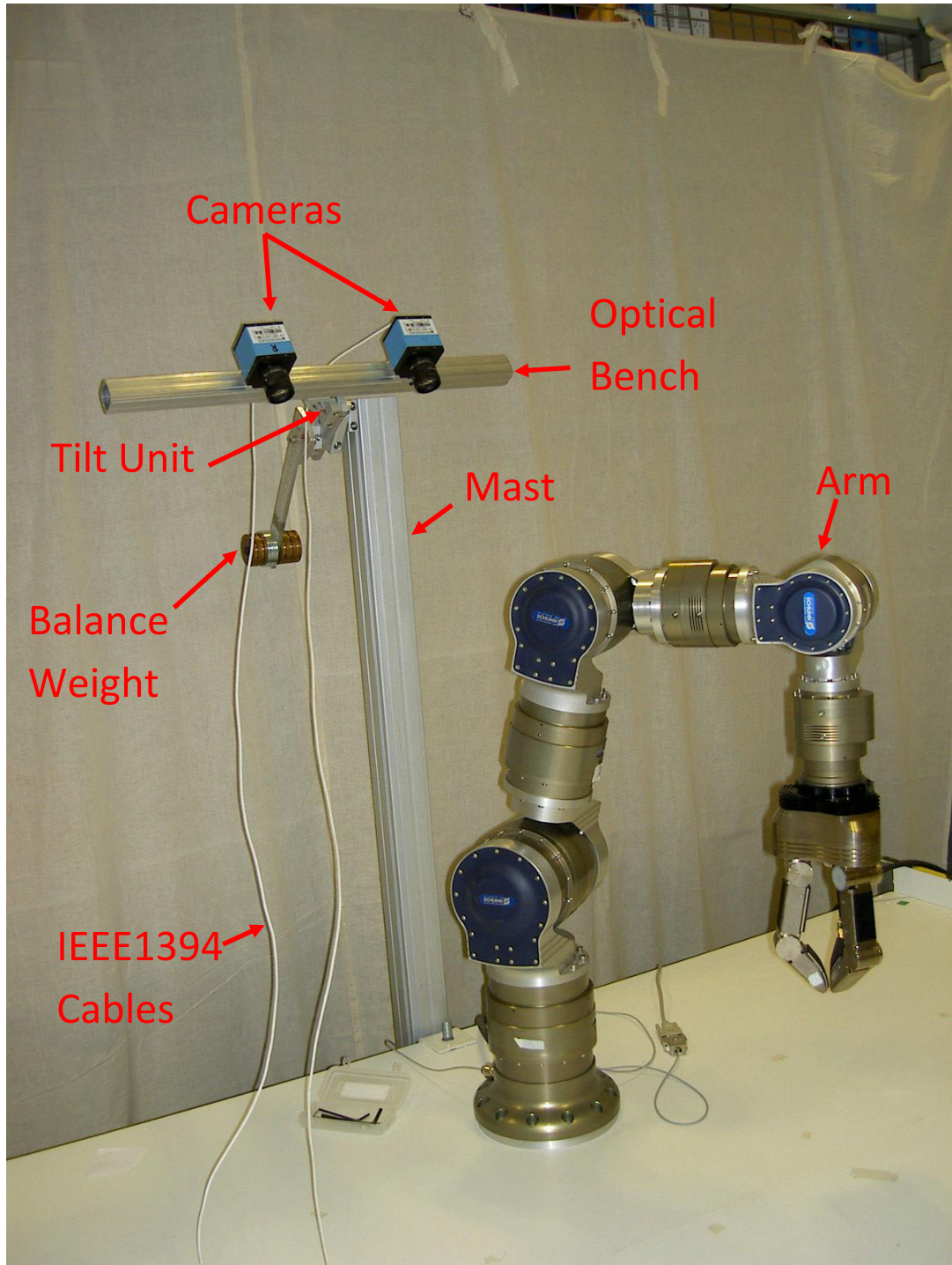


Figure 5.1: Experimental platform

5.1.1 Cameras

The two wide-angle cameras (WACs) are IEEE1394 (FireWire) monochrome cameras made by The Imaging Source Ltd. The cameras each has 1024×768 pixel

resolution and panchromatic sensors without infra-red filters, i.e., their spectral range extends infra-red. This makes them ideal for use with filter wheels (multispectral filters are not involved in the present work). The lenses used have an 8mm focal length which gives an overall horizontal field of view of approximately 35° , and also has lockable focus and iris rings, which are generally desirable for the WACs. Further details of the camera and lens specifications are shown in Table 5.1.

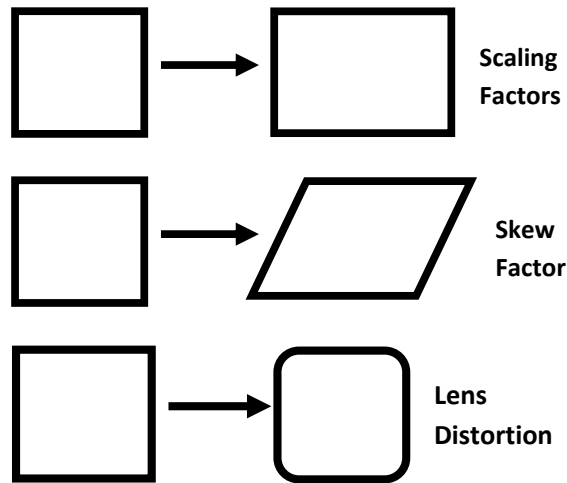
Table 5.1: WACs specifications.

Resolution	1024×768
Pixel Size	$4.65\mu m$
Sensor Size	4.76×3.57
Lens	Computar M0814-MP
Focal Length	8 mm
Field of View	$35^\circ \times 25^\circ$
Frame Rate	3.75 - 30 fps
Shutter	1/10000 - 30 s

5.1.1.1 Camera Calibration

Camera calibration is a necessary step in 3D computer vision in order to extract metric information from 2D images. Currently, according to the different objects used for calibration there are a number of techniques that may be employed to achieve this work. Here 2D plane based calibration technique is used (Heikkila & Silven, 1997), as the work requires the observation of planar patterns shown at a few different orientations. Because almost anyone can make such a calibration pattern by oneself, the setup is easy. In stereo vision two cameras are needed generally. Therefore, the camera calibration requires not only the intrinsic and extrinsic camera parameters, but also the relative position between the two cameras. These parameters are summarized below:

- Position of the image center in an image. Note that this typically not at (width/2, height/2) of the image.
- Focal length.
- Different scaling factors for row pixels and column pixels.
- Skew factor.



- Lens distortion.
- Relative position of the two camera.

The Matlab tool box is used to perform the computation involved in the camera calibration. The calibration involves 14 pairs of corresponding left and right images. The results of camera calibration are shown as follows.

- Intrinsic parameters of left camera:
 - Focal Length: $fc_left = [1780.75603 \ 1781.65210] \pm [8.96685 \ 8.55379]$
 - Principal point: $cc_left = [451.58289 \ 370.04071] \pm [15.92816 \ 15.23360]$
 - Skew: $alpha_c_left = [0.00000] \pm [0.00000] \Rightarrow$ angle of pixel axes = 90.00000 ± 0.00000 degrees
 - Distortion: $kc_left = [-0.07750 \ 0.09062 \ -0.00443 \ -0.00501 \ 0.00000] \pm [0.04188 \ 0.27946 \ 0.00213 \ 0.00350 \ 0.00000]$
- Intrinsic parameters of right camera:
 - Focal Length: $fc_right = [1780.49925 \ 1783.21577] \pm [8.85186 \ 8.67202]$
 - Principal point: $cc_right = [449.69618 \ 334.96230] \pm [14.69461 \ 17.98229]$
 - Skew: $alpha_c_right = [0.00000] \pm [0.00000] \Rightarrow$ angle of pixel axes = 90.00000 ± 0.00000 degrees
 - Distortion: $kc_right = [-0.06579 \ -0.16427 \ -0.00632 \ -0.00852 \ 0.00000] \pm [0.05927 \ 0.83789 \ 0.00314 \ 0.00257 \ 0.00000]$

- Extrinsic parameters (position of the right camera with respect to the left camera):

Rotation vector: $\text{om} = [-0.00362 \ 0.06867 \ -0.00043] \pm [0.01120 \ 0.01124 \ 0.00112]$

Translation vector: $\text{T} = [-199.37136 \ -0.64008 \ 13.00476] \pm [0.73220 \ 0.46330 \ 3.95160]$

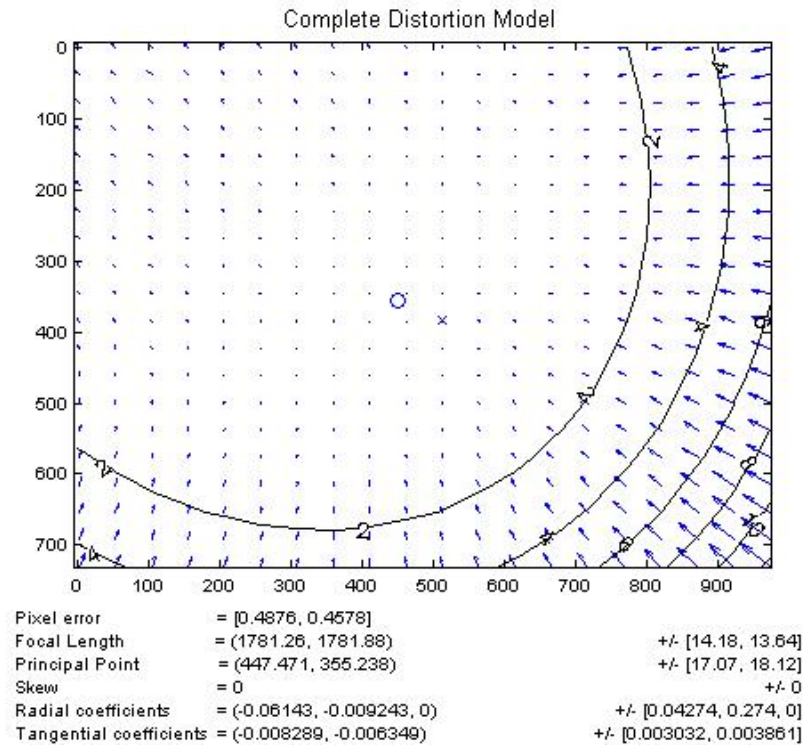
In order to make a decision on choosing an appropriate distortion model to use, it is useful to visualize the effect of distortions on a given image. Figure 5.2 shows the impact of a complete distortion model (radial + tangential) on each pixel of the image, with each arrow representing the effective displacement of a pixel induced by the lens distortion. Observe that points at the corners of the image are displaced by as much as 12 pixels in the distortion model of the right camera.

5.1.2 Optical Bench

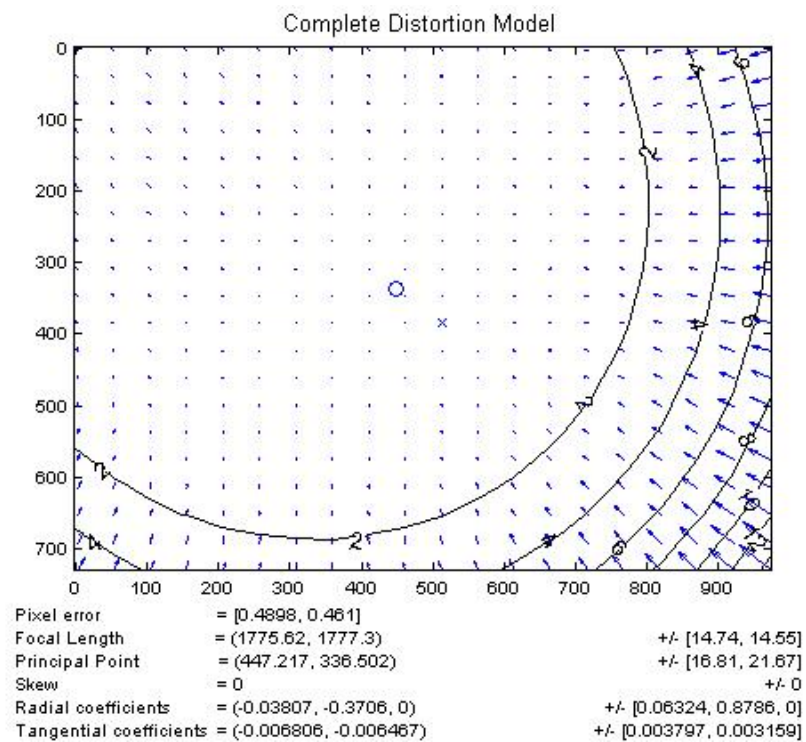
The optical bench used for the experiments is shown in Figure 5.1. It is constructed with lightweight aluminium optical rail and sliders. The rail and sliders have an interlocking double-sided dovetail design that allows the cameras to be moved and locked in the required position. The cameras are connected to the optical bench by custom adapter plates with sliders. The cameras can be mounted anywhere along the rail, with the two cameras situated with a baseline separation of 200mm.

5.1.3 Schunk Arm

The Schunk arm (shown in Fig. 5.3) is developed and manufactured by SCHUNK GmbH & Co. KG. It is based on the servo-electric swivel units PRL combined with ERB jointed modules that contain integrated motor controller units, and a through-hole for cable feed-through. The combination of a high compact performance, and new materials for the connection technology allow the doubling of the payload to nominal 10 kg. The standard design of the arm is available as a 7 degrees of freedom system. In particular, the open software architecture allows for the connection and operation of any type of modules at the servo-electric wrist of the arm. The Schunk Dextrous Hand is set up in the end of the arm as an end effector, a 3-fingered gripper with 7 DOF and tactile feedback sensors in the fingers.



(a)



(b)

Figure 5.2: (a) The distortion model of the left camera. (b) The distortion model of the right camera.

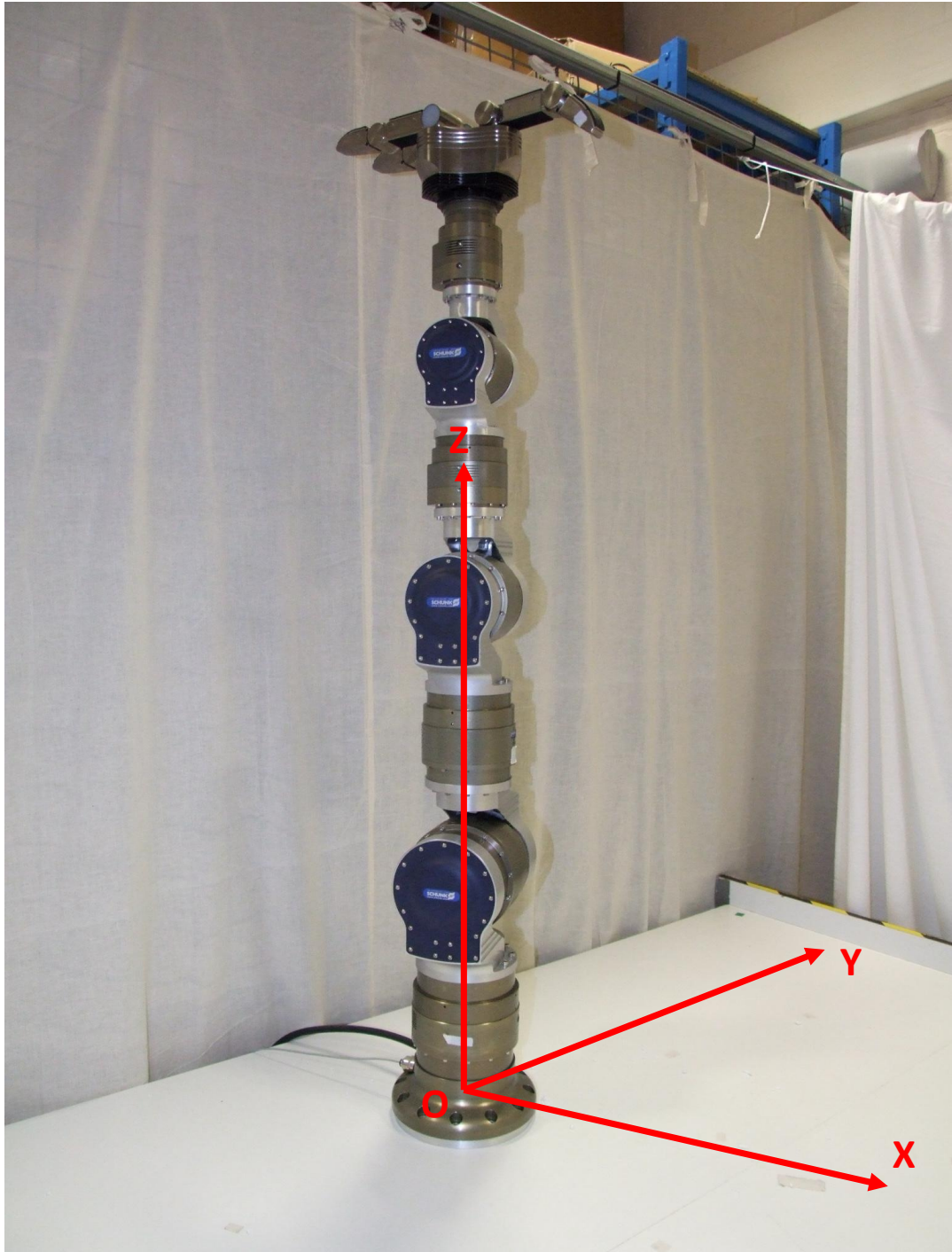


Figure 5.3: Schunk Arm: all the joints are at home base.

The joints of the Schunk arm are constituted by seven Powercube units. From the base joint to the end joint, all joints are orderly named as J_1 , J_2 , J_3 , J_4 , J_5 , J_6 and J_7 , respectively. The Powercube units are numbered with #3, #4, #5, #6, #7, #8 and #9 because of the default setting of the manufacturers. Every

joint is allowed to operate in a range between -2 rad and 2 rad . The directions of the rotation of the seven joints are shown in Fig. 5.4, where “+” is the positive direction and “-” is the negative direction.

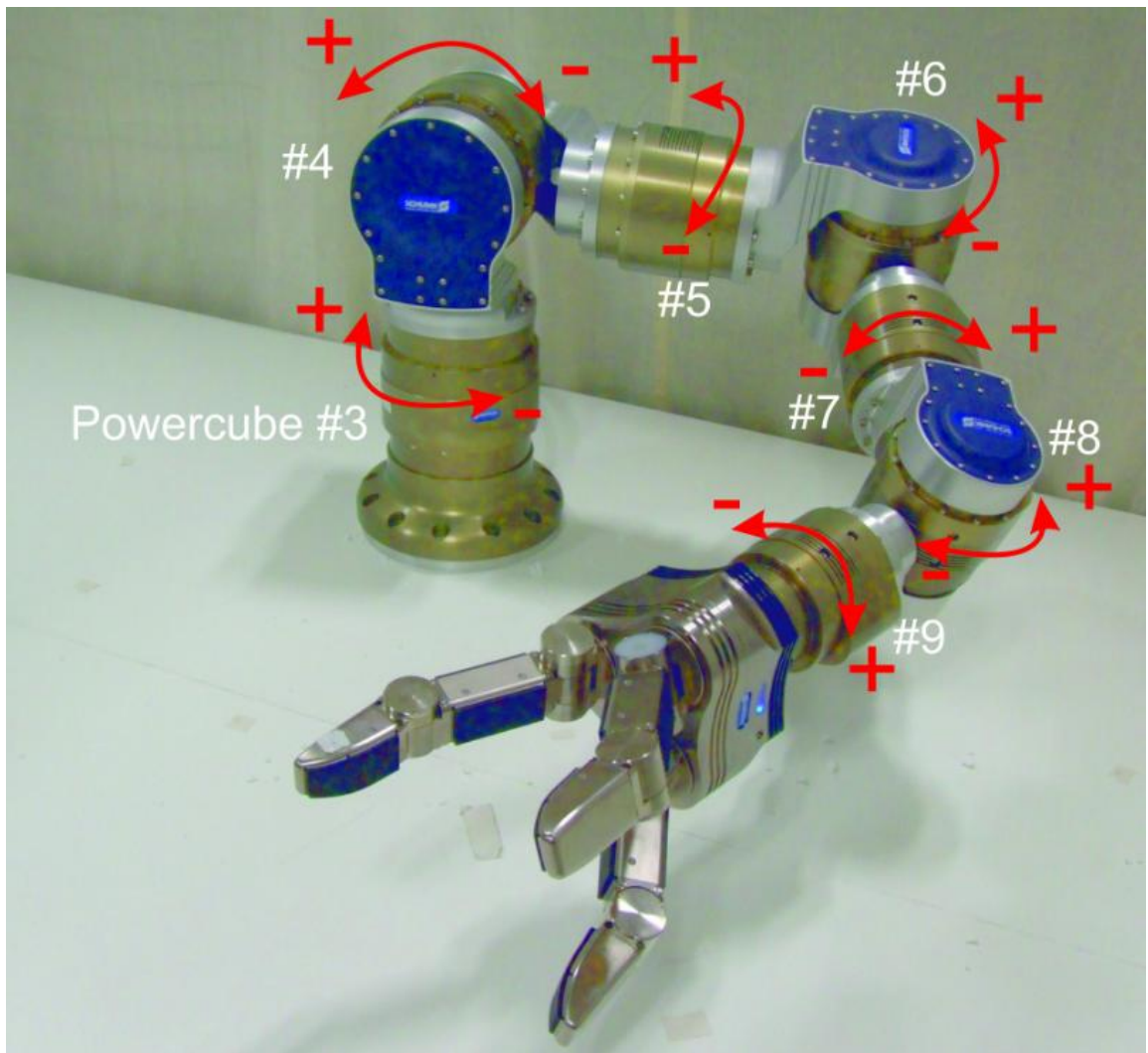


Figure 5.4: Directions of the rotation of the seven joints.

5.1.3.1 Object Location

In robotics, it is important to keep track of an object’s location as it is moving within in 3D space. The workspace is always referenced to a fixed world frame, and all objects within the workspace are positioned with respect to the fixed reference frame by the use of three coordinate numbers (x, y, z) . However, the position of an object as described by its three coordinates possesses only half of

the information regarding the location of the object. The orientation of the object is also important and requires a mathematical description as well. That is the location of an object consists of the object position and orientation:

$$\textit{Location} = \textit{Position and Orientaion}$$

Thus, a reference frame is attached to each input at object location such that knowing where the object frame is located, i.e., knowing both the frame's position and orientation, will unambiguously determine where all points of the object are located.

5.1.3.2 Translations

A translation is a geometric transform that moves an object from one position to another without modifying the object's orientation. A translation moves every point on the object by the same vector \mathbf{u} involving three positional parameters.

Finally, if a point Q , given by its coordinates vector $\mathbf{q} = \begin{bmatrix} x_q \\ y_q \\ z_q \end{bmatrix}$ is translated by

a translation T of vector $\mathbf{u} = \begin{bmatrix} a \\ b \\ c \end{bmatrix}$ denoted $T_{\mathbf{u}}$, the translated point Q' is then

given by the coordinate vector \mathbf{q}' such that

$$\mathbf{q}' = \mathbf{q} + \mathbf{u} = \begin{bmatrix} x_q + a \\ y_q + b \\ z_q + c \end{bmatrix}$$

A translation can also be represented as a homogeneous transform matrix as follows:

$$\mathbf{q}' = T_{\mathbf{u}}\mathbf{q} = \begin{bmatrix} 1 & 0 & 0 & a \\ 0 & 1 & 0 & b \\ 0 & 0 & 1 & c \\ 0 & 0 & 0 & 1 \end{bmatrix} \begin{bmatrix} x_q \\ y_q \\ z_q \\ 1 \end{bmatrix} = \begin{bmatrix} x_q + a \\ y_q + b \\ z_q + c \\ 1 \end{bmatrix}$$

Since translations have no effect on orientation, the 3×3 rotation submatrix of the homogeneous translation transform matrix $T_{\mathbf{u}}$ is an identity matrix.

5.1.3.3 Rotations

Rotation transforms are associated with an axis of rotation, typically designated by a vector $\mathbf{v} = \begin{bmatrix} x_v \\ y_v \\ z_v \end{bmatrix}$ and a fixed angle of rotation θ . If a point Q, with coordinates $\mathbf{q} = \begin{bmatrix} x_q \\ y_q \\ z_q \end{bmatrix}$, is rotated around \mathbf{v} by an angle θ to a point Q' , then the coordinate vector \mathbf{q}' of Q' is determined by

$$\mathbf{q}' = \mathbf{R}_{v,\theta}\mathbf{q}$$

$$\mathbf{R}_{v,\theta} = \begin{bmatrix} \cos\theta + (1 - \cos\theta)x_v^2 & (1 - \cos\theta)x_v y_v - (\sin\theta)z_v & (1 - \cos\theta)x_v z_v + (\sin\theta)y_v \\ (1 - \cos\theta)y_v x_v + (\sin\theta)z_v & \cos\theta + (1 - \cos\theta)y_v^2 & (1 - \cos\theta)y_v z_v - (\sin\theta)x_v \\ (1 - \cos\theta)z_v x_v - (\sin\theta)y_v & (1 - \cos\theta)z_v y_v + (\sin\theta)x_v & \cos\theta + (1 - \cos\theta)z_v^2 \end{bmatrix}$$

where $\mathbf{R}_{v,\theta}$ represents the rotation matrix. To obtain an expression for the matrix $\mathbf{R}_{v,\theta}$, it is convenient to start with rotations around the reference frame axes, referred to as canonical rotations.

5.1.3.4 Forward Kinematics

Forward kinematics is concerned with the computation of the position and orientation of a robot's end effector as a function of its joint variables which are known. In order to compute the end effector pose given a set of joint variable values, the robot manipulator Denavit-Hartenberg (DH) parameters are needed. These parameters result from a set of reference frames, O_0, O_1, \dots, O_n (for an n -joint robot), attached to the robot links. Each link frame is fully described by its pose matrix with respect to the preceding link frame along the robotic chain. In general, a frame O_i is described with respect to O_{i-1} by its pose matrix as determined here:

$$A = \begin{bmatrix} c_i & -\gamma_i s_i & \sigma_i s_i & a_i c_i \\ s_i & \gamma_i c_i & -\sigma_i c_i & a_i s_i \\ 0 & \sigma_i & \gamma_i & d_i \\ 0 & 0 & 0 & 1 \end{bmatrix}$$

where $c_i = \cos(\theta_i)$, $s_i = \sin(\theta_i)$, $\gamma_i = \cos(\alpha_i)$, and $\sigma_i = \sin(\alpha_i)$. θ_i and α_i is DH parameters.

A sequence of pose matrices, which are each themselves a homogeneous frame transforms, are used in the forward kinematics process to compute the pose matrix \mathbf{P} of the end effector frame O_n with respect to the base frame of the robot O_0 . It is often useful to write the homogeneous frame transform in the following partitioned form:

$$\mathbf{A}_i = \begin{bmatrix} \mathbf{R}_i & \mathbf{p}_i \\ 000 & 1 \end{bmatrix}$$

where

$$\mathbf{R}_i = \begin{bmatrix} c_i & -\gamma_i s_i & \sigma_i s_i \\ s_i & \gamma_i c_i & -\sigma_i c_i \\ 0 & \sigma_i & \gamma_i \end{bmatrix}$$

$$\mathbf{p}_i = \begin{bmatrix} a_i c_i \\ a_i s_i \\ d_i \end{bmatrix}$$

The objective of the forward kinematics is to compute the pose \mathbf{P} of the end effector with respect to the base frame. With the present link frame assignment, the frame attached to the end effector is simply O_n . The end effector pose matrix \mathbf{P} for an n -joint robot manipulator is then given by

$$\mathbf{P} = \mathbf{A}_1 \mathbf{A}_2 \dots \mathbf{A}_{n-1} \mathbf{A}_n$$

From the above, for any set of joint variables, there can be only one possible end effector pose matrix. Therefore, the forward kinematics problem has at most one solution.

with respect to the Schunk arm all seven DOF are used in the forward kinematics. The Denavit-Hartenberg method (DH) was introduced to simplify this progress. According to the positive direction of each joint, the DH coordinate frames of all joints can be established as illustrated in Figure 5.5. From this the DH parameters can be obtained, with the resulting parameter for each joint shown in Table 5.2. In particular, the parameter θ is the variable which represents the rotation angle of each joint. The parameters d_1 , d_2 , d_3 and d_4 donate the link lengths of the Schunk arm. On the basis of manufacturer data these are measured to be: $d_1 =$

31.33cm, $d_2 = 33.41\text{cm}$, $d_3 = 28.1\text{cm}$ and $d_4 = 43.72\text{cm}$.

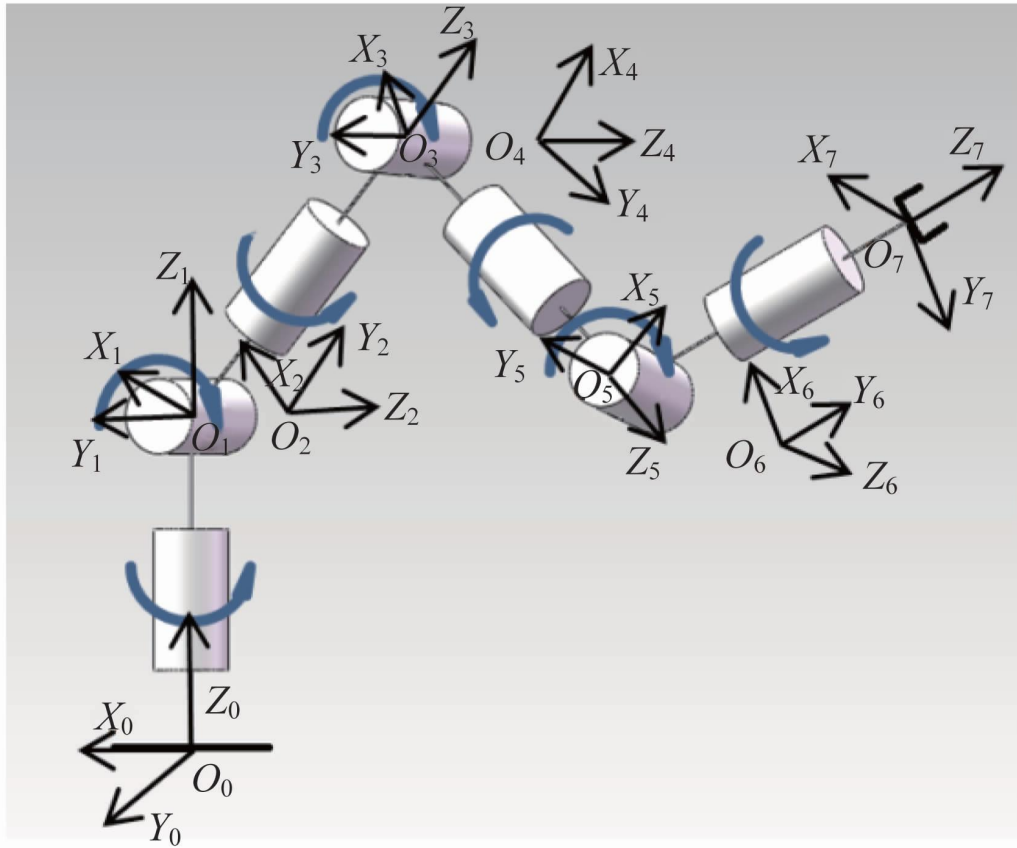


Figure 5.5: D-H frames of the Schunk arm.

5.1.3.5 Inverse Kinematics

The above forward kinematics addresses the problem of finding for the end effector pose of a robot manipulator from a complete set of joint variables. The inverse kinematics problem however, is to find one or more sets of joint values from a given end effector pose. A complete set of joint values is called a configuration in joint space. For a robot manipulator with n joints, a complete set of joint values is an $n \times 1$ vector $\mathbf{p} = [q_1 \ q_2 \ \dots \ q_n]$, where $q_i = \theta_i$ if joint i is revolute and $q_i = d_i$ if joint i is prismatic.

The inverse position kinematics is central to the control of robot manipulators. Indeed, in general, the desired Cartesian location of the robot end effector, the pose matrix, is usually known from the task specifications, but each robot joint

Table 5.2: D-H parameters of the Schunk arm.

	link twist (α_i)	link length (a_i)	link offset (d_i)	link angle (θ_i)
J_1	0	0	d_1	θ_1
J_2	90°	0	0	θ_2
J_3	-90°	0	d_2	θ_3
J_4	90°	0	0	θ_4
J_5	-90°	0	d_3	θ_5
J_6	90°	0	0	θ_6
J_7	-90°	0	d_4	θ_7

is individually controlled. Each joint position must therefore be known in order to obtain the necessary robot motion that achieves the desired end effector pose. When addressing an inverse kinematics problem, as there may be different DH parameters to incorporate, no fixed solution exists.

Considering the purpose of the present experimentation is to check whether the objects are in the range of acquisition, many joints are not needed. Here, joints J_3 , J_5 and J_7 are locked (the rotation angles are fixed as 0°), shortening number of the arm's DOF to four for the Schunk arm. Inverse kinematics for a four DOF manipulator is computed as follows.

Without losing generality, suppose that the coordinates of the end point are (P_x, P_y, P_z) in the arm base frame, that A, B, C and D are the link lengths of the arm, and that $\theta_1, \theta_2, \theta_3$ and θ_4 are the solving targets of inverse kinematics with θ_4 fixed to be $\pi/6$ (shown in Figure 5.6).

In this general case, it can be seen that the rotation angle θ_1 can be simply resolved as below (see Figure 5.7):

$$\theta_1 = \arctan(P_y/P_x) \quad (5.1)$$

The procedure to obtain the angles θ_2, θ_3 are calculated in the plane ZR (see Figure 5.8), such that

$$SP = \sqrt{P_x^2 + P_y^2 + (A - P_z)^2} \quad (5.2)$$

$$EP = \sqrt{C^2 + D^2 + 2 \times C \times D \times \cos(\theta_4)} \quad (5.3)$$

$$\gamma = \arccos(B^2 + SP^2 - EP^2 / 2 \times B \times SP) \quad (5.4)$$

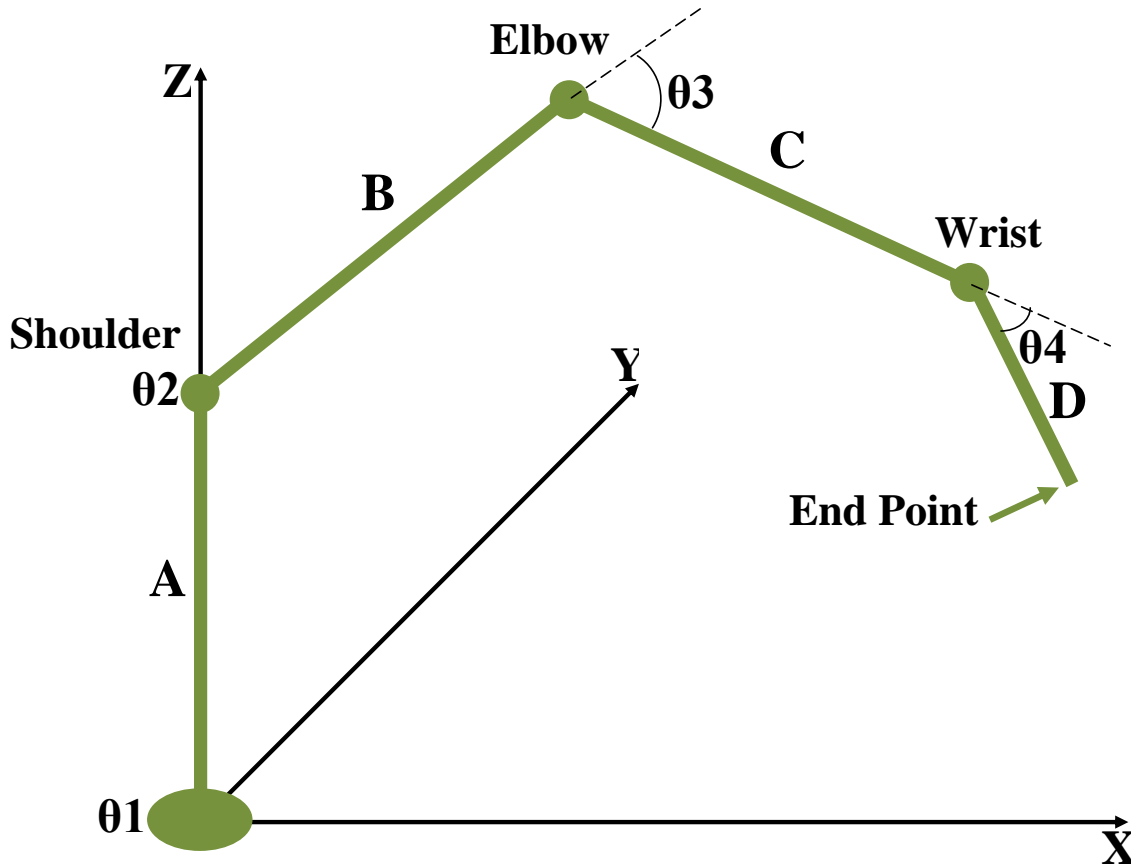


Figure 5.6: Inverse kinematics for a four DOF manipulator.

$$\alpha = \arccos[(A - P_z)/SP] \quad (5.5)$$

$$\theta_2 = \pi - \alpha - \gamma \quad (5.6)$$

$$\beta = \arccos[B^2 + EP^2 - SP^2/2 \times B \times EP] \quad (5.7)$$

$$\delta = \arccos[C^2 + EP^2 - D^2/2 \times C \times EP] \quad (5.8)$$

$$\theta_3 = \pi - \beta - \delta \quad (5.9)$$

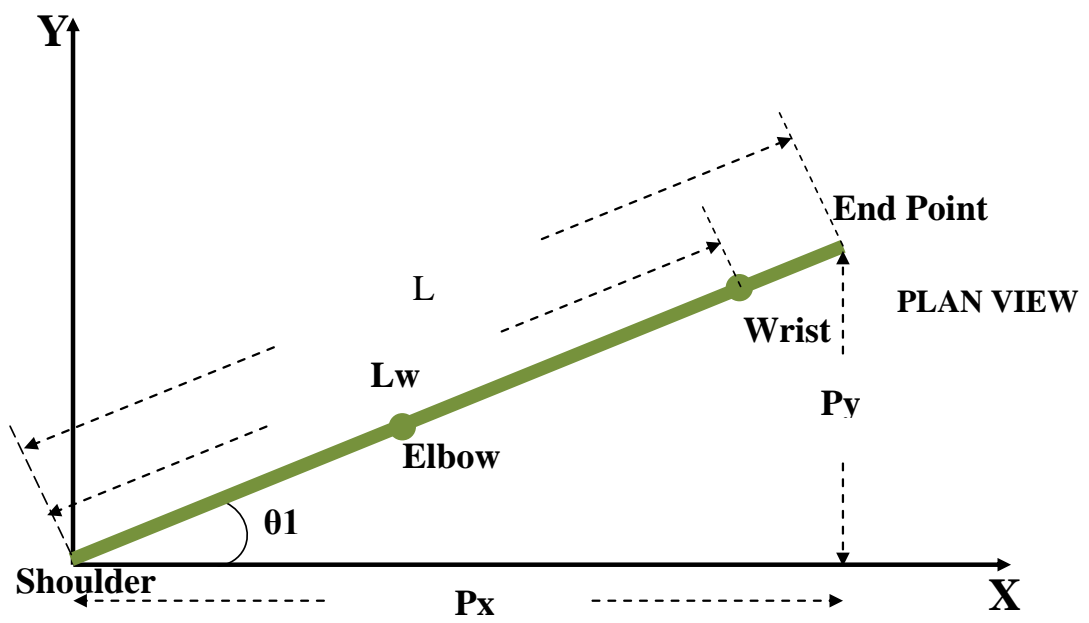


Figure 5.7: Plan View (seen from the z axis) of the four DOF manipulator.

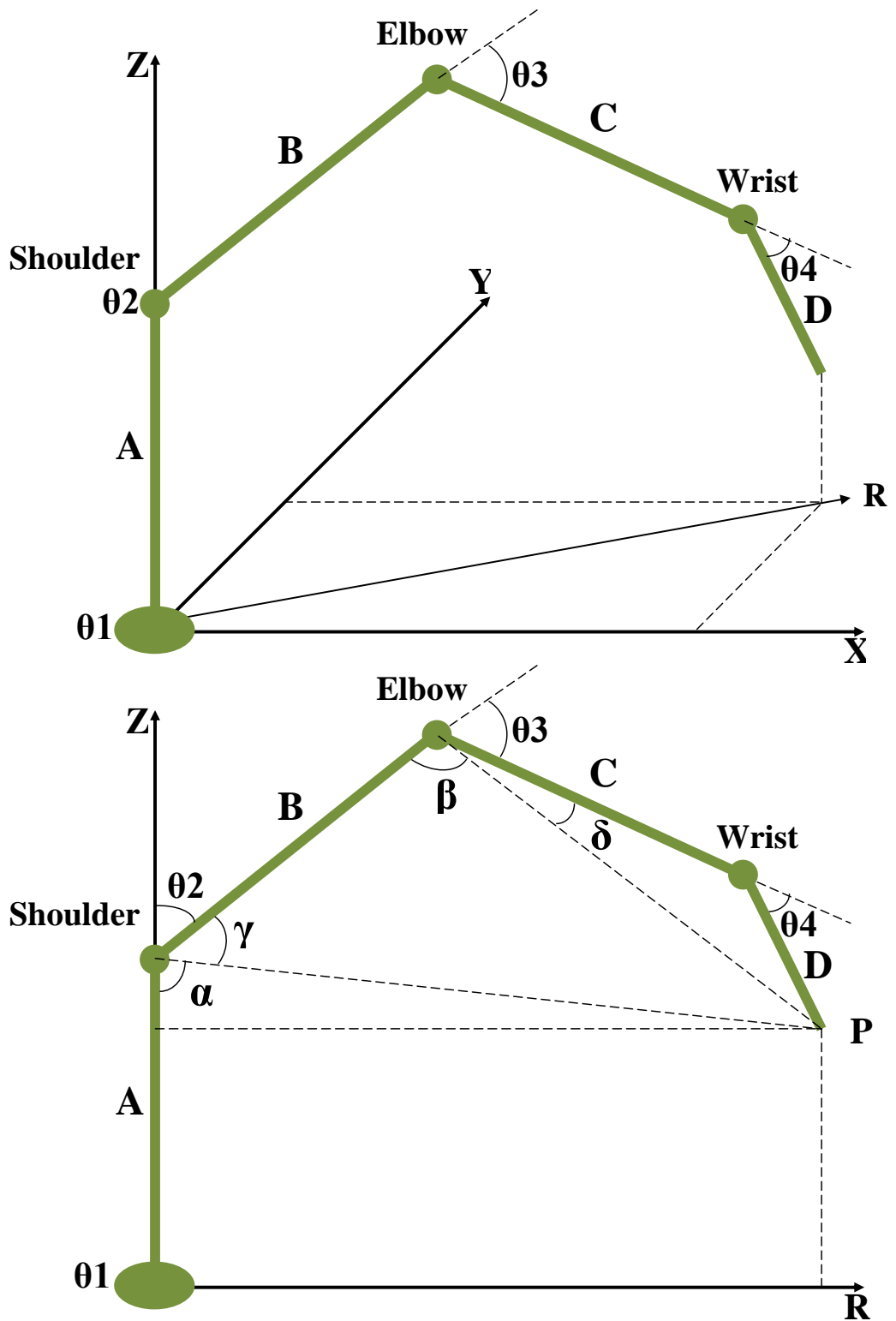


Figure 5.8: ZR plane for the procedure of computing θ_2 and θ_3 .

5.2 Experimental Results

A total of 9 rocks of a different size and shape have been used to test the touchability of rocks. Within the 9 rocks there are 3 small, 3 medium and 3 big ones, involving three kinds of scientific value (Low, Medium and high) for each type of rock (Small, Medium and Big) (see Figure 5.9). Because of the limit of the pan angle (Pan 0°) the two cameras are set at a -40° tilt angle to capture the initial image. Therefore, the overlap vision range of the two cameras is approximately between -30° and 30° , corresponding to the Good and Very Good orientation (see Chapter 4).

As the touchability of Mars scientific targets by a Martian robotic arm has been at the present done by human experts on Earth, the comparison is therefore only compared to the results by a human expert available to this research. In this section results of seven experiments are reported based on the location of the aforementioned 9 rocks (Near, Medium and Far). The rock detection software (see Chapter 3) is not used during these experiments as not all the images used are suitable for the algorithm. The images captured in all experiments are manually segmented and labeled. The purpose of these experiments is to test the viability of the Touchability system. The experimental results are discussed with respect to the input by the domain expert (Dr Derek Pullan of the University of Leicester). Only one expert view is adopted here as the footing for comparison, owing to the rarity of the specialists in this application domain. The evaluation from the domain expert for all experiments is that the Touchability Index should be at least 80%, and the domain expert provided the science value of each rock. The externally given parameters are used throughout the following experiment.

5.2.1 Experiment 1

In Figure 5.10 the four rocks used for this experiment. Rock 1 is a big rock, and has a high science value; its distance to the robot hand is medium. There is a low scientific value for the small Rock 2 with a medium distance. A high science value and a medium distance are assumed for the small Rock 3. Small rock 4 possesses a medium scientific value and is of a near distance to be robot hand. The evaluation of the touchability given by the domain expert for these four rocks is that all rocks are not touchable, except for Rock 1. Figure 5.10 shows the result produced by

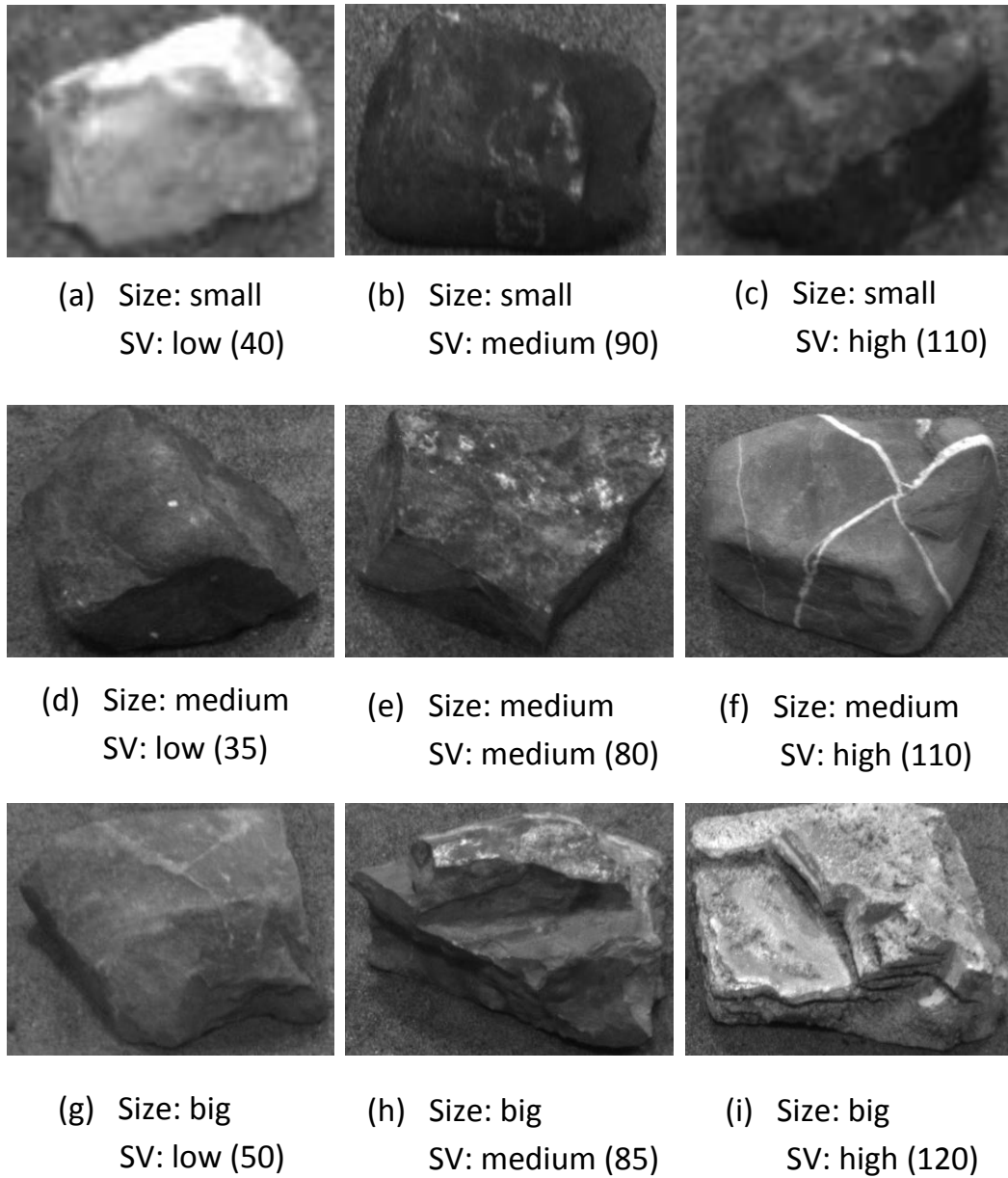


Figure 5.9: Rocks used for experiment.

the Schunk arm. The Touchability Index and the relevant measurement computed are showed in Table 5.3.

5.2.2 Experiment 2

Figure 5.11 shows the four rocks that are used for experiment 2. Rock 1 is a big rock, and has a high science value with a near distance. There is a high scientific

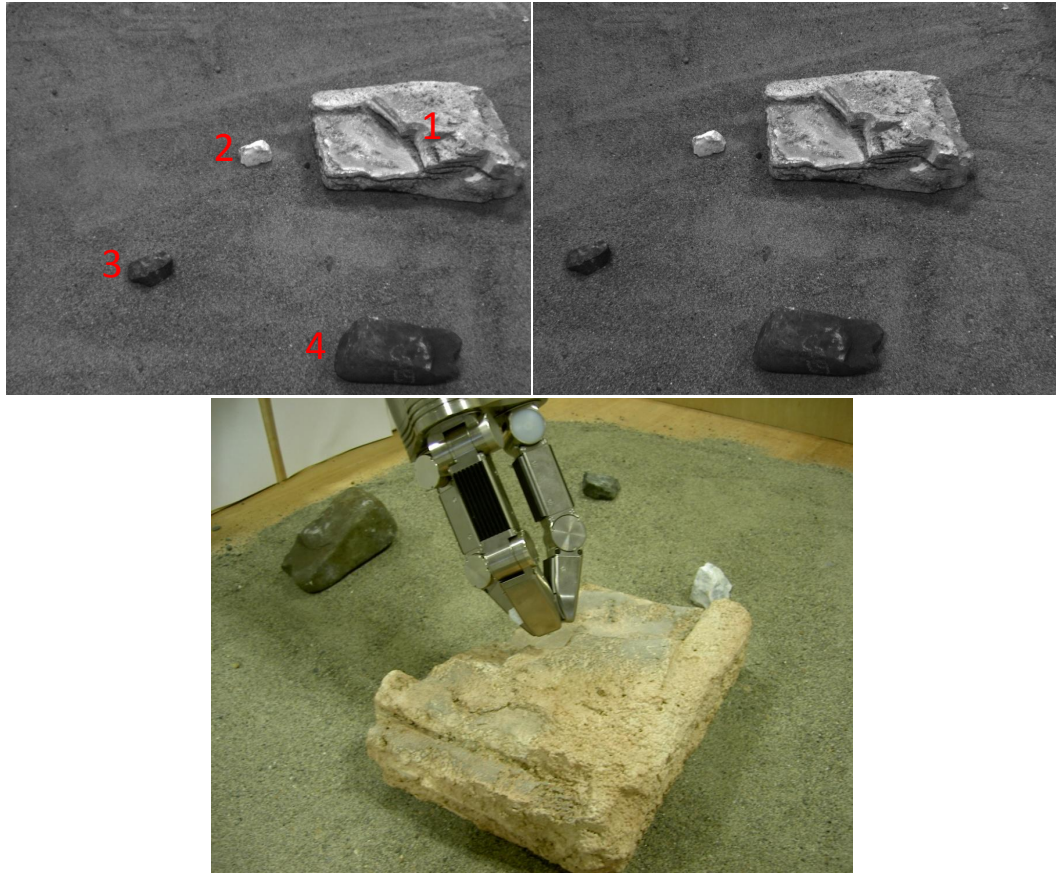


Figure 5.10: Top left image: this image was captured by the left camera. Top right image: this image was captured by the right camera. Bottom image: this image was the result of touchability computation.

Table 5.3: Results from experiment 1.

Rock No.	Size (cm^2)	Orientation	Distance (cm)	Science Value	Touchability Index
1	737.86	18°	76.4	120	92.5%
2	26.33	-6°	75.3	40	9.76%
3	24.4	-25°	52.7	100	9.75%
4	109.46	20°	37.6	90	21.6%

value in the medium Rock 2 that is of a medium distance to the robot hand. A low science value and a far distance are assumed for the medium Rock 3. Small rock 4 possesses a low scientific value and is of a far distance. The evaluation of the touchability given by the domain expert for the four rocks is that all rocks are not touchable, except for Rock 2. Figure 5.11 shows the operational result produced by the Schunk arm. The results of Touchability Index and the relevant

measurements computed are showed in Table 5.4.

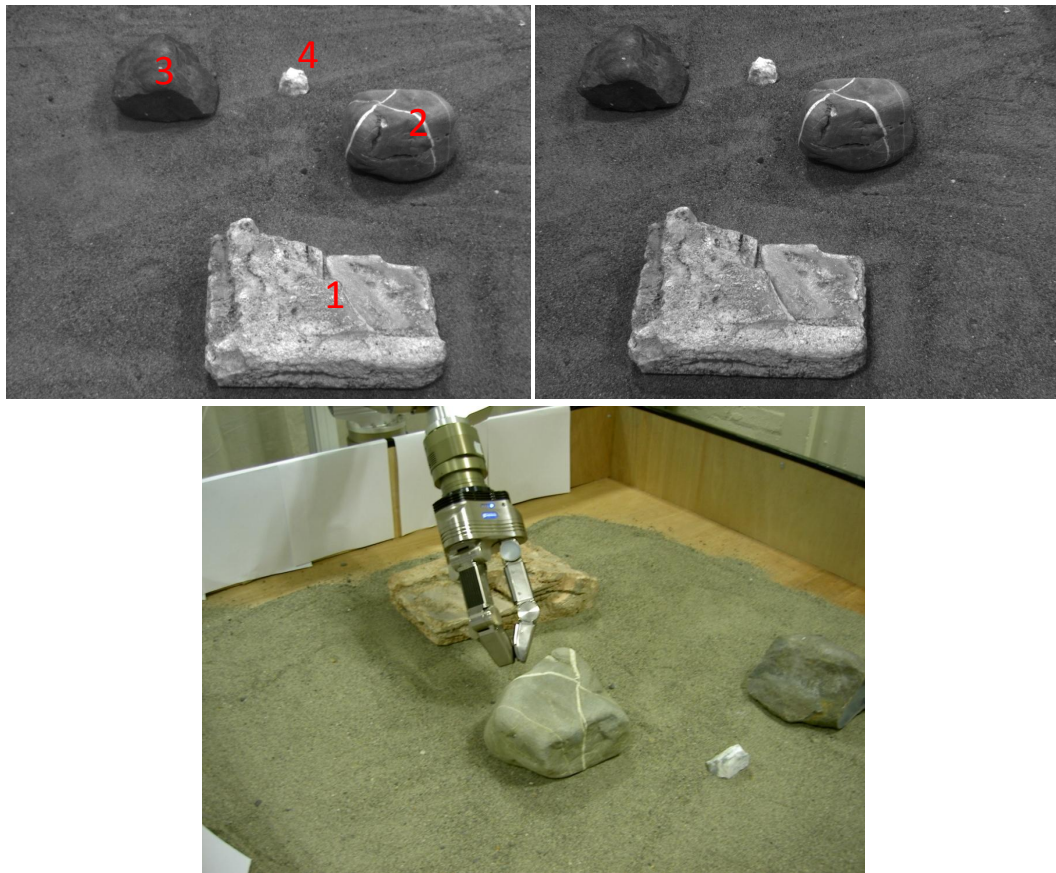


Figure 5.11: Top left image: this image was captured by the left camera. Top right image: this image was captured by the right camera. Bottom image: this image was the result of touchability computation.

Table 5.4: Results from experiment 2.

Rock No.	Size (cm^2)	Orientation	Distance (cm)	Science Value	Touchability Index
1	715.72	3°	32.7	120	58.2%
2	308.01	16°	65.2	110	89.9%
3	291.66	-23°	82.3	35	10.2%
4	27.03	4°	84.5	40	9.8%

5.2.3 Experiment 3

In Figure 5.12 the four rocks are used for experiment 3. Rock 1 is a big rock, and has a medium science value and is far from the robot hand. The medium Rock 2 is of a medium scientific value and a near distance. A low science value and a medium distance are assumed for the medium Rock 3. Small rock 4 possesses a medium scientific value and is of a far distance. The evaluation of the touchability given by the domain expert for the four rocks is that all rocks are not touchable. The Touchability Index and the relevant results computed are showed in Table 5.5.

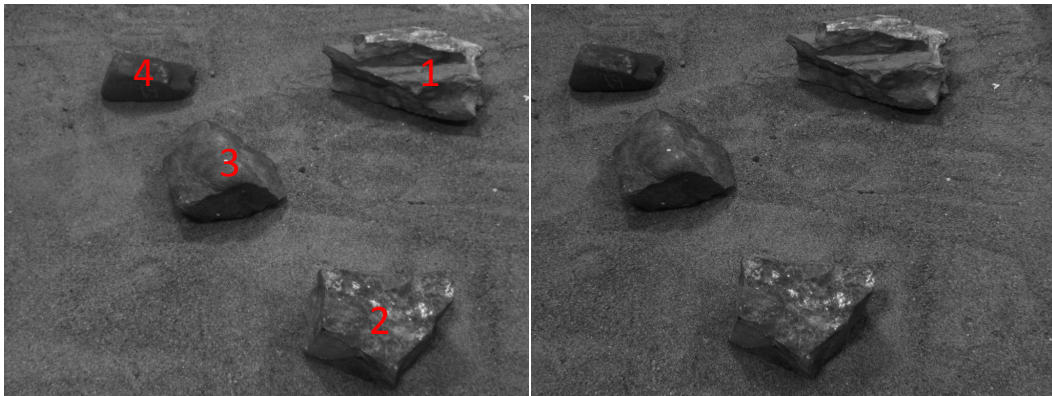


Figure 5.12: Left image: this image was captured by the left camera. Right image: this image was captured by the right camera.

Table 5.5: Results from experiment 3.

Rock No.	Size (cm^2)	Orientation	Distance (cm)	Science Value	Touchability Index
1	564.93	21°	83.6	85	61.8%
2	329.62	24°	34.2	80	52.3%
3	349.23	-11°	62.1	35	10.2%
4	145.15	-19°	84.1	90	40.2%

5.2.4 Experiment 4

Figure 5.13 shows the four rocks that are used for experiment 4. Rock 1 is a big rock, and has a medium science value and is of a medium distance to the robot hand. There is a low scientific value for the big Rock 2 which is of a far distance. A high science value and a near distance are assumed for the medium Rock 3. Small

rock 4 possesses a high scientific value and is of a far distance. The evaluation of the touchability given by the domain expert for these four rocks is that all rocks are not touchable, except for Rock 1. Figure 5.13 shows the operational result produced by The Schunk arm. The resulting of Touchability Index and other measurements are showed in Table 5.6.

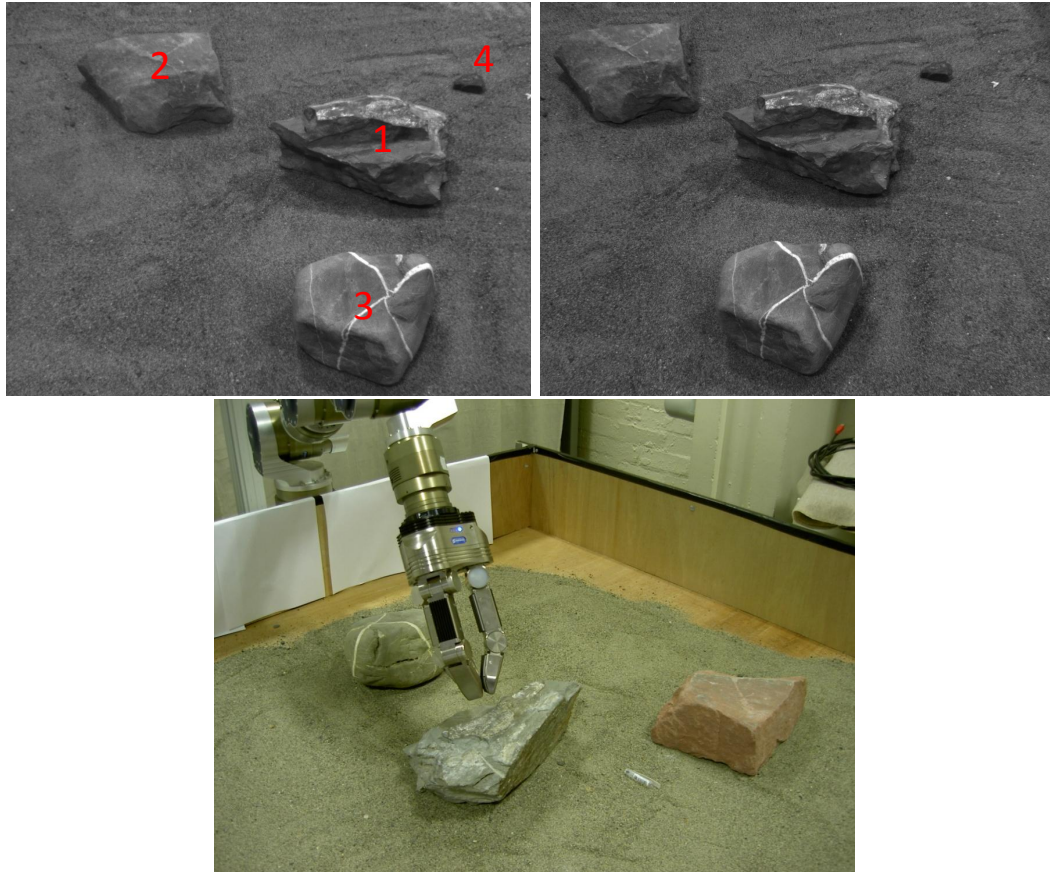


Figure 5.13: Top left image: this image was captured by the left camera. Top right image: this image was captured by the right camera. Bottom image: this image was the result of touchability computation.

Table 5.6: Results from experiment 4.

Rock No.	Size (cm^2)	Orientation	Distance (cm)	Science Value	Touchability Index
1	561.57	12°	59.6	85	85.6%
2	552.08	-12°	86.7	50	11.4%
3	331.09	13°	34.3	110	60.8%
4	24.4	24°	87.3	100	9.8%

5.2.5 Experiment 5

In Figure 5.14 the four rocks that are used in this experiment are shown. Rock 1 is a big rock, and has a medium science value and is of a near the distance to the robot hand. The big rock 2 is of a low scientific value and a medium distance. A high science value and a far distance are assumed for the medium Rock 3. Small rock 4 possesses a low scientific value and is of a near distance. The evaluation of the touchability given by the domain expert for the four rocks is that all rocks are not touchable. The results of Touchability Index and relevant measurements computed are showed in Table 5.7.

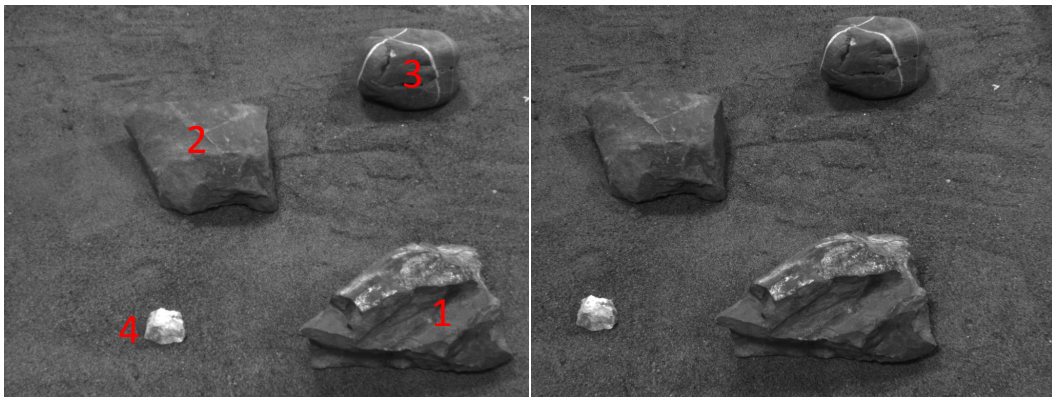


Figure 5.14: Left image: this image was captured by the left camera. Right image: this image was captured by the right camera.

Table 5.7: Results from experiment 5.

Rock No.	Size (cm^2)	Orientation	Distance (cm)	Science Value	Touchability Index
1	520.3	26°	33.1	85	49.7%
2	290.57	-8°	62.8	50	11.4%
3	496.46	17°	84.7	110	62.5%
4	26.23	-26°	33.7	40	9.7%

5.2.6 Experiment 6

Figure 5.15 shows the four rocks that are used in this experiment 6. Rock 1 is a big rock, and has a high science value and is of a far the distance to the robot hand. There is a medium scientific value in the medium Rock 2 which is of a medium distance to the robot hand. A low science value and a near distance are assumed

for the medium Rock 3. Small rock 4 possesses a high scientific value and is of a near distance. The evaluation of the touchability given by the domain expert for these four rocks is that all rocks are not touchable, except for Rock 2. Figure 5.15 shows the operational result produced by The Schunk arm. The results of Touchability Index and the relevant measurements are showed in Table 5.8.

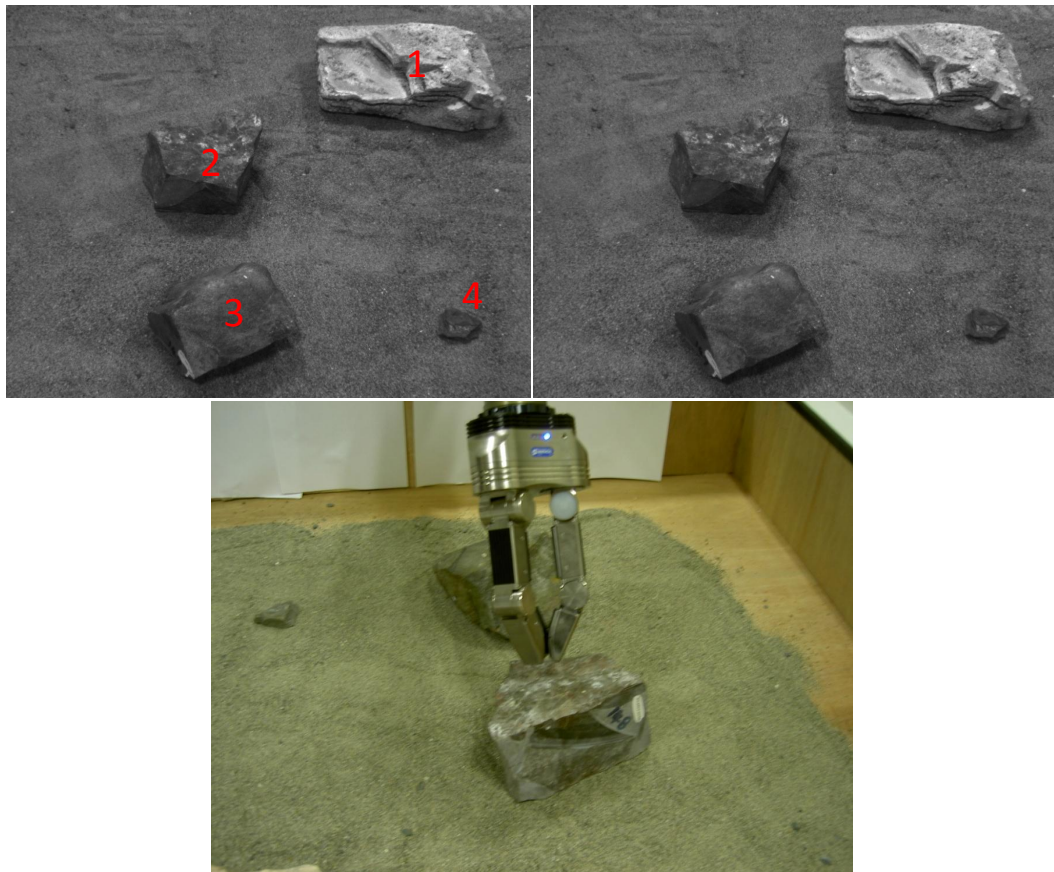


Figure 5.15: Top left image: this image was captured by the left camera. Top right image: this image was captured by the right camera. Bottom image: this image was the result of touchability.

Table 5.8: Results from experiment 6.

Rock No.	Size (cm^2)	Orientation	Distance (cm)	Science Value	Touchability Index
1	717.62	15°	87.7	120	54.9%
2	307.67	-16°	62.4	80	82.1%
3	370.85	-18°	31.8	35	10.2%
4	23.82	28°	32.5	100	9.6%

5.2.7 Experiment 7

In Figure 5.16 the three rocks that are used in this experiment are shown. Rock 1 is a big rock, and has a low science value and is of a near distance to the robot hand. A medium scientific value and a far distance are assumed for the medium Rock 2, and a medium science value and a medium distance for the small Rock 3. The evaluation of the touchability given by the domain expert for the three rocks is that all rocks are not touchable. The results of Touchability Index and other measurements computed are showed in Table 5.9.

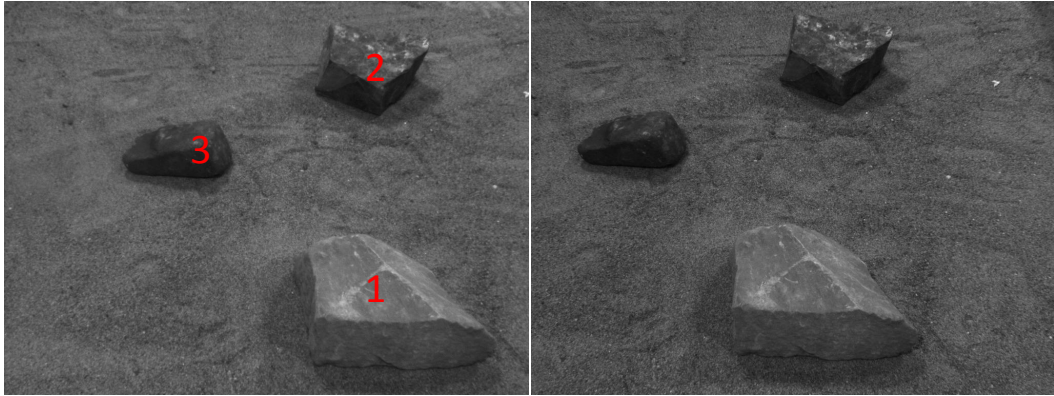


Figure 5.16: Left image: this image was captured by the left camera. Right image: this image was captured by the right camera.

Table 5.9: Results from experiment 7.

Rock No.	Size (cm^2)	Orientation	Distance (cm)	Science Value	Touchability Index
1	490.55	17°	35.1	50	11.4%
2	329.01	10°	64.3	80	11.5%
3	141.83	-15°	83.7	90	40.6%

5.3 Discussion of Results

The Touchability Index value , 80% that is generated by the domain expert is used as the threshold in the above experiment. Thus a positive result is achieved if the Touchability Index over a certain rock is greater than 80%. In experiment one only the Touchability Index over rock 1 (92.5%) is greater than 80%. This means that instrument deployment can reach out for rock 1 but not for the others. Based

on the evaluation of the touchability given by the domain expert only rock 1 can be touched. Therefore the experimental result matched well with the evaluation of domain expert.

In experiment two the Touchability Index over all rocks is less than 80%, so no instrument deployment is possible for any rocks. The evaluation of the touchability given by the domain expert is the same. Thus, the experimental result is consistent with the evaluation of the domain expert. This result applies to experiments three, five and seven also, although different rocks and different numbers of rocks are involved.

In experiment four only the Touchability Index over rock 1 (85.6%) is greater than 80%, implying that instrument deployment can reach out for rock 1. The evaluation of the touchability given by the domain expert is the same, only rock 1 can be touched. Accordingly the experimental result is in accordance with the evaluation of domain expert. Similar results are achieved for experiment six, where only the Touchability Index over rock 1 (82.1%) is greater than the given threshold of 80%. Thus, the instrument deployment can reach out for rock 2. This matches with the evaluation of the touchability over these rocks by the domain expert.

Summarizing the above experiments and discussion, it is clear that the evaluation outcome of the domain expert has perfectly matched with that obtained by the present work. This means that the Touchability System designed herein has achieved the experience and knowledge level of the domain expert.

5.4 Summary

In this chapter the results of the touchability system experimentation have been presented. The experimental hardware platform is built, including: two wide-angle cameras (WACs), Schunk arm, real rocks, camera mast and optical bench. The results of seven independent experiments have been discussed involving different locations of a subset of 9 rocks which have different sizes and science values. The experimental results show that the touchability system designed is able to attain the performance of a domain expert.

Chapter 6

Conclusions

This chapter summarizes and concludes the investigations conducted in this thesis, including a list of the main contributions together with a list of publications produced within this project. It also presents a brief discussion about the future directions of research in order to improve the current work.

6.1 Summary of the Work

Limited opportunity to explore remote planetary surfaces and the substantial cost of each of such exploration have led to an increase in the demand for higher levels of autonomy than that permitted by the exploration platforms currently available (Huntsberger *et al.*, 2005). Full autonomy is still considered as risky and dangerous to many scientists and engineers. This has slowed the application of autonomous systems for space exploration. However, the benefits of autonomy can be clearly seen from the research currently ongoing in the field. Projects such as OASIS, SCAIP, CREST and RAMS which were discussed in chapter 2, have clearly shown the potential benefits of autonomy. On the whole, in the near future more autonomous systems will be developed for space exploration missions.

Rocks are one of the most interesting science targets for geologists and planetary scientists on the Martian surface. The identification of observed rocks is a significant task in route planning and geologic analysis. Rock shape, weathering and dispersion carry important information about environmental characteristics and processes. Therefore, it is essential to develop a method for accurate segmentation of rocks captured in Mars images.

In this thesis, a novel approach is presented to segment Mars images taken by the NASA Mars Exploration Rover (MER). In particular, a tri-level thresholding OTSU method is proposed to segment foreground (rock) from its background. The Canny algorithm is then employed both to investigate the entire edges in an image and to construct the spatial dependency of regions which are returned by the tri-level thresholding OTSU. The Template Dilatation Edge Linking (TDEL) algorithm is adapted to detect the closed contour of each rock within an image. Experimental images are from Navcam and Pancam of the MER. The experimental results of six representative images (with different illumination levels, spectral bands and scenes) including 128 rocks in total are shown. Qualitative and quantitative comparisons demonstrate that the proposed approach is consistent with human perception and offers the best performance in terms of the average value of the Precision, Recall and misclassification error (ME) to many typical classical algorithms.

Additionally, a matching keypoints in comparison is proposed for calculating the size of a detected rock. The work of matching desired keypoints involves three main stages: (a) To match the feature points on the body of a rock in a given pair of images based upon the SIFT-RANSAC algorithm. (b) To employ a method that combines Euclidean distance with the rotation angle of an image to obtain initial rough matching points. (c) To calculate the correlation between the pair of images in order to compute the accurate matching points. The size of a rock is estimated by the desired keypoints using the stereo triangulation method. The experimental results show that the proposed approach for computing rock sizes is better than the standard disparity technique in terms of accuracy.

With regards to Mars rover exploration, the ExoMars 2018 is the next ESA/Roscosmos mission. This is part of the Aurora programme with the future goal of returning rock samples to the Earth as part of the Mars Sample Return (MSR) mission. Currently, science target selection, and whether or not it is possible for a robot arm to touch a given target, is accomplished by human operators and scientists on the Earth. The use of on-board autonomy would greatly reduce human intervention, and it would be advantageous if the rover could evaluate autonomously if the robot arm could place an instrument against an identified science target.

To address this problem a fuzzy logic-based touchability system for autonomous science target touchability evaluation has been developed. The basic definitions of the terms for building the fuzzy control system are introduced, including lin-

guistic variables, fuzzy propositions, relations, implications, and inference engines. Based upon the nature regarding the touchability of a potential science target four input linguistic variables (Size, Distance, SV and Orientation) and one output linguistic variable (Touchability Index) are devised with their membership functions specified. The proposed system includes 74 fuzzy rules in total.

The simulation environment for the rank of science object touchability has been implemented in this work. Particularly, to further test and verify the validity of the proposed touchability system, laboratory-based experiments have been carried out using the hardware platform built within the project which includes two wide-angle cameras (WACs), Schunk arm, real rocks, camera mast and optical bench. Nine real rocks as experimental objects are utilised that each has a different size and science value, and are put at a different location in terms of linguistic distance: near, medium and far. In the experiments the images captured are segmented manually, but the method of rock size measurement given in this work is used to determine the size of each rock. The evaluation given by the domain expert is adopted as the ground truth. Seven experiments have been accomplished and the experimental results have shown that the designed fuzzy controller system can perform as well as the domain expert.

6.2 Original Contribution

This thesis has made a number of original contributions in the following areas:

1. An unsupervised segmentation method on Mars images is proposed to deal with the identification of scientific targets. In this method, An improved OTSU and Canny operator are combined to find out the regions of rocks. Finally, the closed contours of rocks has been achieved by a template dilation edge linking (TDEL) method.
2. A approach is proposed to match desired non-feature keypoints for the size of rocks in a pair of images by using SIFT-RANSAC algorithm, fundamental matrix, epipolar geometry and correlation.
3. An autonomous science target touchability evaluation system which is designed and implemented by Fuzzy System is developed for the following instrument deployment operation.

The above novel contributions have been documented in the following publications:

1. C. Gui and C.J. Shang. Autonomous Science Target Detection and Touchability Assessment for Planetary Exploration. Under review for journal publication.
2. C. Gui and C.J. Shang. Automatic Rock Detection Based on Rover Imagery for Planetary Exploration. Under review for journal publication.
3. C. Gui, D. Barnes and L. Pan. A SIFT-Based Method for Matching Desired Keypoints on Mars Rock Target. In the International Symposium on Artificial Intelligence, Robotics and Automation in Space (i-SAIRAS). 2012.
4. C. Gui, D. Barnes and L. Pan. An Approach for matching Desired Non-Feature Points on Mars Rock Targets Based on SIFT. In the Towards Autonomous Robotic System (TAROS) Conference. 2012.
5. C. Gui, D. Barnes and L. Pan. Planetary Exploration Autonomous Science Target Touchability Evaluation Using a Fuzzy Rule-Based Approach. In the 12th ESA Workshop on Advanced Space Technologies for Robotics and Automation (ASTRA). 2013.
6. C. Gui, D. Barnes and L. Pan. A Method for Matching Desired Non-Feature Points to Size Martian Rocks Based upon SIFT. In the Towards Autonomous Robotic System (TAROS) Conference. 2014.
7. C. Gui and C.J. Shang. Autonomous Science Target Touchability Evaluation: A Fuzzy Logic-Based Approach. ICIRA2015 International Conference on Intelligent Robotics and Applications. 2015
8. L. Pan, C. Gui, D. Barnes, C.J. Shang. Mars Multispectral Image Classification Using Machine Learning Techniques. In the 12th ESA Workshop on Advanced Space Technologies for Robotics and Automation (ASTRA). 2013.
9. L. Pan, D. Barnes, C. Gui. A Novel Saliency Method Based on Restricted Boltzmann Machine (RBM) and Its Application to Planetary Exploration. In the Towards Autonomous Robotic System (TAROS) Conference. 2014.

6.3 Future Research

Possible future directions of development are outlined as below:

1. The current latest Mars exploration rover Curiosity is loaded with Mast Camera (MastCam) system which provides multiple spectra and true-color imaging with two cameras. The cameras can take true-color images at 1600×1200 pixels and up to 10 frames per second hardware-compressed (Malin *et al.*, 2010) (Bell *et al.*, 2012). Research effort exists (Shang & Shen, 2008) (Shang *et al.*, 2011) (Shang & Barnes, 2013) for the rock detection and classification with color Mars images that is currently being adapted to identify rocks in a Martian terrain. Figure 6.1 shows an example result of such work. Combining the color image segmentation technique with the touchability work proposed herein is of great interest to strengthen the present approach.
2. In the current experimental study, because of the limit of the hardware equipment available, the science targets in the front of the two cameras can only be observed approximately between -30° and 30° (which is the overlap vision range of the two cameras). PTU (Pan-Tilt Unit) instrument may be used for future work so that the observation of the science targets can be realised between a range of -90° to 90° .
3. Currently, the image segmentation algorithm and the rock size measurement method are developed using OpenCV, but MATLAB is used to develop the touchability system. Hence, it is necessary to integrate the software packages within a common language for the future rover exploration.
4. In the present investigation, linguistic terms used to build the fuzzy control system are fixed. It would be beneficial to examine more systematically how the variations of these terms may influence the outcome of the touchability evaluation. This remains as an important further research.
5. The end goal of this research is to mount the entire software and hardware (Cameras, Schunk arm) on the PATLab 'Blodwen' half-scale ExoMars 2018 rover for field trial. Significant effort will be required to implement this task in real settings.

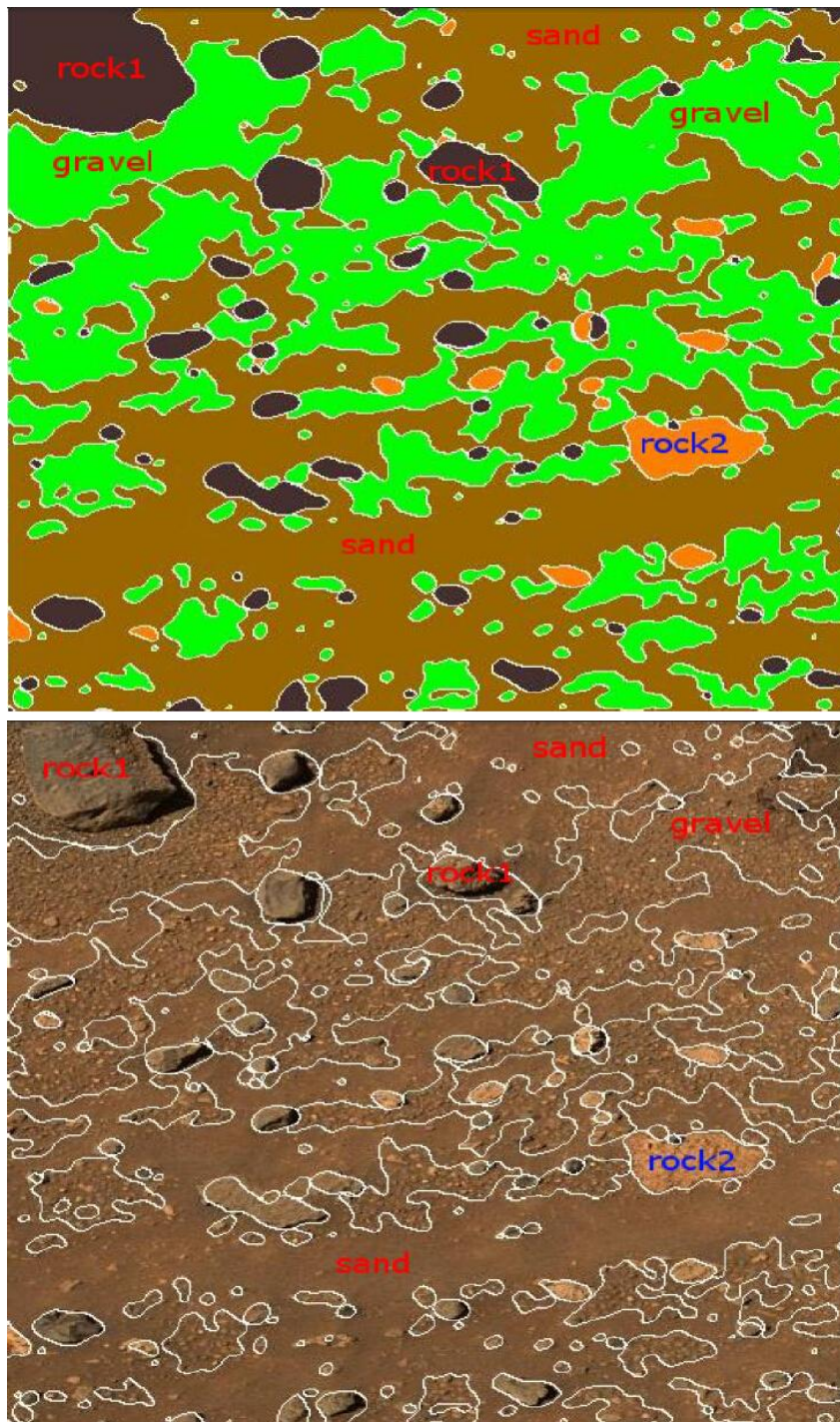


Figure 6.1: Colour image-based Martian rock detection and classification. Image Courtesy of ELSEVIER

Appendix A

List of Acronyms

CREST	Collaborative research in exploration and technology
DEM	Digital elevation model
ECSS	The European cooperation for space standardisation
EDL	Entry, descent and landing
EDM	Entry, descent and landing demonstrator module
ESA	European space agency
FRFS	Fuzzy-rough feature selection
GAP	Gas analysis package
HRC	High resolution camera
JPL	Jet propulsion laboratory
ME	Misclassification error method
MER	Mars exploration rover
MSL	Mars science laboratory mission
MSR	Mars sample return
NASA	National aeronautics and space administration
OASIS	On-board autonomous rover science investigation system
PATLab	Planetary analogue terrain laboratory
PIU	Pancam interface unit
PPL	Pasteur payload

RAMS Robotic antarctic meteorite search
RANSAC Random sample consensus algorithm
SCAIP Single command approach and instrument placement
SIFT Scale invariant feature transform
SV Science value
SVM Support vector machine
TDEL Template dilatation edge linking
USM Unsharp mask
WACs Wide angle cameras

References

- Anderson, R. C., Jandura, L., Okon, A. B., Sunshine, D., Roumeliotis, C., Beegle, L. W., Hurowitz, J., Kennedy, B., Limonadi, D., McCloskey, S., Robinson, M., Seybold, C., & Brown, K. 2012. Collecting samples in gale crater, mars; an overview of the mars science laboratory sample acquisition, sample processing and handling system. *Space science reviews*, **170(1-4)**, 57–75.
- Antonelli, G., Fossen, T. I., & Yoerger, D. R. 2008. Underwater robotics. *Springer handbook of robotics*, 987–1008.
- Apostolopoulos, D., Wagner, M. D., Shamah, B., Pedersen, L., Shillcutt, K., & Whittaker, W. L. 2000. Whittaker. technology and field demonstration of robotic search for antarctic meteorites. *Technology and field demonstration of robotic search for antarctic meteorites*.
- Arvidson, R. E., Squyres, S. W., Anderson, R. C., Bell, J. F., Blaney, D., Brckner, J., Cabrol, N. A., Calvin, W. M., Carr, M. H., Christensen, P. R., Clark, B. C., Crumpler, L., Marais, D. J. Des, & de Souza, P. A. 2006. Overview of the spirit mars exploration rover mission to gusev crater: Landing site to backstay rock in the columbia hills. *Journal of geophysical research: Planets*, **111(E2)**, doi:10.1029/2005JE002499.
- Barnes, D., Grande, M., Tyler, L., & Cook, A. 2008. The europlanet ri transnation access planetary analogue terrain laboratory(patlab). *European planetary science congress,epsc.*, **3**.
- Barnes, D., Pugh, S., & Tyler, L. 2009. Autonomous science target identification and acquisition (astia) for planetary exploration. *International conference on intelligent robots and systems, iee, st. louis, usa.*, 3329–3335.

- Barnes, D., Wilding, M., Gunn, M., Pugh, S., Tyler, L., Coates, A., Griffiths, A., Cousins, C., Schmitz, N., Bauer, A., & Paar, G. 2011. Multi-spectral vision processing for the exomars 2018 mission. *In: Proceedings of the 11th symposium on advanced space technologies in robotics and automation. astra, estec, the netherlands.*
- Barnes, D.P., Phillips, N., & paar, G. 2003. Beagle 2 simulation and calibration for ground segment operations. *Proc. 7th int. symposium on artificial intelligence, robotics and automation in space, isairas'03, nara, japan, CD-ROM Proceedings.*
- Barnes, D.P., Shaw, A., & Pugh, S. 2006. Autonomous sample acquisition for the exomars rover. *In proceedings of the 9th esa workshop on advanced space technologies for robotics and automation 'astra 2006' estec, Noordwijk, The Netherlands.*
- Baxter, J. L., Burke, E. K., Garibaldi, J. M., & Norman, M. 2007. Multi-robot search and rescue: A potential field based approach.
- Bell, J. F., Squyres, S. W., Herkenhoff, K. E., Maki, J. N., Arneson, H. M., Brown, D., Collins, S. A., Dingizian, A., Elliot, S. T., Hagerott, E. C., Hayes, A. G., Johnson, M. J., Johnson, J. R., Joseph, J., Kinch, K., Lemmon, M. T., Morris, R. V., Scherr, L., Schwochert, M., Shepard, M. K., Smith, G. H., Sohl-Dickstein, J. N., Sullivan, R. J., Sullivan, W. T., & Wadsworth, M. Mars exploration rover athena panoramic camera (pancam) investigation. *Journal of geophysical research*, **108**(E12).
- Bell, J.F., Malin, M.C., Caplinger, M.A., Ravine, M.A., Godber, A.S., Jungers, M.C., Rice, M.S., & Anderson, R.B. 2012. Mastcam multispectral imaging on the mars science laboratory rover: Wavelength coverage and imaging strategies at the gale crater field site. *43rd lunar and planetary science conference (2012) at the woodlands, March 19-23, 2541-2542.*
- Bhardwaj, Saket, & Mittal, Ajay. 2012. A survey on various edge detector techniques. *Procedia technology, 2nd international conference on computer, communication, control and information technology(c3it-2012) on february 25 - 26, 2012, 4, 220 - 226.*
- Bridges, J. C., Seabrook, A. M., Rothery, D. A., Kim, J. R., Pillinger, C. T.,

- Sims, M. R., Golombek, M. P., Duxbury, T., head, J. W., Haldemann, A. F. C., Mitchell, K. L., Muller, J. P., Lewis, S. R., Moncrieff, C., Wright, I. P., Grady, M. M., & Morley, J. G. 2003. Selection of the landing site in isidis planitia of mars probe beagle 2. *Journal of geophysical research*, **108(E1)**, doi:10.1029/2001JE001820.
- Canny, J. 1986. A computational approach to edge detection. *Ieee trans. on pattern analysis and machine intelligence* 8., 679–714.
- Carsten, J., Rankin, A., Ferguson, Dave, & Stentz, A. 2007. Global path planning on board the mars exploration rovers. March, 1–11.
- Castano, R., Estlin, T., Anderson, R. C., Gaines, D. M., Castano, A., Bornstein, B., Chouinard, C., & M.Judd. 2007a. Oasis: Onboard autonomous science investigation system for opportunistic rover science. *Journal of field robot*, **24(5)**, 379–397.
- Castano, R., Estlin, T., Gaines, D. M., Chouinard, C., Bornstein, B., Burl, M., Anderson, R. C., Thompson, D., Castano, A., & M.Judd. 2007b. Onboard autonomous rover science. *In ieeeac paper 1475, version 5, jet propulsion laboratory 4800 oak grove drive pasadena, ca 91109. jet propulsion laboratory, ieee*, 13.
- Castao, A., Anderson, R. C., Castao, R., Estlin, T., & Judd, M. 2004. Intensity-based rock detection for acquiring onboard rover science. *In 35th lunar and planetary science conference*.
- Castao, R., Mann, T., & Mjolsness., E. 1999. Texture analysis for mars rover images. *In applications of digital image processing denver*.
- Castao, R., Estlin, T., Gaines, D., Castao, A., Bornstein, B., Chouinard, C., Anderson, R. C., & Judd, M. 2006. Intensity-based rock detection for acquiring onboard rover science. *Automated target selection for opportunistic rover science*.
- Castao, R., Estlin, T., Anderson, R. C., Gaines, D., Bornstein, B., & Judd., M. 2008. Opportunistic detection and measurement of novel rocks. *In 39th lunar and planetary science conference, (lunar and planetary science xxxix)*.
- Chien, S., Smith, B., Rabideau, G., Muscettola, N., & Rajan, K. 1998. Automated planning and scheduling for goal-based automomous spacecraft. *Intelligent systems and their applications, ieee*, **13(5)**, 50–55.

- Cousins, C., Gunn, M., Prosser, B., Barnes, D., Crawford, I., Griffiths, A., Davis, L., & Coates, A. 2012. Selecting the geology filter wavelengths for the exomars panoramic camera instrument. *Planetary and space science*, **71(1)**, 80–100.
- Debus, A., Bacher, M., Ball, A., Barcos, O., Bethg, B., Gaubert, F., Halde-
mann, A., Lindner, R., Pacros, A., Trautner, R., & Vag, J. 2010. Exo-
mars 2018 rover pasteur payload. *38th cospar scientific assembly*, 2.
- Dunlop, H., Thompson, D. R., & Wettergreen, D. 2007. Multi-scale features
for detection and segmentation of rocks in mars images. *In: Proceedings
of ieee conference on computer vision and pattern recognition*, 1–7.
- Faugeras, O. 1992. What can be seen in three dimensions with an uncal-
ibrated stereo rig? *Proceedings of european conference on computer
vision*.
- Feller, W. 1971. An introduction to probability theory and its applications.
vol. i. *Wiley (1971)*.
- Fink, W., Datta, A., Dohm, J. M., Tarbell, M. A., Jobling, F. M., Furfaro,
R., Kargel, J. S., Schulze-Makuch, D., & Baker, V. R. 2008. Auto-
mated global feature analyzer - a driver for tier-scalable reconnaissance.
Aerospace conference, 2008 ieee., March, 1–12.
- Fischler, M. A., & Bolles, R. C. 1981. Random sample consensus: a paradigm
for model fitting with applications to image analysis and automated
cartography. *Communications of the acm.*, **24(6)**, 381–395.
- Furfaro, R., Dohm, J.M., Fink, W., Kargel, J., Schulze-Makuch, D., Fairn,
A.G., Palmero-Rodriguez, A., Baker, V.R., Ferr, P.T., Hare, T.M., Tar-
bell, M.A., Miyamoto, H., & Komatsu, G. 2008. The search for life
beyond earth through fuzzy expert systems. *Planetary and space sci-
ence*, **56**, 448–472.
- Godwin, R. 2000. Mars: The nasa mission reports. *Apogee books*, ISBN
1–896522–62–9.
- Goldstein, B., & Shotwell, R. 2009. Phoenix: The first mars scout mission.
Aerospace conference, ieeeac, 1579–1596.
- Golombek, M. P. 1997. The mars pathfinder mission. *Journal of geophysical
research: Planets*, **102(E2)**, 3953–3965.

- Golub, G. 1965. Numerical methods for solving linear least squares problems. *Numerische mathematik*, **7(3)**, 206 – 216.
- Gor, V., Castano, R., Manduchi, R., Anderson, R. C., & Mjolsness, E. 2001. Autonomous rock detection for mars terrain. *In: Space 2001, american institute of aeronautics and astronautics, albuquerque, nm, usa.*
- Grotzinger, J. P., Crisp, J., Vasavada, A. R., Anderson, R. C., Baker, C. J., Barry, R., Blake, D. F., Conrad, P., Edgett, K. S., Ferdowski, B., Gellert, R., & Gilbert, J. B. 2012. Mars science laboratory mission and science investigation. *Space science reviews*, **170(1-4)**, 5–56.
- Gui, C., Barnes, D., & Pan, L. 2012a. An approach for matching desired non-feature points on mars rock targets based on sift. *In the towards autonomous robotic system (taros) conference.*, 418–419.
- Gui, C., Barnes, D., & Pan, L. 2012b. A sift-based method for matching desired keypoints on mars rock target. *In the international symposium on artificial intelligence, robotics and automation in space (i-sairas).*
- Heikkila, J., & Silven, O. 1997 (Jun). A four-step camera calibration procedure with implicit image correction. *Pages 1106–1112 of: Computer vision and pattern recognition, 1997. proceedings., 1997 ieee computer society conference on.*
- Howard, A., Seraji, H., & Werger, B. 2002. Fuzzy terrain-based path planning for planetary rovers. *Proceedings of ieee international conference on fuzzy systems*, **1**(May), 316–320.
- Huntsberger, T., Cheng, Y., Stroupe, A., & Aghazarian, H. 2005. Closed loop control for autonomous approach and placement of science instruments by planetary rovers. *In 2005 ieee/rsj international conference on intelligent robots and systems, numro wpii-13 in planetary rovers.*
- iMARS Working Group. 2008. Preliminary planning for an international mars sample return mission.
- Jensen, R., & Shen, Q. 2008. Computational intelligence and feature selection: Rough and fuzzy approaches. *Ieee press and wiley (2008).*
- Jensen, R., & Shen, Q. 2009. New approaches to fuzzy-rough feature selection. *Fuzzy systems, ieee transactions on*, **17(4)**, 824–838.
- Jnsson, A., Morris, R. A., & Pedersen, L. 2007. Autonomy in space current capabilities and future challenges.

- Juan, L., & Gwun, O. 2009. A comparison of sift, pca-sift and surf. *International journal of image processing (ijip)*, **3-4**, 143–152.
- Laurent, R., & Michel, M. 2006. Autonomous navigation : A development roadmap for exomars. *In 9th esa workshop on advanced space technologies for robotics and automation*.
- Liao, P. S., Chen, T. S., & Chung, P. C. 2001. A fast algorithm for multilevel thresholding. *Journal of information science and engineering*, 713–727.
- Lowe, D. G. 1999. Object recognition from local scale-invariant features. *Proceedings of the seventh ieee international conference on computer vision.*, 1150–1157.
- Lowe, D. G. 2001. Local feature view clustering for 3d object recognition. *Ieee conference on computer vision and pattern recognition.*, 682–688.
- Lowe, D. G. 2004. Distinctive image features from scale-invariant keypoints. *International journal of computer vision.*, **60(2)**, 91–110.
- Mahmound, T. 2008. Hybrid intelligent path planning for articulated rovers in rough terrain. *Fuzzy sets and systems*, **159(1)**, 2927–2937.
- Malin, M.C., Caplinger, M.A., Edgett, K.S., Ghaemi, F.T., Ravine, M.A., Schaffner, J.A., Baker, J.M., Bardis, J.D., Dibiase, D.R., Maki, J.N., Willson, R.G., Bell, J.F., Dietrich, W.E., Edwards, L.J., Hallet, B., Herkenhoff, K.E., Heydari, E., Kah, L.C., Lemmon, M.T., Minitti, M.E., Olson, T.S., Parker, T.J., Rowland, S.K., Schieber, J., Sullivan, R.J., Sumner, D.Y., Thomas, P.C., & Yinst, R.A. 2010. The mars science laboratory (msl) mast-mounted cameras (mastcams) flight instruments. *41st lunar and planetary science conference in the woodlands*, March 1-5, 1123–1124.
- March, R. 1988. Computation of stereo disparity using regularization. *Pattern recognition letters*, **8(3)**, 181 – 187.
- Martin-Mur, T. J., Kruizinga, G. L., Burkhart, P. D., Abilleira, F., Wong, M. C., & Kangas, J. A. 2014. Mars science laboratory interplanetary navigation. *Journal of spacecraft and rockets*, **51(4)**, 1014 – 1028.
- Mikolajczyk, K., & Schmid, C. 2002. An affine invariant interest point detector. *European conference on computer vision.*, 128–142.
- Mitchell, T. 1997. Machine learning. *Mcgraw-hill (1997)*.

- Navid, S., & Homayoun, S. 2007. Landing site selection using fuzzy rule-based reasoning. *International conference on robotics and automation, ieeee*, 4899–4904.
- Otsu, N. 1979. A threshold selection method from gray level histogram. *Ieee trans. syst. man cybern*, 62–66.
- Paar, G., Oberst, J., Barnes, D. P., Griffiths, A. D., Jaumann, R., Coates, A. J., Muller, J. P., Gao, Y., & Li, R. 2008. Exomars panoramic camera 3d vision:expected quality of rover surroundings description. *In proc. of the 8th international symposium on artificial intelligence, robotics and automation in space, munich, germany*, **10**.
- Pedersen, L. 2000. Robotic rock classification and autonomous exploration. *Phd thesis, carnegie mellon university*.
- Pedersen, L., Apostolopoulos, D., Whittaker, W., Benedix, G., & Roushi, T. 1998. Sensing and data classification for a robotic meteorite search. *In mobile robots xiii and intelligent transportation systems*.
- Pedersen, L., Deans, M., Lees, D., Rajagoplan, S., & Smithi, D. E. 2005. Multiple-target single cycle instrument placement. *Geophysical research abstracts, esa sp-603, qss group, inc at nasa ames, nasa arc, ms 269-3, moffett field, ca 94035, august 2005. isairas*.
- Pugh, S. 2009. Autonomous science for future planetary exploration operations. *Phd, thesis, aberystwyth university*.
- Pugh, S., & Barnes, D. 2007. Autonomous sample selection and acquisition for planetary exploration. *Towards autonomous robotic system (taros) and the 2nd european planetary science congress (epsc)*.
- Pugh, S., Tyler, T., & Barnes, D. 2010. Automatic pointing and image capture (apic) for exomars type mission. *The 10th international symposium on artificial intelligence robotics and automation in space*.
- Pugh, S., Tyler, T., Barnes, D., Labrosse, F., & Neal, M. 2011. Automatic pointing and image capture : A field study. *11th symposium on advanced space technologies in robotics and automation (astra 2011)*.
- Pugh, S., Barnes, D., & Tyler, L. 2012. Aupe: A pancam emulator for the exomars mission. *In the international symposium on artificial intelligence robotics and automation in space (i-sairas)*.

- Pullan, D. 2006. Scientific autonomy for planetary rovers. *Rapport technique, university of leicester, space research centre, department of physics and astronomy, university of leicester.*
- Pullan, D., Sims, M. R., Wright, I. P., Pillinger, C. T., & Trautner, R. 2004. Beagle 2: the exobiological lander of mars express. *In mars express: The scientific payload, esa special publication, SP-1240.*
- Sahoo, P.K, Soltani, S, & Wong, A.K.C. 1988. A survey of thresholding techniques. *Computer vision, graphics, and image processing*, **41**(2), 233 – 260.
- Schenker, P. S., I. Huntsberger, T., Pirjanian, P., Baumgartner, E. T., & Tunstel, E. 2003. Planetary rover developments supporting mars exploration, sample return and future human-robotic colonization. *Jet propulsion laboratory, 4800 oak grove drive, pasadena, ca 91109, usa,nasa/jpl.*
- Seraji, H. 1999. Traversability index: A new concept for planetary rovers. *Proceedings of the 1999 ieee international conference on robotic and automation.*
- Sezgin, M., & Sankur, B. 2004. Survey over image thresholding techniques and quantitative performance evaluation. *J. electron. imaging.* **13**(1)., 146–165.
- Shang, C., & Barnes, D. 2011. Classification of mars mcmurdo panorama images using machine learning techniques. *Proceedings of ijcai workshop on ai in space: Intelligence beyond planet earth.*
- Shang, C., & Barnes, D. 2013. Fuzzy-rough feature selection aided support vector machines for mars image classification. *Computer vision and image understanding*, **117**(3), 202 – 213.
- Shang, C., Barnes, D., & Shen, Q. 2011. Facilitating efficient mars terrain image classification with fuzzy-rough feature selection. *International journal of hybrid intelligent systems*, **8**(1), 3–13.
- Shang, C.J., & Shen, Q. 2008. Aiding neural network based image classification with fuzzy-rough feature selection. *In 17th international conference on fuzzy systems.*
- Shaw, A., Woods, M., Honary, E., Rendell, P., Pullan, D., Barnes, D., Pugh,

- S., & Long, D. 2007. Crest robotic scientist. *In towards autonomous robotic systems (taros)*.
- Shotwell, R. 2005. Phoenix the first mars scout mission. *Acta astronautica*, **57(2-8)**, 121–134.
- Song, Y. 2008. Automated rock segmentation for mars exploration rover imagery. *In: 39th lunar and planetary science conference*.
- Space Studies Board, National Research Council. 2011. Vision and voyages for planetary science in the decade 2013-2022. *National academies press*.
- Squyres, S. W., Arvidson, R. E., Baumgartner, E. T., III, J. F. Bell, Christensen, P. R., Gorevan, S., Herkenhoff, K. E., Klingelhofer, G., Madsen, M. B., Morris, R. V., Rieder, R., & Romero, R. A. 2003. Athena mars rover science investigation. *Journal of geophysical research: Planets*, **108(E12)**, doi: 10.1029/2003JE002121.
- Squyres, S. W., Arvidson, R. E., Bollen, D., III, J. F. Bell, Brckner, J., Cabrol, N. A., Calvin, W. M., Carr, M. H., Christensen, P. R., Clark, B. C., & Crumpler, L. 2006. Overview of the opportunity mars exploration rover mission to meridiani planum: Eagle crater to purgatory ripple. *Journal of geophysical research*, **111(E1)**, doi:10.1029/2006JE002771.
- Thompson, D., Niekum, S., Smith, T., & Wettergreen, D. 2005. Automatic detection and classification of features of geologic interest. *In: Proceedings of IEEE aerospace conference*.
- Thompson, D. R., & Castano, R. 2007. Performance comparison of rock detection algorithms for autonomous planetary geology. *Aerospace conference, 2007 IEEE*, March, 1–9.
- Tomasi, C., & Manduchi, R. 2004. Intensity-based rock detection for acquiring onboard rover science. *In 35th lunar and planetary science conference*.
- Tsai, D. M., & Lin, C. Ta. 2003. Fast normalized cross correlation for defect detection. *Pattern recognition letters*, **24(15)**, 2625 – 2631.
- Tyler, L., & Barnes, D. 2008. An instrument deployment arm study for the exomars rover vehicle. *European planetary science congress, epsc.*, **3**.
- Woods, M., Shaw, A., Rendell, P., Honary, E., Barnes, D., Pugh, S., Price, D., Pullan, D., & Long, D. 2008. Crest autonomous robotic scientist:

Developing a closed-loop science exploration capability for european mars missions. *In i-sairas: International symposium on artificial intelligence, robotics and automation in space.*

Woods, M., Shaw, A., Barnes, D., Price, D., Long, D., & Pullan, D. 2009. Autonomous science for an exomars rover-like mission. *Field robotics*, **26**, 358–390.

Zadeh, L.A. 1965. Fuzzy sets. *Information and control*, **8**(3), 338 – 353.